Linköping studies in science and technology. Thesis.
No. 1464

Navigation and SAR Auto-focusing in a Sensor Fusion Framework

Zoran Sjanic

REGLERTEKNIK
AUTOMATIC CONTROL
LINKÖPING

Division of Automatic Control
Department of Electrical Engineering
Linköping University, SE-581 83 Linköping, Sweden
http://www.control.isy.liu.se
zoran@isy.liu.se

Linköping 2011

This is a Swedish Licentiate's Thesis.

Swedish postgraduate education leads to a Doctor's degree and/or a Licentiate's degree.
A Doctor's Degree comprises 240 ECTS credits (4 years of full-time studies).
A Licentiate's degree comprises 120 ECTS credits,
of which at least 60 ECTS credits constitute a Licentiate's thesis.

Linköping studies in science and technology. Thesis.
No. 1464

Navigation and SAR Auto-focusing in a Sensor Fusion Framework

Zoran Sjanic

zoran@isy.liu.se
www.control.isy.liu.se
Department of Electrical Engineering
Linköping University
SE-581 83 Linköping
Sweden

ISBN 978-91-7393-253-0 ISSN 0280-7971 LiU-TEK-LIC-2011:3

Printed by LiU-Tryck, Linköping, Sweden 2011

Za L. i G.

Abstract

Since its discovery, in the 1940's, radar (Radio Detection and Ranging) has become an important ranging sensor in many areas of technology and science. Most of the military and many civilian applications are unimaginable today without radar. With technology development, radar application areas have become larger and more available. One of these applications is Synthetic Aperture Radar (SAR), where an airborne radar is used to create high resolution images of the imaged scene. Although known since the 1950's, the SAR methods have been continuously developed and improved and new algorithms enabling real-time applications have emerged lately. Together with making the hardware components smaller and lighter, SAR has become an interesting sensor to be mounted on smaller unmanned aerial vehicles (UAV's).

One important thing needed in the SAR algorithms is the estimate of the platform's motion, like position and velocity. Since this estimate is always corrupted with errors, particularly if lower grade navigation system, common in UAV applications, is used, the SAR images will be distorted. One of the most frequently appearing distortions caused by the unknown platform's motion is the image defocus. The process of correcting the image focus is called auto-focusing in SAR terminology. Traditionally, this problem was solved by methods that discard the platform's motion information, mostly due to the off-line processing approach, *i.e.* the images were created after the flight. Since the image (de)focus and the motion of the platform are related to each other, it is possible to utilise the information from the SAR images as a sensor and improve the estimate of the platform's motion.

The auto-focusing problem can be cast as a sensor fusion problem. Sensor fusion is the process of fusing information from different sensors, in order to obtain best possible estimate of the states. Here, the information from sensors measuring platform's motion, mainly accelerometers, will be fused together with the information from the SAR images to estimate the motion of the flying platform. Two different methods based on this approach are tested on the simulated SAR data and the results are evaluated. One method is based on an optimisation based formulation of the sensor fusion problem, leading to batch processing, while the other method is based on the sequential processing of the radar data, leading to a filtering approach. The obtained results are promising for both methods and the obtained performance is comparable with the performance of a high precision navigation aid, such as Global Positioning System (GPS).

Populärvetenskaplig sammanfattning

Sedan dess uppfinning, på 1940-talet, har radar blivit en viktig sensor för mätning av avstånd i många tekniska och vetenskapliga områden. De flesta militära och många civila tillämpningar är svåra att tänka sig utan radar idag. Med teknikens utveckling har radarns användningsområde blivit större och mer tillgängliga. En av dessa områden är Syntetisk Apertur Radar (SAR), där en luftburen radar används för att skapa högupplösta bilder av den avbildade scenen. Trots att SAR-metoder är kända sedan 1950-talet, har dessa metoder ständigt utvecklats och förbättrats och nya algoritmer, lämpliga för realtidstillämpningar, har trätt fram på senare tid. I och med att hårdvara har blivit mindre och lättare, har möjligheter för SAR att monteras på mindre obemannade flygande farkoster (UAV) blivit större.

En viktig sak som är nödvändig i SAR algoritmer är skattning av flygande plattforms rörelse, såsom position och hastighet. Eftersom denna skattning alltid är bestyckat med fel, speciellt om sämre navigeringssystem vanliga i UAV används, kommer SAR bilder att vara förvrängda. En av de vanligaste bildförvrängningar orsakad av plattformens okända rörelse är defokusering av SAR bilden. Processen som korrigerar för detta kallas för auto-fokusering i SAR terminologi. Traditionellt har detta problem lösts med metoder som kastar bort informationen om plattformens rörelse, mestadels på grund av icke realtidsmetodiken. Eftersom bildens (de)fokus och plattformens rörelse är relaterade till varandra, är det möjligt att använda information från SAR bilder som en sensor och förbättra skattningen av plattformens rörelse.

Denna formulering av auto-fokuseringsproblemet är lämpad för sensorfusionsramverk. Sensorfusion är tillståndsskattningsmetod där information från olika sensorer sammanfogas för att på så sätt åstadkomma bästa möjliga skattningen av tillstånden. I detta fall, informationen från sensorer som mäter plattformens rörelse, huvudsakligen accelerometrar, skall fusioneras tillsammans med informationen från SAR bilder för att skatta rörelsen hos den flygande plattformen Två olika metoder baserade på detta tillvägsgångsätt är testade på simulerade SAR data och resultat är utvärderade. Första metoden är baserad på en optimeringsformulering av sensorfusionsproblemet, vilket leder till en metod som hanterar data blockvis, medan den andra baseras på sekvensiell behandling av radar data, vilket är en filtreringsformulering. De erhållna resultaten är lovande för båda metoderna och den uppnådda noggrannheten är jämförbar med noggrannheten som fås med navigeringshjälpmedel med hög prestanda, som Global Positioning System (GPS).

Acknowledgments

First, I would like to thank my supervisor Prof. Fredrik Gustafsson and my co-supervisor Dr Thomas Schön. Discussions with you have always been a great source of inspiration and guided me in the right direction along the way.

I would also like to thank Prof. Lenart Ljung for giving me the opportunity to do my post graduate studies at the best control theory group in the world(!), as well as people from Saab Aeronautics in Linköping for letting me do it, Dr Predrag Pucar, Niklas Ferm, Björn Kullberg, Tobias Jansson and Dr Gunnar Holmberg. Thanks for all your support and understanding for my "absence from the work".

My thanks go also to the people at Saab EDS in Göteborg, Dr Hans Hellsten and Dr Patrik Dammert. Your comments and radar expertise have helped me a lot in my work.

And speaking about the best group in the world, thanks to all guys in this group, Prof. Lenart Ljung and Prof. Svante Gunnarsson for your excellent leadership, Ulla Sallaneck and Åsa Karmelind for keeping everything well ordered and organised, Martin Skoglund and Roger Larsson for good cooperation, Dr Umut Orguner, Dr David Törnqvist and Dr Martin Enqvist for all kind of discussions about various research issues. The best groups are not only characterised by the work but also by the fun, and there is no lack of that here either. Lic Christian Lundquist, Lic Christian Lyzell, Karl Granström, Jonas Callmer, Dr Ragnar Wallin, Dr Henrik Ohlsson, Sina Koshfetrat Pakazad, Lic Rikard Falkeborn and of course my "roomies", Lic Daniel Petersson and Fredrik Lindsten, you all know what the fun is.

This journey that I am doing would be impossible without support from my family and friends, so thanks for all the confidence and trust.

Last, but not least, thanks to the LINK-SIC Industry Excellence Center for financing my studies.

Linköping, January 2011
Zoran Sjanic

Contents

Notation **xiii**

1 Introduction **1**
1.1 Background 1
1.2 Problem Formulation 4
1.3 Thesis Overview 5
1.4 Contributions 5

2 Principles of Synthetic Aperture Radar **7**
2.1 Real Aperture Radar 7
2.2 Synthetic Aperture Radar 9
2.3 Quantisation Effects 13

3 Sensor Fusion Framework **15**
3.1 State Estimation and Sensor Fusion 15
3.2 SAR in the Sensor Fusion Framework 18
3.3 System Model 20
3.3.1 Euler Angles 21
3.3.2 Quaternions 21
3.3.3 Measurements 22
3.3.4 Specialisation of the Model Used Here 23
3.3.5 Stationary Estimate Accuracy 24
3.4 Some Estimator Performance Measures 25

4 Measuring Focus **27**
4.1 Focus Measures 27
4.1.1 Sum-Modified-Laplacian 27
4.1.2 Tenengrad 28
4.1.3 Discrete Cosine Transform 28
4.1.4 Entropy 29
4.2 Evaluation on Test Optical Image 29
4.2.1 Threshold Dependence 32
4.2.2 Blur Kernel Dependence 32

4.3 Evaluation on Test SAR Images 33
4.3.1 Threshold Dependence 33
4.3.2 Position Blur Dependence 33
4.3.3 Evaluation on Perturbed Trajectory 35

5 Methods Based on the Complete SAR Images **47**
5.1 Gradient Based Search 47
5.1.1 Calculating the Gradient 48
5.1.2 Numerical Examples 51
5.2 Global Grid Search 57
5.2.1 Numerical Examples 58

6 Methods Based on Raw Radar Data **61**
6.1 Introduction to Phase Gradient or Range Gradient Methods 61
6.2 Estimating the Range Gradient 63
6.3 EKF and Evaluation of the Performance 64
6.4 Comparison between Filter and Optimisation Method's Results . . 67

7 Concluding Remarks **73**
7.1 Conclusions 73
7.2 Future Work 74

Bibliography **77**

Notation

Symbols and Operators

Notation	Meaning
x_t	State vector
y_t	Measurements vector
u_t	Known inputs vector
w_t	Process noise
e_t	Measurement noise
Q_t	Process noise variance
R_t	Measurement noise variance or range
$\hat{x}$	Estimate of x
$\mathcal{N}(\mu, P)$	Gaussian distribution with mean μ and variance P
$x_{0:N}$	Short notation for $\{x_0,\ x_1,\ \dots,\ x_N\}$
X, Y, Z	Position in Cartesian coordinates
v^X, v^Y, v^Z	Velocity in $X-$, $Y-$ and $Z-$direction, respectively
a^X, a^Y, a^Z	Acceleration in $X-$, $Y-$ and $Z-$direction, respectively
I	Grey-scale image (optical or SAR)
$\tilde{I}$	Complex valued SAR image
$\mathbb{R}$	Set of real numbers
$\mathcal{O}$	Ordo
$\dot{x}_t$	Time derivative of x_t
$\sim$	Is distributed according to
$\lvert x \rvert$	Absolute value of x
$\lVert x \rVert_P$	$P^{-1}-$weighted norm of x, $\sqrt{x^T P^{-1} x}$
x^*	Complex conjugate of x
$\arg\min_x$	Minimising argument with respect to x
$\arg\max_x$	Maximising argument with respect to x
$\in$	Is member of
$\notin$	Is not member of
$\mathbf{dim}(x)$	Amount of elements in vector x
$A * B$	Convolution of matrices A and B

Abbreviations

Abbreviation	Meaning
BFGS	Broyden-Fletcher-Goldfarb-Shanno (quasi-Newton algorithm)
CARABAS	Coherent All RAdio BAnd Sensing
DCT	Discrete Cosine Transform (focus measure)
DOF	Degrees Of Freedom
EKF	Extended Kalman Filter
MAP	*Maximum A Posteriori* (estimate)
MV	Minimum Variance (estimate)
RAR	Real Aperture Radar
SAR	Synthetic Aperture Radar
SML	Sum-Modified-Laplacian (focus measure)
TG	Tenengrad (focus measure)
TkBD	Track Before Detect

1

Introduction

1.1 Background

Radar (Radio Detection and Ranging) is a system used for finding different objects in the environment. Usually, in radar, radio waves are transmitted from the transmitter antenna and echoed waves from objects are received. By measuring the time between transmission and reception of the waves, the range to the objects can be determined. Radar has, since its introduction in the early 1940's, been used more and more in different areas of technology and science. It spans from early military applications, where radar was used to detect and track enemy aircraft to more recent applications in the automotive industry where radar is used for detection of other vehicles or pedestrians on the road in order to prevent accidents. The primary area of radar application is, just as when it was invented, tracking of different objects for various purposes, like for example tracking of airplanes in Air Traffic Control or cars in automotive anti-collision systems.

An example of a target tracking scenario is illustrated in figure 1.1a, where two omni-directional ranging sensors are estimating the position of one stationary target. It is easy to see that we can determine the target's position based on the intersection of the ranges R_1 and R_2. The accuracy of the target's position is dependent of the range accuracy of the radars. Note that there are two intersections, giving the ambiguity in determination of the targets position. If even more ranging sensors are used as in Figure 1.1b, more intersections of the ranges are available and the target's position can be determined with even higher accuracy. The same scenario can be obtained if we have one sensor carried by some moving platform that is moving along the straight trajectory with velocity v_t and collecting radar echos from the stationary target, as in Figure 1.1c. Usually, the targets that are tracked are also recognised as targets, *i.e.* some kind of target

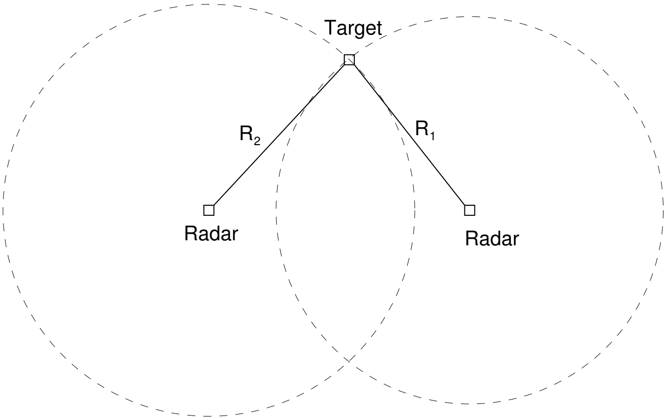

(a) *Target tracking scenario with two stationary radars and one stationary target.*

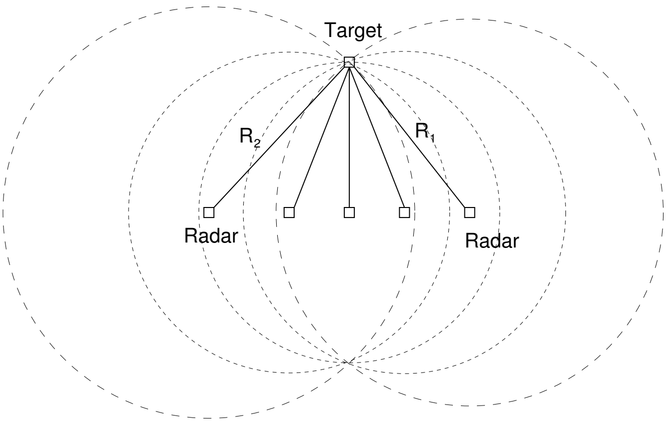

(b) *Target tracking scenario with five stationary radars and one stationary target.*

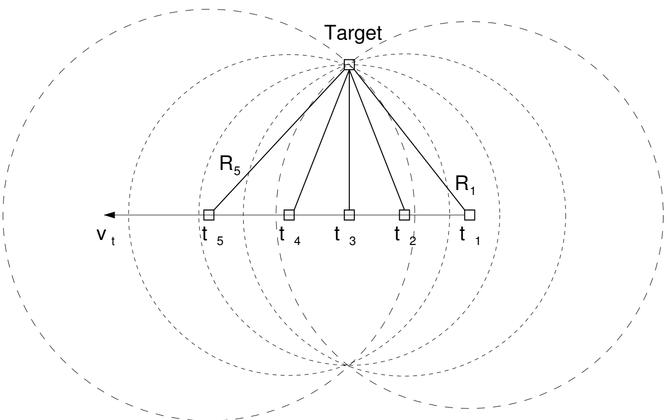

(c) *Target tracking scenario with one moving radar and one stationary target.*

Figure 1.1: *Different target tracking examples.*

Figure 1.2: *An aircraft carrying CARABAS, a low frequency UHF SAR. Image is courtesy of Saab AB.*

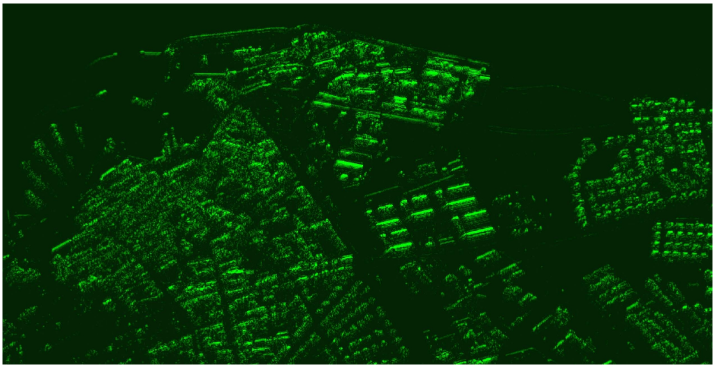

Figure 1.3: *CARABAS SAR image of Simrishamn, Sweden. Image is courtesy of Blekinge Institute of Technology.*

detection and association is used. If that is not done, *i.e.* no tags are assigned to the targets, and every radar echo is recorded and treated as target, we get the, so called, track before detect (TkBD) approach [Salmond and Birch, 2001]. Suppose now that, instead of one target as in the example above, we are tracking many targets, each with different radar reflectance. Based on these reflections we can obtain an "image" of the scene where targets are placed. This is exactly the idea underlying Synthetic Aperture Radar (SAR), where this basic principle is used to create high resolution images of the stationary scene with radar carried by the flying platforms, like aircraft or satellites. In Figure 1.2 an aircraft carrying low frequency UHF SAR, CARABAS, is shown and in Figure 1.3 an image of a small town in southern Sweden, Simrishamn, produced using CARABAS is depicted.
One of the biggest advantages of radar images over optical images is the radar's all-weather operational capability, *i.e.* the radar is not occluded by the clouds. This is a very important advantage that makes the radar an attractive imaging

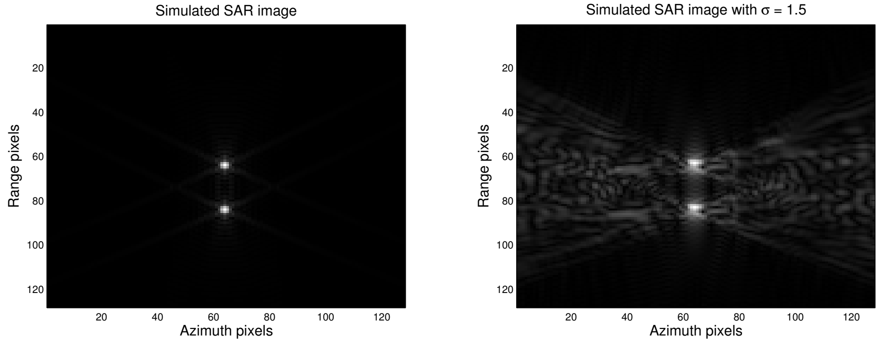

*(**a**) Focused SAR image of two point targets.* *(**b**) Unfocused SAR image of two point targets with $\sigma = 1.5$.*

Figure 1.4: *Example SAR images with perturbed trajectory.*

sensor. Moreover, the radar operates in different frequency bands compared to optical images, making it possible to discover things invisible to optical systems.

1.2 Problem Formulation

In the above examples, it was assumed that the radar positions are known and the only source of the targets' estimated position error is the range measurement inaccuracy. In many target tracking applications that assumption is valid, but if the radar's or the platform's positions are unknown, which is always the case, the targets' estimated positions will suffer from additional inaccuracy caused by the position error. In the context of SAR imaging, this inaccuracy is the dominating source of the error, since measured range accuracy is usually high. Today, many flying platforms are equipped with precision global navigation systems like Global Navigation Satellite Systems (GNSS) which are able to deliver very accurate position and velocity estimates. The downside of the GNSS is that they are very easy to disturb or jam which means that some alternative, GNSS independent, way of obtaining good navigation estimate is needed. This is particularly important in military operations where access to GNSS can not be assumed. The position inaccuracy will lead to different image distortions, of which image defocus is the most common one. An example of image defocusing is depicted in Figure 1.4, where two point targets are imaged. Data are acquired with linear trajectory and constant speed. In Figure 1.4a, the same linear trajectory is used for image creation, which results in a perfectly focused image. In the image in Figure 1.4b, the variation in the platform's cross-track position was added as $\mathcal{N}(0, \sigma^2)$, $\sigma = 1.5$ and the image is created with the assumption that the path was linear. This gives the unfocused images as depicted. This leads to the conclusion that if better position accuracy of the platform can be estimated, the distortions can be minimised and more focused images obtained. This process is in SAR context known as auto-focusing. Many SAR algorithms do not use the position of the platform explicitly, but rather assume a straight flying trajectory and try to correct the images afterwards. In this way, the information about the trajectory that the images contain is not used. However, the back-projection SAR algorithms [Natterer, 1986] utilise the platform's position and the information in the images could be exploited to obtain better position of the platform and in turn better images.

In the view of this approach for SAR images, the problem is closely related to the Simultaneous Localisation and Mapping (SLAM), [Durrant-Whyte and Bailey, 2006, Bailey and Durrant-Whyte, 2006], where a map of the unknown environment is estimated at the same time as the platform's position. The SLAM problem has been well studied during recent years and many different solution methods have been proposed. One method that has been quite successful is to solve the SLAM problem in the sensor fusion framework. In the SAR application, the map of the environment from SLAM, is the unknown scene that is imaged and can be seen as the two dimensional map of point reflectors. The position of the platform is the same as in the SLAM problem. The idea is now to apply the sensor fusion framework as in the SLAM case and view the SAR images as a "sensor" that contains information about the position of the platform and obtain the goal mentioned above, *i.e.* better position estimate and better images.

1.3 Thesis Overview

In Chapter 2 the basic principles behind SAR are explained. In Chapter 3, the sensor fusion framework is introduced and a method of using SAR images for navigation purposes is suggested. In Chapter 4, different image focus measures are evaluated on both optical and SAR images. Chapter 5 covers methods based on the complete SAR images leading to the batch formulation or smoothing and Chapter 6 describes the filtering approach based on the raw radar data. In Chapter 7 conclusions and future work are discussed.

1.4 Contributions

Contributions relevant for this thesis:

> Z. Sjanic and F. Gustafsson. Simultaneous Navigation and SAR Auto-focusing. In *Proceedings of 13th International Conference on Information Fusion*, Edinburgh, UK, July 2010.

This work introduces the simultaneous auto-focusing of the SAR images and navigation in the sensor fusion framework. Auto-focusing problem is formulated as a state estimation optimisation problem and solved with both local and global methods.

Other contributions:

> Z. Sjanic, M. A. Skoglund, T. B. Schön, and F. Gustafsson. A Nonlinear Least-Squares Approach to the SLAM Problem. In *Proceedings of 18th IFAC World Congress (submitted to)*, Milano, Italy, August/Septemeber 2011.

In this contribution, a nonlinear least-squares formulation of the visual SLAM problem with 6-DOF platform motion description is posed and solved. the solution is leading to the smoothed estimate of the platform's states and the landmarks. This work is submitted to the 18th IFAC World Congress, Milano, Italy, August/September, 2011.

> R. Larsson, Z. Sjanic, M. Enqvist, and L. Ljung. Direct Prediction-error Identification of Unstable Nonlinear Systems Applied to Flight Test Data. In *Proceedings of the 15th IFAC Symposium on System Identification*, Saint-Malo, France, July 2009.

In this work, an approach for identification of unstable and nonlinear systems based on prediction-error method is presented. The predictors are based on the nonlinear state space description of the system. The methods are implemented and evaluated on both simulated data and real flight test data with promising results.

2

Principles of Synthetic Aperture Radar

In this chapter the basic principles of the Synthetic Aperture Radar (SAR) are explained. It starts with the Real Aperture Radar (RAR), continues with the methods to create high resolution images and mentions some of the effects associated with SAR.

2.1 Real Aperture Radar

In the simplest setup a radar image can be created with the moving platform carrying the side-looking radar and flying above the scene to be imaged. By sending and receiving radar pulses along the trajectory, a range-azimuth image is created, see figure 2.1. Since the energy in each radar pulse is spread out over the scene, every pulse will produce a one-dimensional image according to the simple principle; each echoed pulse is received and gated in the range bins according to the time (t) it takes to receive the pulse, using the relation $R = tc/2$, where c denotes the speed of light. Since echoes are saved in the digital memory this will cause some quantisation effects which are described in the Section 2.3 below. This means that each range bin will contain the total energy reflected from the scene on that specific range. When all of these simple one-dimensional images are stacked next to each other, a full RAR image is created. RAR images will have the imaged scene smeared across the azimuth, giving very poor effective resolution which can be seen in Figure 2.2, where a simulated example of the RAR image of two point targets is depicted. The resolution in the azimuth direction for the RAR images is governed by the basic laws of the electromagnetism which state that the radar lobe width is dependent of the antenna size and the wavelength of the carrier according to λ/d, where d is antenna size and λ is the wavelength. This will give the resolution $\lambda R/d$ where R is the range to the imaged scene. We

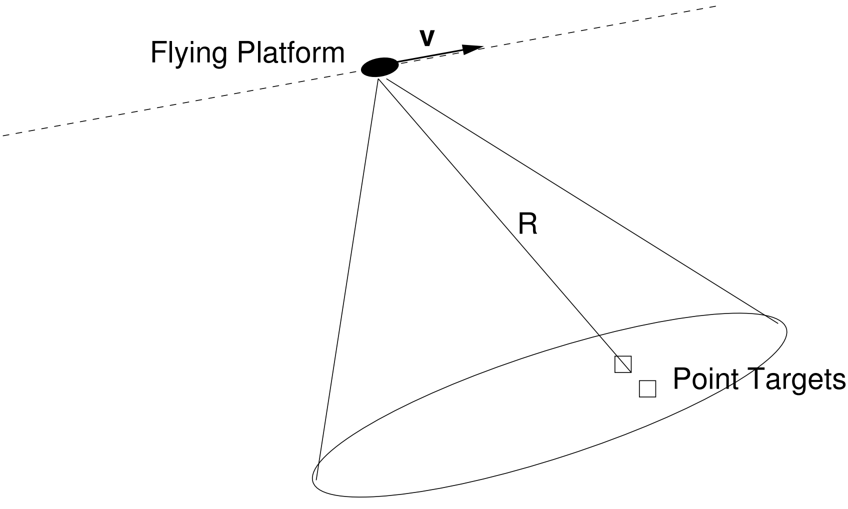

Figure 2.1: *Side-looking radar geometry. R is the range to the target.*

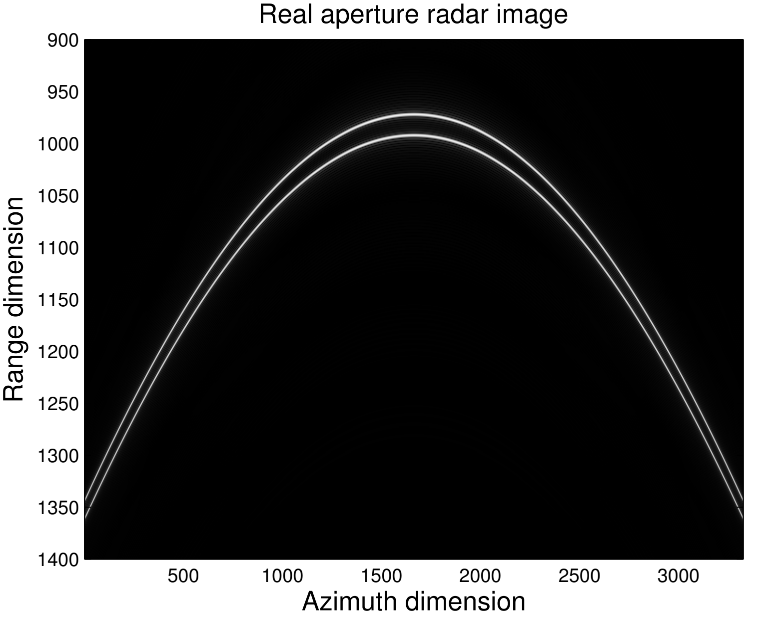

Figure 2.2: *Real aperture radar image of the two point targets.*

see that by decreasing the wavelength or increasing the antenna we can make the lobe narrower and increase the resolution. The wavelength is usually fixed to a specific value and there is not much freedom of decreasing it, and besides there are other unwanted effects if low wavelengths are used like cloud occlusions. There are also limits regarding how large antenna a flying platform can carry which limits that parameter as well. However, by using the movement of the platform a long antenna can be synthesised and the resolution of the images is drastically increased. This principle leads to the SAR [Cutrona et al., 1961].

2.2 Synthetic Aperture Radar

As mentioned above the movement of the platform can be utilised to improve the resolution in the azimuth direction. During the motion of the platform the scene, which can be assumed to consist of point scatterers, will travel trough the radar lobe and the slant range to it will vary, see Figure 2.1. This slant range variation can be compensated for each radar echo and all of the echos can be integrated in order to produce an image which can be expressed as

$$I_{\mathrm{SAR}}(R, A) = \int_{D_t} I_{\mathrm{RAR}}(R, t) g(R, t) dt \tag{2.1}$$

where $I_{\mathrm{SAR}}(R, A)$ is the SAR image, $I_{\mathrm{RAR}}(R, t)$ is the RAR image (or raw radar data), $g(R, t)$ is the slant range compensating function, R is the range dimension, t is the azimuth dimension of the raw data (or time dimension), A is the azimuth dimension of the SAR image and D_t is the azimuth (or time) domain of the RAR image. Image creation can be performed in the image (or time) domain or in the frequency domain. Some of the most important frequency domain methods are the Fourier-Hankel [Fawcett, 1985, Hellsten and Andersson, 1987, Andersson, 1988] and the ω-K migration methods [Rocca, 1987, Cafforio et al., 1991, Milman, 1993]. The frequency domain methods are generally fast, but has a downside that they assume straight trajectories in order to work properly. However, in reality the trajectory will never be straight, especially if the flying platform is a small UAV. This will cause image distortions and auto-focusing is more complicated. This opens up for the use of time domain methods, which are slower, but can handle any trajectory shape. This of course is an important benefit, particularly if SAR images are to be used for trajectory estimation, and time domain methods will be considered from now on.

One of the most known time domain methods is back-projection [Natterer, 1986]. In the back-projection procedure each saved radar echo, which is one dimensional, is back-projected onto a two dimensional area. In this way a poor quality image of the scene is obtained. Now we can sum up all these back-projected images in order to obtain the full SAR image. This is equivalent to the integration operation in (2.1), except that integration becomes summation due to the discrete data. Figure 2.3 describes this procedure in a schematic way, and Figure 2.4 is the resulting simulated image if the same raw data used for RAR from Figure 2.2 is

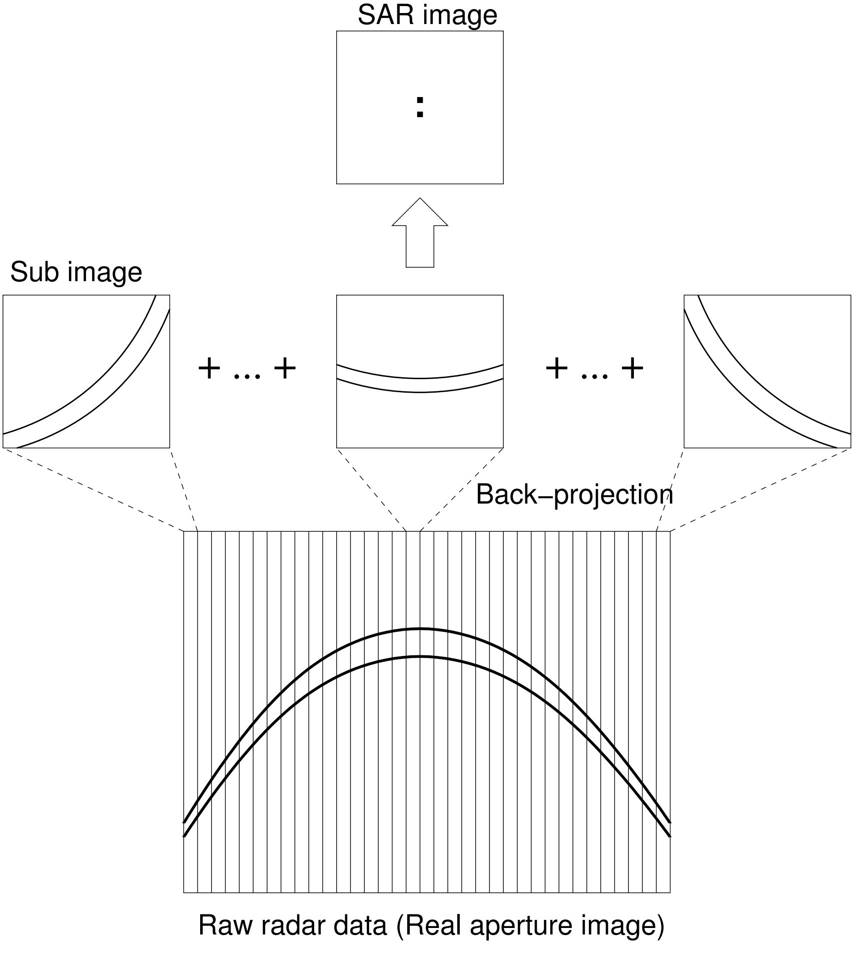

Figure 2.3: *Back-projection operation schematically described.*

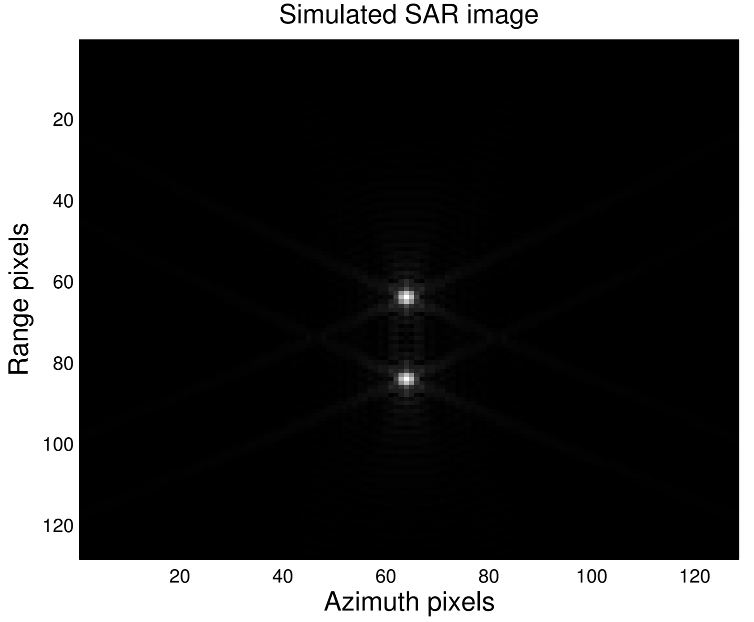

Figure 2.4: *Synthetic aperture radar image of the two points.*

used. The main downside of this kind of procedure is that the number of operations needed to synthesise an image is proportional to $\mathcal{O}(NM^2)$ for a $M \times M$ image created from N radar echos. This can be a large number for large images and long aperture times. However during recent years a modification to the original back-projection, called fast factorised back-projection, has been developed. This method can actually create of the SAR image in $\mathcal{O}(M^2 \log N)$ number of operations [Ulander et al., 2003]. This implies considerable time saving and together with the development of the computers, this allows to consider real time SAR imaging.

It is now clear that in order to perform the back-projection (or factorised fast back-projection) operation the trajectory of the platform must be known or otherwise the resulting image will be distorted. The image distortion can manifest itself in many ways, from pure translation through geometric distortion to defocusing. Since translation and geometric distortions are hard to measure if the true scene is unknown, these will not be considered here. Defocusing, which is a very common distortion, is measurable, at least seen as an image property. The main source of defocusing of the SAR images is the error in the trajectory estimate used for creation of the images. In the frequency domain methods, a straight trajectory is used, and if the real trajectory deviates from this assumption, it will cause image defocusing. In the time domain methods, despite the fact that the general trajectory form is used, deviations from the real trajectory will cause the back-projected sub images to be shifted. The summation operation of the sub

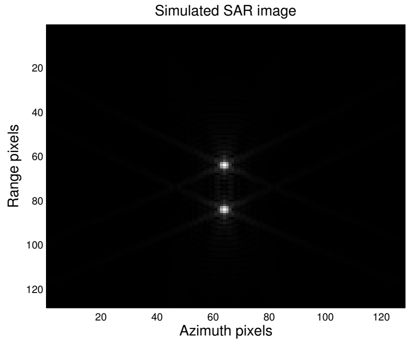

***(a)** Focused SAR image of two point targets.*

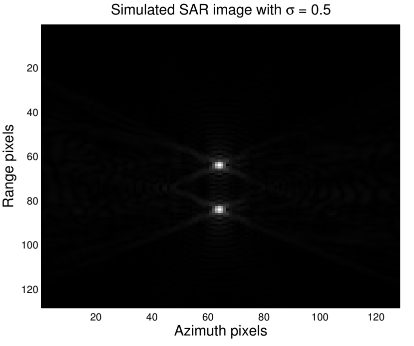

***(b)** Unfocused SAR image of two point targets with $\sigma = 0.5$.*

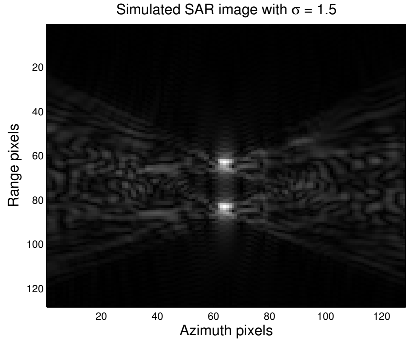

***(c)** Unfocused SAR image of two point targets with $\sigma = 1.5$.*

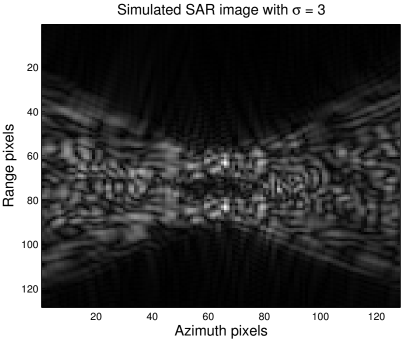

***(d)** Unfocused SAR image of two point targets with $\sigma = 3$.*

***Figure 2.5:** Example SAR images with different perturbed trajectories.*

images will then cause defocusing. To illustrate this, the simple two point image from Figure 2.4 can be used. If Gaussian white noise with different variances is added to the cross-track position of the platform, images as in Figure 2.5 are obtained. In Figure 2.5a, the image is created with the same trajectory as data were acquired, which results in a perfectly focused image. In the other three images the cross-track position noise was $\mathcal{N}(0, \sigma^2)$ where $\sigma = \{0.5, 1.5, 3\}$ and the images are created under the assumption that the trajectory was linear. This results in defocused images, and the degree of defocusing depends on the noise variance. Much effort has been spent to correct for this, see for example Oliver and Quegan [2004], Wahl et al. [1994], Xi et al. [1999], Morrison and Munson [2002], Xing et al. [2009]. Traditionally, these methods are open-loop type, meaning that the image is created with assumptions of linear flight trajectory and focusing is done afterwards in an open-loop way discarding possible flight trajectory information. This is a consequence of the off-line image generating process where the trajectory is no longer interesting. In the setup where SAR images are generated on-line, an idea, as already mentioned, is to use information from the image defocusing and navigation system together. The approach is to fuse this information in a sensor fusion framework and try to obtain the best possible solution to both focusing and navigation simultaneously. This will be covered in Chapter 3 and how information about defocusing can be obtained will be extensively covered in Chapter 4.

2.3 Quantisation Effects

Since radar measurements collected during flight are saved in discrete form, range, as well as azimuth, will be quantised. The size of the quantisation depends on the radar processing parameters, *i.e.* sampling frequency for range data and pulse repetition frequency for azimuth data. The quantisation effect in the range direction will set the limit on attainable observability for the errors in the trajectory. For example, for the situation in Figure 2.6, where a point target is considered, R_t and R_t' can be calculated as

$$R_t' = \sqrt{R_0^2 + (x_0 - (\Delta v)t)^2} \approx R_0 + \frac{(x_0 - (\Delta v)t)^2}{2R_0} \tag{2.2a}$$

$$R_t = \sqrt{R_0^2 + (x_0 - vt)^2} \approx R_0 + \frac{(x_0 - vt)^2}{2R_0} \tag{2.2b}$$

$$\Delta v = v + \delta_v \tag{2.2c}$$

assuming that v is constant along the synthetic aperture and that $x_0 \ll R_0$, which is true for the SAR geometry. This gives that

$$\Delta_R(\delta_v, t) = |R_t - R_t'| = \left| \frac{2x_0\delta_v t - 2v\delta_v t^2 - \delta_v^2 t^2}{2R_0} \right| \tag{2.3}$$

must be larger than the quantisation bin for the velocity error to have influence on the SAR image. Due to the fact that the largest possible t is limited (the image is created after finite time), δ_v will then have a lower limit posed by the SAR processing parameters and the particular flight case. An example is given in Figure 2.7, where it can be seen that for small δ_v, the range difference will never be larger than the quantisation limit. This means that the real aperture images will be the same and the observability of the velocity error in the azimuth direction is lacking.

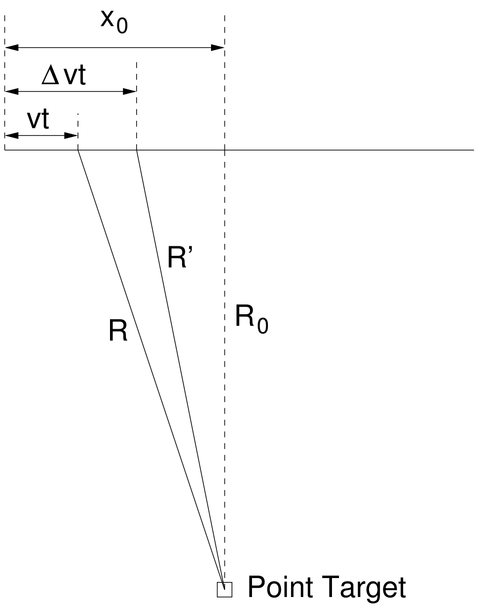

Figure 2.6: *Range error geometry with error in velocity of azimuth direction only.*

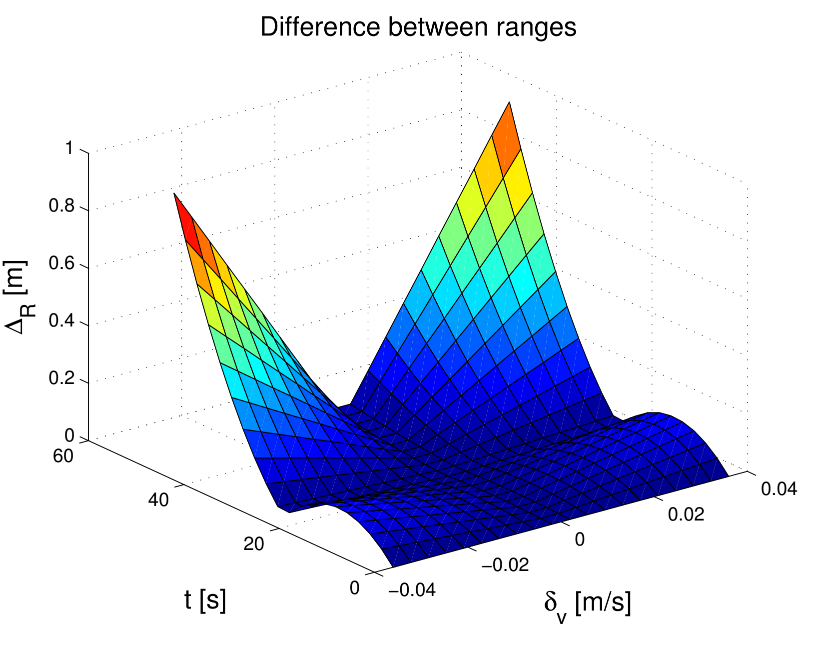

Figure 2.7: *Range difference as a function of δ_v and time for $R_0 = 4000$ m, $x_0 = 2300$ m and $v = 100$ m/s. Note that the quantisation limit is 0.9 m.*

3 Sensor Fusion Framework

In this chapter a basic approach to state estimation and sensor fusion is introduced. This approach leads to the estimation solution in the form of a filter or a smoother. Further, the incorporation of the SAR images or raw data in this framework will be described. Moreover, dynamic and measurement models that will be used are described.

3.1 State Estimation and Sensor Fusion

In many practical engineering applications, one works with dynamical systems that can describe dynamical processes, *e.g.* movement of different objects, like an aircraft. Additionally, information about some entities that characterise the dynamical system is also sought. In a perfect world it would be possible to measure everything that is of interest, but in reality it is quite often not possible. This can be due to the fact that sensors are too expensive, heavy or not very accurate. A typical example of this problem is a situation where accelerations are measured, but velocity and position of the moving platform are wanted. This leads to an estimation problem. In this context, a particularly useful description of the dynamical systems is the state space description, usually in the form

$$x_{t+1} = f(x_t, u_t, w_t) \tag{3.1a}$$

$$y_t = h(x_t, u_t, e_t) \tag{3.1b}$$

where x_t are the states of the system, u_t are the known inputs, w_t is the system noise with variance Q_t, y_t are the measurements, e_t is the measurement noise with variance R_t, f is a function that describes the dynamics of the system and h is a function that relates the measurements and the states of the system. This is a rather general model of a system and one that is often used is

$$x_{t+1} = f(x_t, w_t) \tag{3.2a}$$

$$y_t = h(x_t) + e_t \tag{3.2b}$$

where noise term in the measurement equation appears in an additive way and the known input u_t is omitted. This poses no practical problems, since in most cases the additive measurement noise is a plausible model and known input can be modelled as time dependent functions f and h. In the rest of this thesis u_t will be omitted. The descriptions of the dynamics and measurements (3.1) and (3.2) are in discrete time, which is suitable for implementation in computers and because most of the modern sensors deliver data in sampled form. Usually system dynamics is dependent on the moving platform, so it can be fixed for each application. In our case the dynamics of the system is modelled as aircraft dynamics which will be described below.

Another, and more general, way of describing the system (3.2) is in the form of conditional probability density functions for state transition and measurements

$$x_{t+1} \sim p(x_{t+1}|x_t) \tag{3.3a}$$

$$y_t \sim p(y_t|x_t) \tag{3.3b}$$

From the system perspective these two descriptions are equivalent. The model above are referred to as Markov process', *i.e.* the state at time t is only dependent of the state at time $t-1$. In a similar way the measurement at time t is conditionally independent of the states in all times except the state at time t. As an example of model (3.3), take equation (3.2b) and suppose that the noise has Gaussian distribution with zero mean and variance R_t. This will yield

$$p(y_t|x_t) = p_{e_t}(y_t - h(x_t)) = \frac{1}{\det\{2\pi R_t\}^{1/2}} e^{-\frac{1}{2}(y_t - h(x_t))^T R_t^{-1}(y_t - h(x_t))} \tag{3.4}$$

The estimation problem can now be posed as determining the states $x_{1:N}$ given all the measurements $y_{0:N}$ (or equivalently expressed, obtaining the posterior distribution $p(x_{0:N}|y_{1:N})$) and the model (3.2) or (3.3). One straightforward solution is to find $x_{0:N}$ that maximise the posterior distribution, so called *Maximum a posteriori* estimate (MAP)

$$\hat{x}_{0:N}^{\text{MAP}} = \arg\max_{x_{0:N}} \; p(x_{0:N}|y_{1:N}) \tag{3.5}$$

With help from the Bayes' rule [Bayes, 1763]

$$p(x|y) = \frac{p(y|x)p(x)}{p(y)} \tag{3.6}$$

the maximisation problem can be rewritten as

$$\hat{x}_{0:N}^{\text{MAP}} = \arg\max_{x_{0:N}} \; p(y_{1:N}|x_{1:N})p(x_{0:N}) \tag{3.7}$$

($p(y_{1:N})$ is omitted since it does not depend on $x_{0:N}$ and does not influence the maximisation procedure). This formulation together with Markov and measurement model assumption leads to the following MAP optimisation

$$\hat{x}_{0:N}^{\text{MAP}} = \arg\max_{x_{0:N}} \; p(x_0) \prod_{t=1}^{N} p(y_t|x_t)p(x_t|x_{t-1}) \tag{3.8}$$

where $p(x_0)$ is the prior of the states, *i.e.* the belief about the state values before any measurements have arrived. The sequential solution to (3.8) is given by recursive Bayesian filtering. The posterior distribution for each time instant can be obtained as, see Gustafsson [2010] for complete derivation,

$$p(x_1|y_0) = p(x_0) \qquad \text{(Initialisation)} \tag{3.9a}$$

$$p(x_t|y_{1:t}) = \frac{p(y_t|x_t)p(x_t|y_{1:t-1})}{p(y_t|y_{1:t-1})} \tag{3.9b}$$

$$p(y_t|y_{1:t-1}) = \int_{\mathbb{R}^n} p(y_t|x_t)p(x_t|y_{1:t-1})dx_t \tag{3.9c}$$

$$p(x_t|y_{1:t-1}) = \int_{\mathbb{R}^n} p(x_t|x_{t-1})p(x_{t-1}|y_{1:t-1})dx_{t-1} \tag{3.9d}$$

Procedure (3.9) defines a very general nonlinear filter that can be applied to a large class of the dynamic and measurements models. However, the close form solution exists only in a few cases. In practice, one such important special case where both the dynamic and the measurement models are linear, the prior has Gaussian distribution and the process and the measurement noise are Gaussian and white, is

$$f(x_t, w_t) = Fx_t + w_t \tag{3.10a}$$

$$h(x_t) = Hx_t \tag{3.10b}$$

$$x_0 \sim \mathcal{N}(0, P_0) \tag{3.10c}$$

$$w_t \sim \mathcal{N}(0, Q_t) \tag{3.10d}$$

$$e_t \sim \mathcal{N}(0, R_t) \tag{3.10e}$$

Here, P_0 is the initial state covariance matrix, *i.e.* the uncertainty of x_0. For that case it can be shown that procedure (3.9) becomes the Kalman Filter (KF) [Kalman, 1960] which is a Minimum Variance (MV) and the Best Linear Unbiased Estimator (BLUE). The equivalent formulation of (3.8) in the linear case becomes

$$\begin{aligned}\hat{x}_{0:N}^{\text{MV}} &= \arg\min_{x_{0:N}} \; \|x_0\|_{P_0}^2 + \sum_{t=1}^{N} \|y_t - Hx_t\|_{R_t}^2 + \|x_t - Fx_{t-1}\|_{Q_t}^2 \\ &= \arg\min_{x_{0:N}} \; \|x_0\|_{P_0}^2 + \sum_{t=1}^{N} \|e_t\|_{R_t}^2 + \|w_t\|_{Q_t}^2 \end{aligned} \tag{3.11}$$

which is a weighted least squares problem. Here, the notation $\|x\|_P$ is P^{-1}–weighted norm of x, $\|x\|_P = \sqrt{x^T P^{-1} x}$. If all the measurements are available at the estimation time, the solution to (3.11) can be obtained with the Kalman smoother. If the model is not linear, some approximate solutions to solve (3.9) must be applied, where Extended Kalman Filter (EKF) [Kailath et al., 2000] and Particle Filter (PF) [Gordon et al., 1993] are the most common approaches.

The state estimation method described above is basically the sensor fusion problem, *i.e.* by using the measurements from different sensors, $y_{1:N}$, and using the mathematical description of the form (3.2) or (3.3), the best possible estimate of the states, $\hat{x}_{0:N}$, is obtained by filtering or smoothing.

3.2 SAR in the Sensor Fusion Framework

In this context, SAR images or raw radar data can be seen as measurements that carry information about the flying platform's states and can be utilised in the sensor fusion. This principle is illustrated in Figure 3.1. In the top figure a traditional approach to SAR auto-focusing is depicted. Navigation data are used only for the initial image creation and auto-focusing is performed with image processing methods. In the middle and bottom figures, a sensor fusion block is used to estimate the best possible estimate of the navigation states and in turn SAR images, given all the available information. In the decentralised fusion approach information from the SAR processing is the complete image, while in the centralised approach, raw radar data is used.

In the model above it is assumed that the measurements are available for each time instant. In the centralised sensor fusion approach this could be achieved, as will be demonstrated in Chapter 6, but in the decentralised approach, where only the complete image is available some other kind of "measurement" must be used. Since we are trying to focus the images, it is natural to define this measurement as "how focused the image is" which will be the function of the whole image and in turn of the whole unknown platform's trajectory. As mentioned above, the sensor fusion framework is a very flexible approach, where sensors can be added or removed, they can work in different sampling rates or describe different states. It is even possible to add scalar valued terms that are functions of the states or the measurements and constraints of different kinds in the optimisation criterion (3.8) or (3.11).

Given the measurement and dynamic model as described above, the information from the SAR images can now be included in the optimisation problem. With the possibility to include extra terms in the optimisation criterion, a solution to the sensor fusion problem with SAR images included is to solve the following

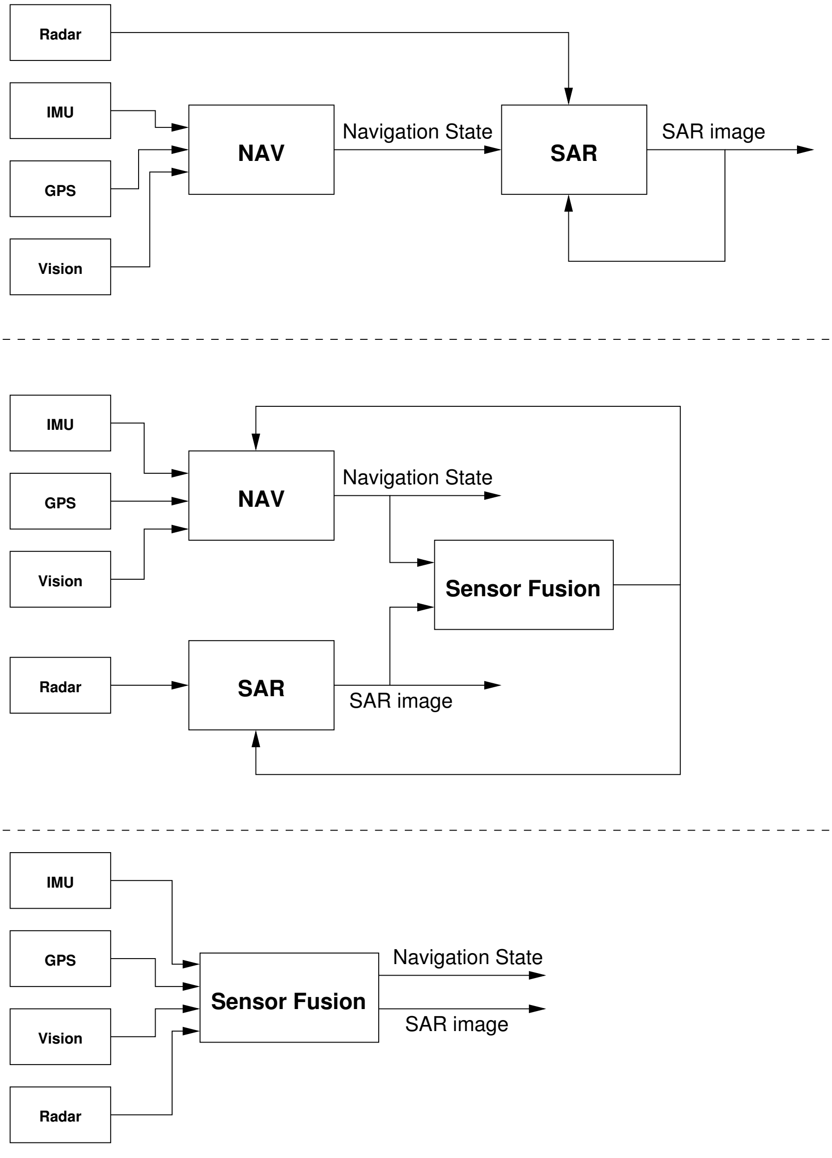

Figure 3.1: *Top: SAR architecture where navigation data is used in an open-loop manner. Middle: SAR architecture where navigation and SAR data are used together in a decentralised sensor fusion framework. Bottom: SAR architecture where navigation and SAR data are used together in a centralised sensor fusion framework.*

minimisation problem

$$\min_{x_0,\ w_{1:N}} \ \gamma_F F(x_{0:N}) + \gamma_s \left(\|x_0\|^2_{P_0} + \sum_{t=1}^{N} \| \underbrace{y_t - h(x_t)}_{e_t} \|^2_{R_t} + \|w_t\|^2_{Q_t} \right) \tag{3.12a}$$

subject to

$$x_{t+1} = f(x_t, w_t) \tag{3.12b}$$

where γ_F and γ_s are weights ($\gamma_F + \gamma_s = 1$, $\gamma_F \geq 0$, $\gamma_s \geq 0$) and $t \in \{0 : N\}$. Here the focus measure $F(\cdot)$ is the function that assumes its minimum for the most focused image. In Chapter 4 some possible functions used for this purpose will be evaluated.

3.3 System Model

As mentioned earlier for the sensor fusion framework to be applied a dynamical model of the aircraft and measurement models of the sensors must be defined. In its simplest form, a 3-DOF model of the aircraft can be expressed as [Farrell and Barth, 1999]

$$\dot{X}_t = v_t^X \tag{3.13a}$$
$$\dot{Y}_t = v_t^Y \tag{3.13b}$$
$$\dot{Z}_t = v_t^Z \tag{3.13c}$$
$$\dot{v}_t^X = a_t^X \tag{3.13d}$$
$$\dot{v}_t^Y = a_t^Y \tag{3.13e}$$
$$\dot{v}_t^Z = a_t^Z \tag{3.13f}$$
$$\dot{a}_t^X = w_t^{aX} \tag{3.13g}$$
$$\dot{a}_t^Y = w_t^{aY} \tag{3.13h}$$
$$\dot{a}_t^Z = w_t^{aZ} \tag{3.13i}$$

where X, Y, Z are positions of the aircraft, $v^{\{X,Y,Z\}}$ are the aircraft's velocities, $a^{\{X,Y,Z\}}$ are the acceleration and $w^{a\{X,Y,Z\}}$ is the unknown external jerk. These states of the aircraft describe pure translational motion and are expressed in some global coordinate frame, called world coordinate frame, with an arbitrary origin. There is another coordinate frame which is important and it is the navigation frame. The navigation frame is attached to the aircraft and its axis are aligned with the global frame, so there is no rotation between these frames. If these two frames were the only frames considered (*i.e.* the aircraft does not rotate) the dynamics above will be sufficient. However, since all modern inertial measuring equipment is strapped-down in the aircraft, the measurements obtained from these will be expressed in the so called body frame of the aircraft. This frame is attached to the aircraft (it has the same origin as the navigation frame) and its axis are aligned with the aircraft, *i.e.* it rotates with the aircraft. To describe the rotation of the body frame relative to the navigation (and global) frame, and obtain the full 6-DOF dynamic system model, we must introduce a way to describe rotations between different frames. Here, two possible ways will be described, Euler angles or quaternions.

3.3.1 Euler Angles

Euler angles ϕ, θ and ψ are called roll, pitch and yaw angle of the aircraft and these describe the rotation of the body frame relative to the navigation frame [Shuster, 1993]. This rotation is in matrix form expressed as (with notation $s. = \sin(\cdot)$ and $c. = \cos(\cdot)$)

$$C_b^n = \begin{bmatrix} c_\theta c_\psi & -c_\theta s_\psi & s_\theta \\ s_\phi s_\theta c_\psi + c_\phi s_\psi & -s_\phi s_\theta s_\psi + c_\phi c_\psi & -s_\phi c_\theta \\ -c_\phi s_\theta c_\psi + s_\phi s_\psi & c_\phi s_\theta s_\psi + s_\phi c_\psi & c_\phi c_\theta \end{bmatrix} \tag{3.14}$$

This matrix is valid for the specific order of rotations about fixed axis (in this case navigation frame), namely yaw-pitch-roll. If another order is used the rotation matrix will be different, since the rotation operation is not commutative. Since rotation matrices are orthonormal, the inverse rotation, C_n^b, is calculated as $C_n^b = (C_b^n)^T$. Note that the term Euler angles is normally used for a different rotation order and the order used here is called roll-pitch-yaw. However, here these terms are considered equivalent.

The dynamics of the Euler angles is

$$\dot{\phi}_t = \omega_t^X + \sin(\phi_t)\tan(\theta_t)\omega_t^Y - \cos(\phi_t)\tan(\theta_t)\omega_t^Z \tag{3.15a}$$

$$\dot{\theta}_t = \cos(\phi_t)\omega_t^Y + \sin(\phi_t)\omega_t^Z \tag{3.15b}$$

$$\dot{\psi}_t = -\frac{\sin(\phi_t)}{\cos(\theta_t)}\omega_t^Y + \frac{\cos(\phi_t)}{\cos(\theta_t)}\omega_t^Z \tag{3.15c}$$

$$\dot{\omega}_t^X = w_t^{\omega X} \tag{3.15d}$$

$$\dot{\omega}_t^Y = w_t^{\omega Y} \tag{3.15e}$$

$$\dot{\omega}_t^Z = w_t^{\omega Z} \tag{3.15f}$$

where $\omega^{\{X,Y,Z\}}$ are the angular velocities of the aircraft measured in the body frame and $w^{\omega\{X,Y,Z\}}$ are the unknown external angular accelerations. We immediately see that there exists a singularity in the dynamics for $\theta_t = \pm\pi/2$. In this case the roll and the yaw angles are undefined. Fortunately, there is another representation of the rotations in $\mathbb{R}^3$, with the help of the quaternions, that does not suffer from these limitations.

3.3.2 Quaternions

Quaternions are defined in four dimensional space as $q = [q_0, q_1, q_2, q_3]^T, q_i \in \mathbb{R}$. To represent the rotation in $\mathbb{R}^3$, q is constrained to the unit sphere, *i.e.* $q^T q = 1$ [Kuipers, 1999, Shuster, 1993]. The transformation from Euler angles to quaternions is defined as

$$q_0 = \cos(\phi/2)\cos(\theta/2)\cos(\psi/2) + \sin(\phi/2)\sin(\theta/2)\sin(\psi/2) \tag{3.16a}$$
$$q_1 = \sin(\phi/2)\cos(\theta/2)\cos(\psi/2) - \cos(\phi/2)\sin(\theta/2)\sin(\psi/2) \tag{3.16b}$$
$$q_2 = \cos(\phi/2)\sin(\theta/2)\cos(\psi/2) + \sin(\phi/2)\cos(\theta/2)\sin(\psi/2) \tag{3.16c}$$
$$q_3 = \cos(\phi/2)\cos(\theta/2)\sin(\psi/2) - \sin(\phi/2)\sin(\theta/2)\cos(\psi/2) \tag{3.16d}$$

and from quaternions to Euler angles as

$$\begin{bmatrix} \phi \\ \theta \\ \psi \end{bmatrix} = \begin{bmatrix} \operatorname{atan2}(2(q_0 q_1 + q_2 q_3), 1 - 2(q_1^2 + q_2^2)) \\ \arcsin(2(q_0 q_2 - q_3 q_1)) \\ \operatorname{atan2}(2(q_0 q_3 + q_1 q_2), 1 - 2(q_2^2 + q_3^2)) \end{bmatrix} \tag{3.17}$$

where $\operatorname{atan2}(\,\cdot\,,\cdot\,)$ is arctan function defined for all four quadrants.

The dynamics of the quaternions can be expressed as

$$\dot{q}_t = \frac{1}{2} \underbrace{\begin{bmatrix} 0 & -\omega_t^X & -\omega_t^Y & -\omega_t^Z \\ \omega_t^X & 0 & \omega_t^Z & -\omega_t^Y \\ \omega_t^Y & -\omega_t^Z & 0 & \omega_t^X \\ \omega_t^Z & \omega_t^Y & -\omega_t^X & 0 \end{bmatrix}}_{S(\omega_t)} q_t = \frac{1}{2} \underbrace{\begin{bmatrix} -q_1 & -q_2 & -q_3 \\ q_0 & -q_3 & q_2 \\ q_3 & q_0 & -q_1 \\ -q_2 & q_1 & q_0 \end{bmatrix}}_{\tilde{S}(q_t)} \omega_t \tag{3.18}$$

We see that the dynamics is still non-linear, but the non-linearities are much simpler than for Euler angles (it is actually bilinear).

The rotation matrix corresponding to (3.14), but expressed in quaternions, is

$$C_b^n = \begin{bmatrix} q_0^2 + q_1^2 - q_2^2 - q_3^2 & 2(q_1 q_2 + q_0 q_3) & 2(-q_0 q_2 + q_1 q_3) \\ 2(q_1 q_2 - q_0 q_3) & q_0^2 - q_1^2 + q_2^2 - q_3^2 & 2(q_2 q_3 + q_0 q_1) \\ 2(q_1 q_3 + q_0 q_2) & 2(-q_0 q_1 + q_2 q_3) & q_0^2 - q_1^2 - q_2^2 + q_3^2 \end{bmatrix} \tag{3.19}$$

3.3.3 Measurements

So far we have defined the dynamics of the system, in this case a flying platform. In order to get a complete model, we also need a measurement equation of the form (3.1b) or (3.2b), where the latter is the most common and will be used in the rest of the thesis. For the models above the natural measurements are the accelerations and angular rates which are measured with accelerometers and rate gyros. These are often combined in an inertial measurement unit (IMU). The IMU is strapped to the platform and hence aligned with the platform's body coordinate frame. Hence, measurements that come from the IMU are accelerations and angular rates expressed in the body coordinate frame. In the dynamics (3.13) above, accelerations are assumed to be relative navigation frame. This leads to a measurement equation of the form

$$a_t^m = C_b^n(a_t - \mathbf{g}) + e_t^a \tag{3.20}$$

where the superscript m stands for measured and $\mathbf{g} = [0,\ 0,\ -9.81]^T$ since accelerometers measure gravitation force as well. The measurement equation for the angular rates is simply

$$\omega_t^m = \omega_t + e_t^\omega \tag{3.21}$$

e_t^a and e_t^ω are white Gaussian noises with variances R^a and R^ω.

3.3.4 Specialisation of the Model Used Here

In the setup here, the platform is assumed to be flying in a fairly straight trajectory during image acquisition. Since the origin and the orientation of the global coordinate frame is arbitrary it can easily be placed aligned with the trajectory, *i.e.* the X-axis is aligned with the along-track (or azimuth) direction, the Y-axis is aligned with the cross-track (or range) direction and the Z-axis is pointing upwards. Since rotation of the platform is also assumed negligible during image acquisition no rotation dynamics is needed (or at least can be approximated with zero). Due to the inertial properties of the flying platform, one more simplification we can do is to assume that the flying altitude is constant. With all these assumptions, the following 2-DOF dynamics can be used:

$$\dot{X}_t = v_t^X \tag{3.22a}$$
$$\dot{Y}_t = v_t^Y \tag{3.22b}$$
$$\dot{v}_t^X = a_t^X \tag{3.22c}$$
$$\dot{v}_t^Y = a_t^Y \tag{3.22d}$$
$$\dot{a}_t^X = w_t^X \tag{3.22e}$$
$$\dot{a}_t^Y = w_t^Y \tag{3.22f}$$

where X and Y are the horizontal positions of the aircraft, X is the position in the azimuth direction and Y is the position in range direction, v^X and v^Y are the velocities in the X- and Y-directions respectively and a^X and a^Y are the accelerations in X- and Y-directions respectively. This model is discretised into (T_s is the sampling time):

$$X_{t+1} = X_t + T_s v_t^X + \frac{T_s^2}{2} a_t^X + \frac{T_s^3}{6} w_t^X \tag{3.23a}$$
$$Y_{t+1} = Y_t + T_s v_t^Y + \frac{T_s^2}{2} a_t^Y + \frac{T_s^3}{6} w_t^Y \tag{3.23b}$$
$$v_{t+1}^X = v_t^X + T_s a_t^X + \frac{T_s^2}{2} w_t^X \tag{3.23c}$$
$$v_{t+1}^Y = v_t^Y + T_s a_t^Y + \frac{T_s^2}{2} w_t^Y \tag{3.23d}$$
$$a_{t+1}^X = a_t^X + T_s w_t^X \tag{3.23e}$$
$$a_{t+1}^Y = a_t^Y + T_s w_t^Y \tag{3.23f}$$

where $w_t^{\{X,Y\}}$ are modelled as Gaussian white noise. This dynamics is purely linear and time invariant and can be written in the form

$$x_{t+1} = Fx_t + Gw_t \tag{3.24a}$$

$$F = \begin{bmatrix} I_2 & T_s I_2 & \frac{T_s^2}{2} I_2 \\ 0_{2\times 2} & I_2 & T_s I_2 \\ 0_{2\times 2} & 0_{2\times 2} & I_2 \end{bmatrix} \tag{3.24b}$$

$$G = \begin{bmatrix} \frac{T_s^3}{6} I_2 \\ \frac{T_s^2}{2} I_2 \\ T_s I_2 \end{bmatrix} \tag{3.24c}$$

In most cases the measurements that are available are positions and velocities, usually from some Global Navigation Satellite System (GNSS), like GPS, and accelerations from the IMU. This gives the measurement equation in the form

$$y_t = I_6 x_t + e_t \tag{3.25}$$

Given the dynamics and the measurements the Kalman Filter can be used to estimate x_t, giving $\hat{x}_t$ and the corresponding covariance P_t. Since the model is purely linear and the noise is assumed to be white and Gaussian, this filter is optimal and its estimate is the best we can accomplish given the measurements.

3.3.5 Stationary Estimate Accuracy

The covariance of the estimate, due to the fact that the system is time invariant and linear, will converge to the stationary covariance $\bar{P}$ which can be calculated as [Gustafsson, 2010]

$$\bar{P} = F\bar{P}F^T - F\bar{P}H^T(H\bar{P}H^T + R)^{-1}H\bar{P}F^T + GQG^T \tag{3.26}$$

where F and G are defined in (3.24), and H is defined in (3.25). For a typical navigation sensor used in an UAV, the accuracy for these parameters (assumed to be measurement noise) can be summarised according to Table 3.1 and Q, which represents disturbance on the states like wind turbulence, will be taken here as diag$\{0.25,\ 0.25\}$ [m/s^2]. With these values stationary accuracy is given in the third column in Table 3.1. The stationary accuracy of the states will be used to define the range of the initial values for the estimation procedures with SAR information included. Because it is interesting to evaluate the performance of the estimation procedure with only inertial measurements and SAR images, the positions and velocities will not be used as measurements.

Parameter	Accuracy (1σ)	Stationary accuracy (1σ)
Position	3 m	0.093 m
Velocity	0.4 m/s	0.012 m/s
Acceleration	0.06 m/s^2	0.015 m/s^2

Table 3.1: *Accuracy and stationary accuracy for the navigation parameters.*

3.4 Some Estimator Performance Measures

In the chapters to follow, the sensor fusion methods described above will be evaluated on different SAR images and with some different measurements. To achieve this, some different performance measures are needed to evaluate both the state estimation and image quality. If $\hat{x} = [\hat{x}_1, \ldots, \hat{x}_N]^T$, are unbiased estimates of the scalar parameter x, Root Mean Square Error (RMSE), defined as

$$RMSE(\hat{x}) = \sqrt{\frac{\sum_{k=1}^{N} (\hat{x}_k - x)^2}{N}} \tag{3.27}$$

is one popular measure of the accuracy, *i.e.* it is the estimate of the standard deviation.

To assess the quality of the SAR images obtained with different methods the power of the error image can be used. This can be defined as

$$E_I = \frac{\sum_{i=1}^{M} \sum_{j=1}^{N} |\hat{I}_{ij} - I_{ij}|^2}{MN} \tag{3.28}$$

where $\hat{I}$ is the $M \times N$ complex SAR image obtained with the estimation procedure and I is the perfect focused SAR image, *i.e.* created with true trajectory.

4

Measuring Focus

In optimisation criterion (3.12a), a focus measure $F(\cdot)$ is used to incorporate the information from the SAR images. The focus measure is a function of the whole trajectory $x_{0:N}$ since the SAR image is a function of the same. In Huang and Jing [2007] several measures of the image focus are evaluated. Two measures that perform well according to this paper are Sum-Modified-Laplacian and Tenengrad and these two measures will be analysed in this chapter. Also some classical image focus measures like image entropy are evaluated. The evaluation will be performed on both optical and SAR images.

4.1 Focus Measures

4.1.1 Sum-Modified-Laplacian

The Sum-Modified-Laplacian focus measure is defined as

$$\begin{aligned} \nabla^2_{\mathrm{ML}} I_{ij} =& |2I_{ij} - I_{(i-1)j} - I_{(i+1)j}| + \\ & |2I_{ij} - I_{i(j-1)} - I_{i(j+1)}| \end{aligned} \tag{4.1a}$$

$$\mathrm{SML}(I) = \sum_{i=2}^{M-1} \sum_{j=2}^{N-1} \nabla^2_{\mathrm{ML}} I_{ij} \cdot \mathbf{I}_{[\nabla^2_{\mathrm{ML}} I_{ij} \geq T]}(\nabla^2_{\mathrm{ML}} I_{ij}) \tag{4.1b}$$

where I_{ij} is the $M \times N$ image grey-scale intensity for pixel coordinate (i, j), $\mathbf{I}$ is the indicator function, and T is the threshold value. This measure has its maximum for the most focused images. Since (3.12a) is a minimisation criterion, SML can be inverted or negated to fit into this criterion.

4.1.2 Tenengrad

The Tenengrad focus measure is defined as

$$\mathrm{TG}(I) = \sum_{i=2}^{M-1} \sum_{j=2}^{N-1} S_{ij}^2 \cdot \mathbf{I}_{[S_{ij}>T]}(S_{ij}) \tag{4.2}$$

where S_{ij} is the Sobel gradient in pixel coordinate (i, j),

$$S_{ij} = \sqrt{(S_{ij}^r)^2 + (S_{ij}^c)^2} \tag{4.3}$$

where S^r and S^c are row and column Sobel gradients respectively, T is the threshold value and I is the $M \times N$ image. The Sobel gradients are obtained by convolving the image with the row and column Sobel kernels D^r and D^c,

$$S^r = D^r * I \tag{4.4a}$$

$$S^c = D^c * I \tag{4.4b}$$

$$D^r = \begin{bmatrix} -1 & 0 & 1 \\ -2 & 0 & 2 \\ -1 & 0 & 1 \end{bmatrix} \tag{4.4c}$$

$$D^c = \begin{bmatrix} -1 & -2 & -1 \\ 0 & 0 & 0 \\ 1 & 2 & 1 \end{bmatrix} \tag{4.4d}$$

Just as SML, TG has it maximum for the most focused images. This problem is circumvented in the same way as for the SML.

4.1.3 Discrete Cosine Transform

Further, the Discrete Cosine Transform (DCT) can be used to measure image focus, see Kristan et al. [2006]. The main idea is that focused images have higher frequency components than unfocused images. The focus measure based on DCT is defined as

$$\mathrm{DCT}(I) = 1 - \frac{\sum_{\omega=1}^{T} \sum_{\nu=1}^{T} |D(\omega,\nu)|^2}{(\sum_{\omega=1}^{T} \sum_{\nu=1}^{T} |D(\omega,\nu)|)^2} \tag{4.5}$$

where

$$D(\omega,\nu) = \alpha_\omega \alpha_\nu \sum_{i=0}^{M-1} \sum_{j=0}^{N-1} I_{ij} \cos\left(\frac{\pi(2i+1)\omega}{2M}\right) \cos\left(\frac{\pi(2j+1)\nu}{2N}\right) \tag{4.6a}$$

$$\alpha_\omega = \begin{cases} \frac{1}{\sqrt{M}}, & \omega = 0 \\ \sqrt{\frac{2}{M}}, & 1 \le \omega \le M-1 \end{cases} \tag{4.6b}$$

$$\alpha_\nu = \begin{cases} \frac{1}{\sqrt{N}}, & \nu = 0 \\ \sqrt{\frac{2}{N}}, & 1 \le \nu \le N-1 \end{cases} \tag{4.6c}$$

is the Discrete Cosine Transform of the image I and T is the threshold. Even DCT behaves as TG and SML, *i.e.* it attains the maximum value for the sharpest images.

4.1.4 Entropy

Another measure of the image focus is image entropy calculated as

$$E_1(I) = -\sum_{k=1}^{256} p_k \log_2(p_k) \tag{4.7}$$

where p_i is an approximated grey level distribution of the $M \times N$ grey-scale image. A grey-scale SAR image is taken as the amplitude image $I_{ij} = |\tilde{I}_{ij}|$, where $\tilde{I}_{ij}$ is the complex-valued SAR image. p_i can be obtained from the image histogram, calculated as

$$p_k = \frac{\left\{\# \text{ of pixel values } |\tilde{I}_{ij}|\right\} \in [k-1, k]}{MN} \tag{4.8a}$$

$$k \in [1, 256] \tag{4.8b}$$

The more focused the image is, the higher the entropy is [Ferzli and Karam, 2005], exactly as for the previous mentioned measures. Note however that entropy measure is primarily used for optical images, whose defocus (or rather unsharpness) have different nature from the defocus of SAR images. In Section 4.3 it will be shown that the entropy for a SAR image is lower the more focused the image is. Example histograms and entropy values for the images in Figure 2.5 are given in Figure 4.1.

An alternative definition of entropy (and more frequently used in the SAR context) is [Yegulalp, 1999, Xi et al., 1999, Morrison and Munson, 2002],

$$E_2(\tilde{I}) = -\sum_{i=1}^{M}\sum_{j=1}^{N} p_{ij} \ln(p_{ij}) \tag{4.9a}$$

$$p_{ij} = \frac{|\tilde{I}_{ij}|^2}{\sum_{i=1}^{M}\sum_{j=1}^{N} |\tilde{I}_{ij}|^2} \tag{4.9b}$$

This entropy, on the other hand, will have its minimum for both optical and SAR images, as will be shown in the evaluations in Sections 4.2 and 4.3.

4.2 Evaluation on Test Optical Image

For the purpose of evaluation of the different focus measures, the image in Figure 4.2 is used. The evaluation will be performed for different thresholds where it is applicable and for different degrees of defocus (or unsharpness).

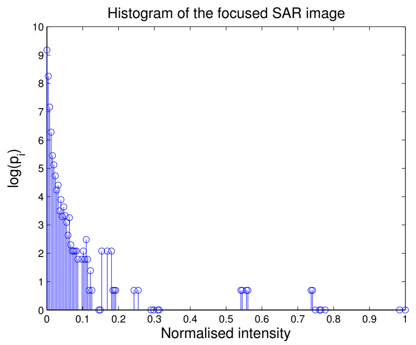

(a) *Histogram of the focused image.* $E_1(I) = 2.66$.

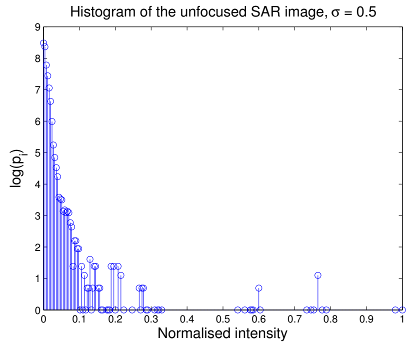

(b) *Histogram of the unfocused image with* $\sigma = 0.5$. $E_1(I) = 3.32$.

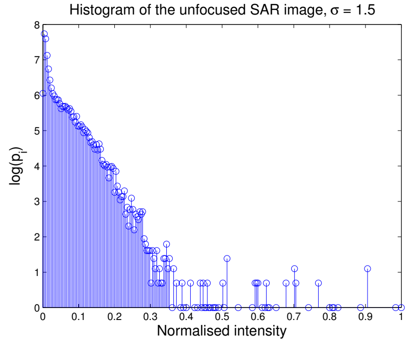

(c) *Histogram of the unfocused image with* $\sigma = 1.5$. $E_1(I) = 5.72$.

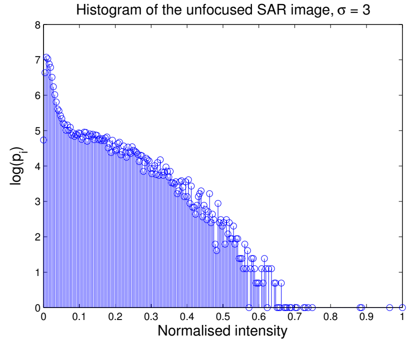

(d) *Histogram of the unfocused image with* $\sigma = 3$. $E_1(I) = 7.47$.

Figure 4.1: *Histograms for the images in Figure 2.5 and corresponding entropy 1 values. Note the log-scale on* y*-axis.*

Figure 4.2: *Test image used for evaluation of the focus measures. Image is courtesy of University of Southern California, Los Angeles, California, USA.*

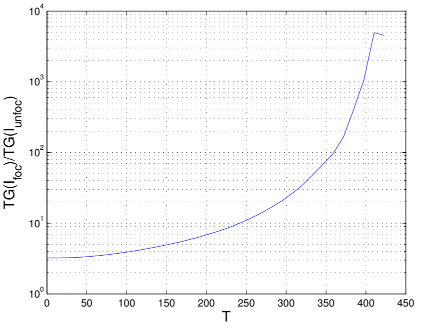

(a) $TG(I_{foc})/TG(I_{unfoc})$ *as a function of the threshold, log-scale on the* y*-axis.*

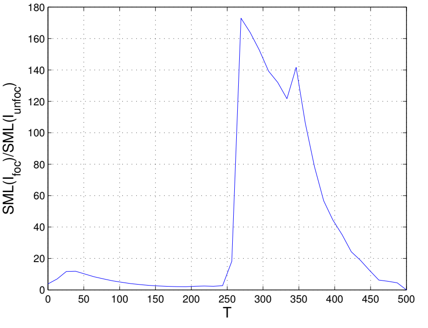

(b) $SML(I_{foc})/SML(I_{unfoc})$ *as a function of the threshold.*

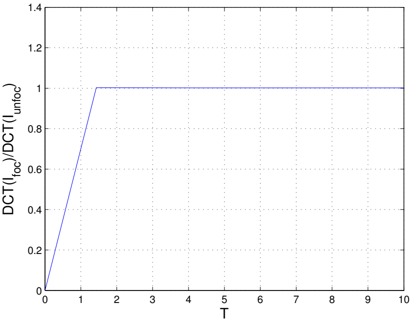

(c) $DCT(I_{foc})/DCT(I_{unfoc})$ *as a function of the threshold.*

Figure 4.3: *Ratio of the different focus measures for focused and unfocused optical images as a function of the threshold.*

4.2.1 Threshold Dependence

In order to evaluate the performance of the different measures, the ratio between focused and unfocused images, $F(I_{\text{focused}})/F(I_{\text{unfocused}})$, is plotted for the test image as a function of threshold T (F is one of TG, SML or DCT). Unfocusing is performed with the Gaussian low-pass filter kernel with size 5×5 pixels and with standard deviation $\sigma = 1.5$. The results are plotted in Figure 4.3. Since entropy does not depend on the threshold, only one value is obtained for this case, $E_1(I_{\text{foc}})/E_1(I_{\text{unfoc}}) = 6.99/6.80 = 1.03$ and $E_2(I_{\text{foc}})/E_2(I_{\text{unfoc}}) = 12.40/12.42 = 0.99$.

4.2.2 Blur Kernel Dependence

In Figure 4.4 the ratio $F(I_{\text{focused}})/F(I_{\text{unfocused}})$ is plotted for different standard deviations of the 5×5 Gaussian low-pass kernel, in the range $\sigma \in [0,\ 4]$. Higher variance will yield a less focused image. For the measures that depends on the threshold, the threshold values are chosen based on the results from Section 4.2.1, *i.e.* the threshold values that give high ratio between focused and unfocused images. For this particular evaluation they are $T_{\mathrm{TG}} = 350$, $T_{\mathrm{SML}} = 270$ and $T_{\mathrm{DCT}} = 2$.

4.3 Evaluation on Test SAR Images

For SAR images, basically the same evaluation as above will be performed, but in this case defocusing will be caused by the different trajectory errors, which is the main reason for SAR image defocusing.

4.3.1 Threshold Dependence

To get a feeling for how different focus measures perform on SAR images as a function of the threshold, the same evaluation is done as in Section 4.2.1. The example SAR image used in the evaluation is in Figure 4.5. Defocusing is here obtained with adding range direction noise with standard deviation $\sigma = 1.5$. Results are plotted in Figure 4.6. Exactly as above, since entropy does not depend on the threshold, there is only one value for each σ. In particular, $\sigma = 1.5$ gives $E_1(I_{\mathrm{foc}})/E_1(I_{\mathrm{unfoc}}) = 1.91/5.12 = 0.37$ and $E_2(\tilde{I}_{\mathrm{foc}})/E_2(\tilde{I}_{\mathrm{unfoc}}) = 4.28/8.10 = 0.53$.

4.3.2 Position Blur Dependence

Another test of the focus measures that is performed is how they depend on the variance of the noise in the range direction for a given threshold, similar to the evaluation in Section 4.2.2. The simulation is performed with the same noise realisation, but different variances, *i.e.* position in range direction is

$$Y_t = \sqrt{Q} w_t \tag{4.10}$$

where w_t is $\mathcal{N}(0, 1)$ and $Q \in [0,\ 9]$ (standard deviation is between 0 and 3). The result is depicted in Figure 4.7. From these plots it can be noticed that DCT and entropy 2 measures behave as expected, *i.e.* the ratio between focused and unfocused image is monotonically increasing as a function of the standard deviation for DCT and decreasing for entropy 2 measure. For TG, SML and entropy 1, however, there is a difference between optical and SAR images. For optical images, all three measures will have their maxima for focused images, while for SAR images they will have their minima. This behaviour can be explained both by the look of the test image, two bright points and lot of dark area, and the nature of the SAR images, *i.e.* SAR images usually look like they are negative optical images and contain more dark areas than optical images.

In order to obtain an image which is more informative, a scene in Figure 4.8 is created. A smaller image is created to minimise the dark area. This image should be more representative for the SAR images. The simulation above is modified and the maximum value for the standard deviation of the noise is set to 1.5 instead of 3. This is done because the smaller image might cause rand effects which will

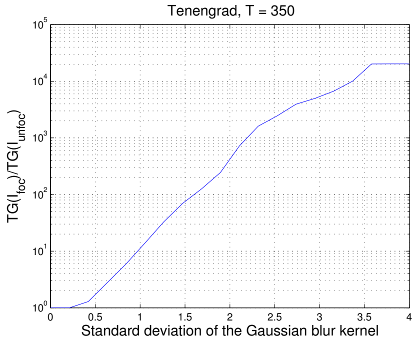

(a) $TG(I_{foc})/TG(I_{unfoc})$ *as a function of the standard deviation of the Gaussian blur kernel, log-scale on the y-axis.*

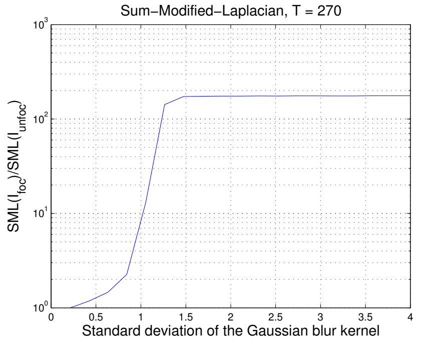

(b) $SML(I_{foc})/SML(I_{unfoc})$ *as a function of the standard deviation of the Gaussian blur kernel, log-scale on the y-axis.*

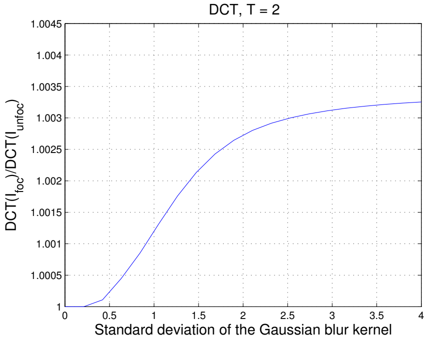

(c) $DCT(I_{foc})/DCT(I_{unfoc})$ *as a function of the standard deviation of the Gaussian blur kernel.*

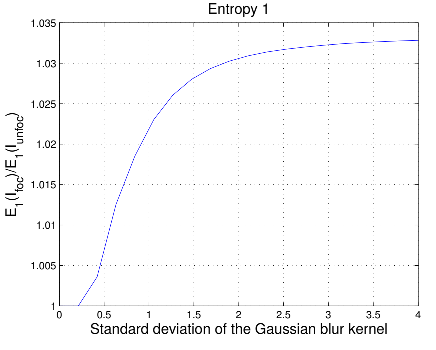

(d) $E_1(I_{foc})/E_1(I_{unfoc})$ *as a function of the standard deviation of the Gaussian blur kernel.*

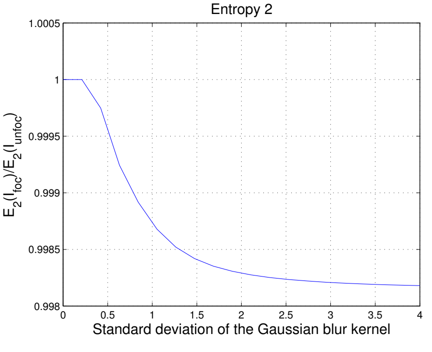

(e) $E_2(I_{foc})/E_2(I_{unfoc})$ *as a function of the standard deviation of the Gaussian blur kernel.*

Figure 4.4: *Ratio of the different focus measures for focused and unfocused optical images as a function of the standard deviation of the Gaussian blur kernel.*

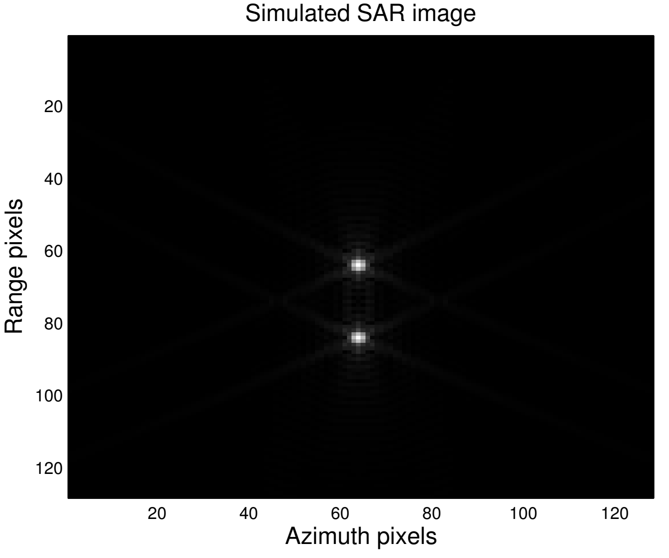

Figure 4.5: *Example SAR image used for evaluation of the focus measures.*

negatively influence the focus measures. The results are depicted in Figure 4.9. It can be noticed in these plots that TG and SML behaves as expected now, but SML has a highly nonconvex form. This indicates that SML might not be suitable measure for the SAR images. Entropy 2 and DCT behaves still as expected, and entropy 1, just as in the previous case, attains minimum for the most focused SAR image.

4.3.3 Evaluation on Perturbed Trajectory

In order to evaluate the focus measures behaviour for different trajectories on the simulated SAR images, simulations with different trajectory errors are performed. The trajectory is simulated with the model (3.24a) and trajectory errors consist of different incorrect initial conditions on velocity in azimuth direction, v_0^X, and acceleration in range direction, a_0^Y. The nominal initial values are chosen as $v_0^X = 100$ m/s and $a_0^Y = 0$ m/s^2 and acceleration error is varied between -0.045 and 0.045 m/s^2 and velocity error is varied between 99.962 and 100.038 m/s. Those values are chosen as 3σ-values, based on the results from Section 3.3. The noise, $w_t^{X/Y}$, is set to zero in these simulations, *i.e.* the trajectory is completely deterministic. This has been done in order to be able to illustrate focus measures in a two dimensional plot. On the other side, all focus measures, as functions of the state noise are convex and impose no problems in the minimisation step. In Figure 4.10 trajectory examples with some different acceleration and velocity errors are shown.

All five focus measures, TG with threshold value $T = 550$, SML with $T = 170$,

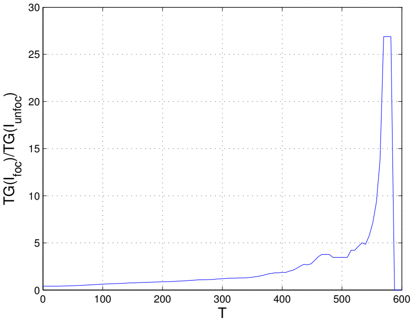

(a) $TG(I_{foc})/TG(I_{unfoc})$ *as a function of the threshold.*

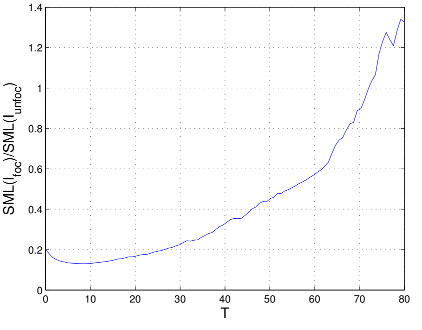

(b) $SML(I_{foc})/SML(I_{unfoc})$ *as a function of the threshold.*

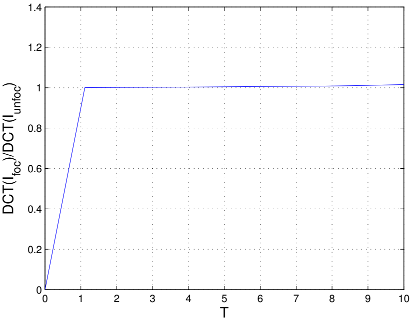

(c) $DCT(I_{foc})/DCT(I_{unfoc})$ *as a function of the threshold.*

Figure 4.6: *Ratio of the different focus measures for focused and unfocused SAR images as a function of the threshold.*

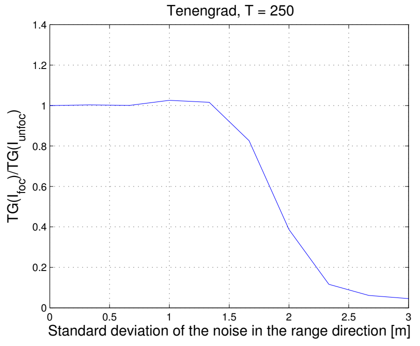

(a) *$TG(I_{foc})/TG(I_{unfoc})$ as a function of the standard deviation of the noise in the range direction.*

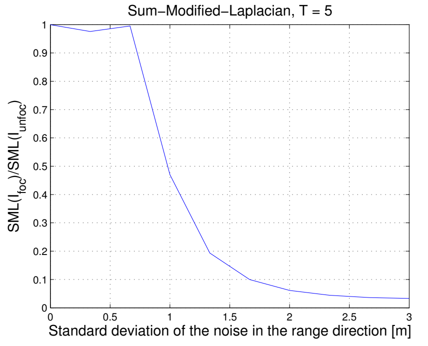

(b) *$SML(I_{foc})/SML(I_{unfoc})$ as a function of the standard deviation of the noise in the range direction.*

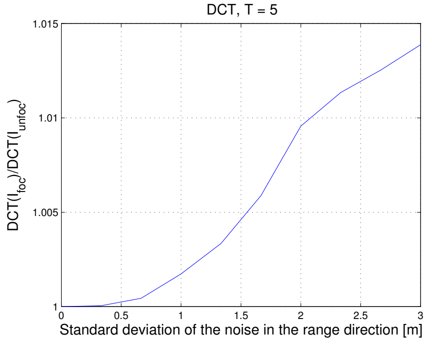

(c) *$DCT(I_{foc})/DCT(I_{unfoc})$ as a function of the standard deviation of the noise in the range direction.*

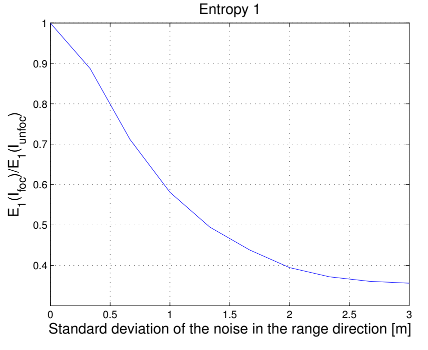

(d) *$E_1(I_{foc})/E_1(I_{unfoc})$ as a function of the standard deviation of the noise in the range direction.*

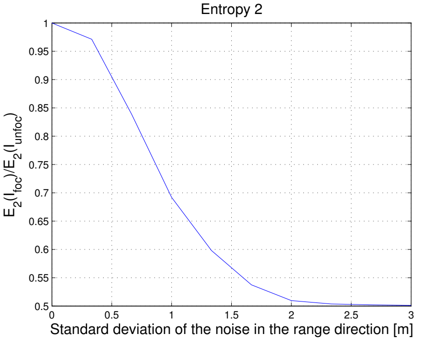

(e) *$E_2(I_{foc})/E_2(I_{unfoc})$ as a function of the standard deviation of the noise in the range direction.*

Figure 4.7: *Ratio of the different focus measures for focused and unfocused SAR images as a function of the standard deviation of the noise in the range direction.*

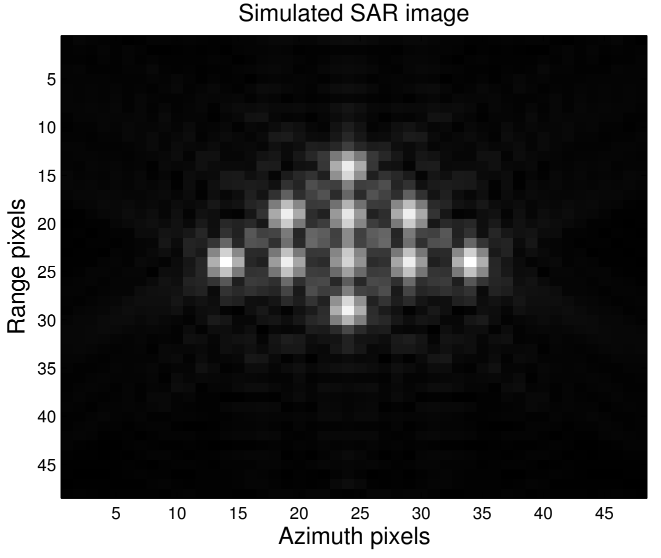

Figure 4.8: *Example SAR image with more informative scene.*

DCT with $T = 5$ and entropy measures 1 and 2, are compared on the image in Figure 4.8. The thresholds are chosen according to the results from the simulations in Section 4.3.1. Results are depicted in Figure 4.11 where $1\sigma-$, $2\sigma-$ and $3\sigma-$ standard deviations of the states from Section 3.3.5 are also drawn. The contours in the plots are the level curves of the focus measures as a function of the error in the initial states, v_0^X and a_0^Y. The level curves for the measures with the maximum for the correct values of the initial states, like TG or SML, are inverted.

Further, plots where only one parameter, v_0^X or a_0^Y, is varied are presented in Figure 4.12 (all measures are normalised between 0 and 1). From all these figures it looks like that all measures except entropy 2 have several local minima and are highly non-convex. We also see that TG and SML do not have minimum value for the correct velocity value and that DCT has its minimum in the wrong value of the acceleration. The entropy measures perform fairly well, and entropy 1 has much sharper global minimum than entropy 2. Based on this, the entropy 1 and the entropy 2 measures look as the most attractive measures since they behave good for the correct values of the states, they do not have any threshold to tune and entropy 2 is also smooth and convex.

The focus measures' performance is also tested on a more unstructured scene illustrated in Figure 4.13a. This scene is created by randomly placing 150 point targets and assigning them a random reflectivity. The focus measures for this scene are shown in Figure 4.13. Here it can be seen that the measures look even worse and not even the entropy 1 measure has its global minimum for the correct values of the states. Entropy 2 is however still convex and smooth in the vicinity of the correct values of the states, and is still the most promising alternative to

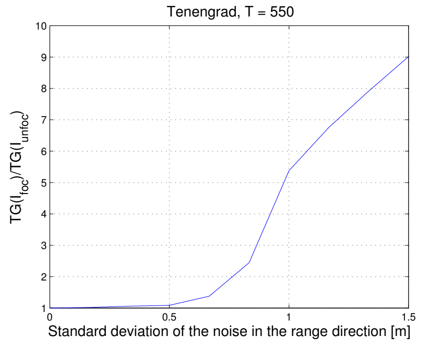

(a) *$TG(I_{foc})/TG(I_{unfoc})$ as a function of the standard deviation of the noise in the range direction.*

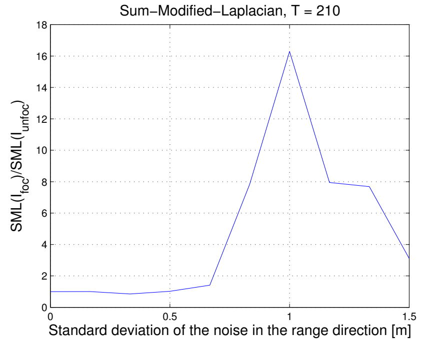

(b) *$SML(I_{foc})/SML(I_{unfoc})$ as a function of the standard deviation of the noise in the range direction.*

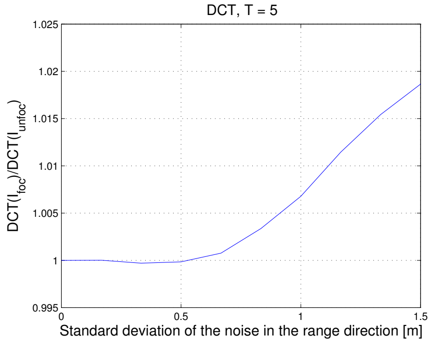

(c) *$DCT(I_{foc})/DCT(I_{unfoc})$ as a function of the standard deviation of the noise in the range direction.*

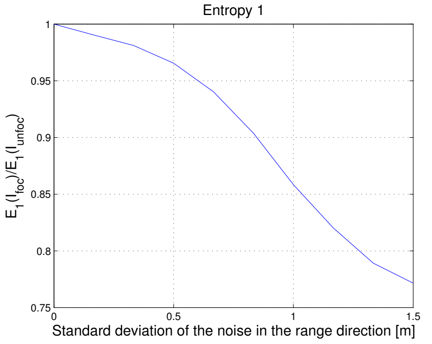

(d) *$E_1(I_{foc})/E_1(I_{unfoc})$ as a function of the standard deviation of the noise in the range direction.*

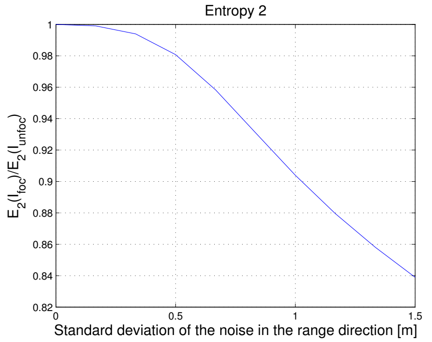

(e) *$E_2(I_{foc})/E_2(I_{unfoc})$ as a function of the standard deviation of the noise in the range direction.*

Figure 4.9: *Ratio of the different focus measures for focused and unfocused SAR images with more informative scene as a function of the standard deviation of the noise in the range direction.*

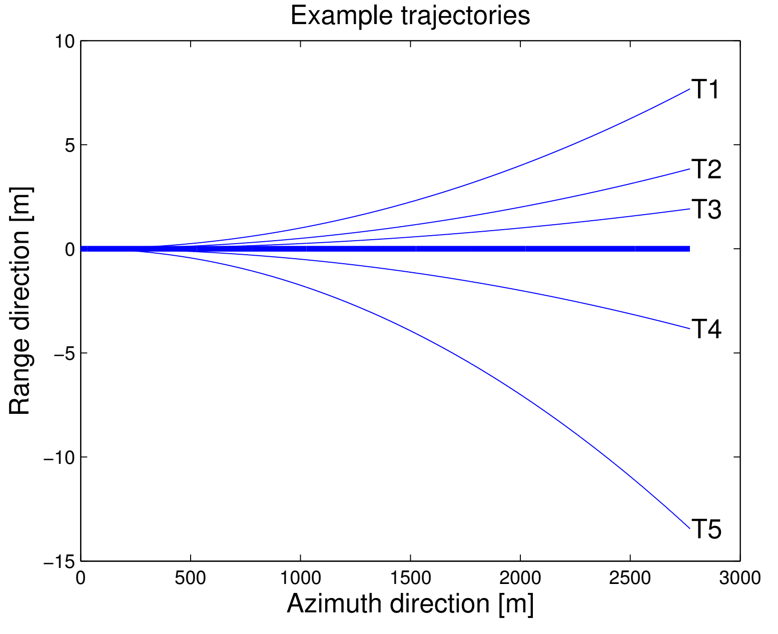

Figure 4.10: *Example trajectories: thick line: no errors in initial values; from above:* -0.005 m/s *velocity error and* 0.02 m/s^2 *acceleration error,* -0.01 m/s *velocity error and* 0.01 m/s^2 *acceleration error,* 0.005 m/s *velocity error and* 0.005 m/s^2 *acceleration error,* 0.02 m/s *velocity error and* -0.01 m/s^2 *acceleration error,* 0.005 m/s *velocity error and* -0.035 m/s^2 *acceleration error.*

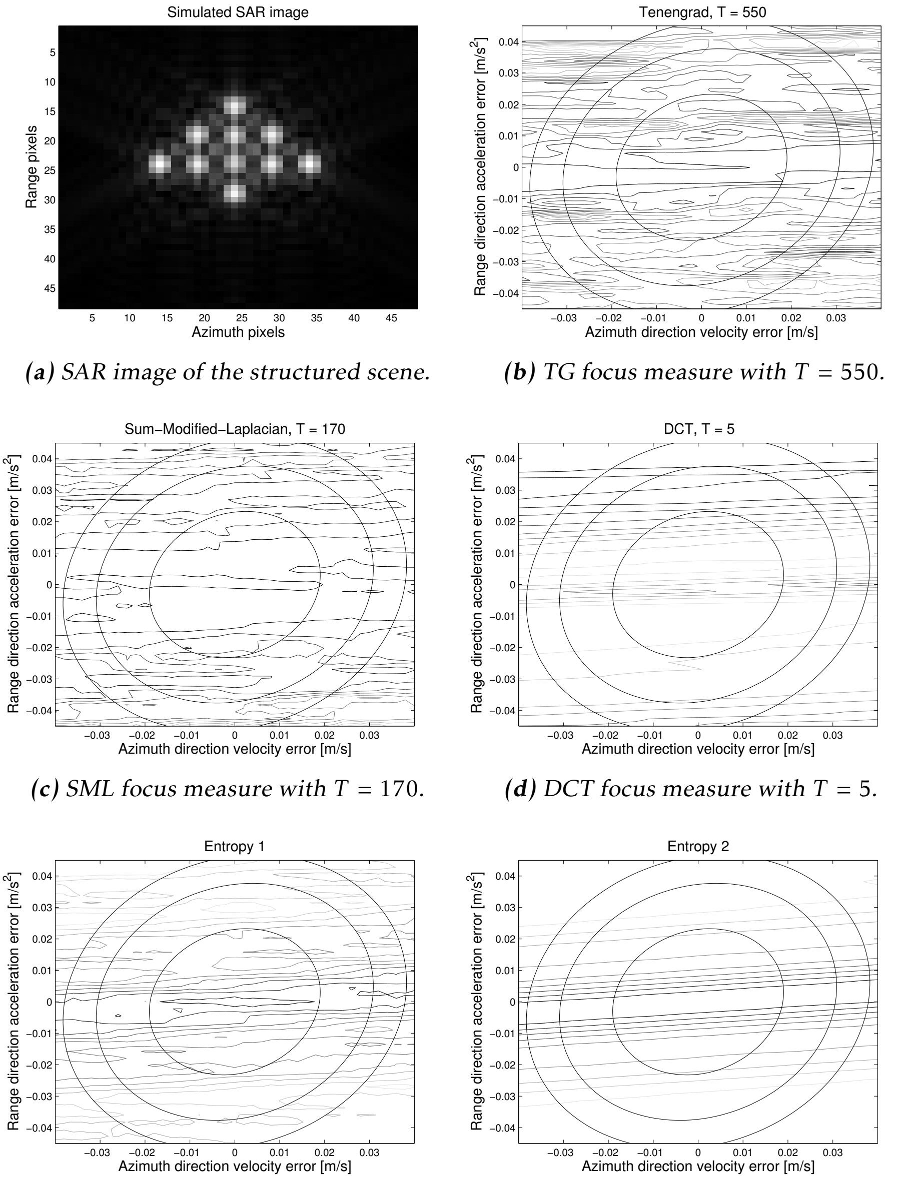

(a) *SAR image of the structured scene.*

(b) *TG focus measure with $T = 550$.*

(c) *SML focus measure with $T = 170$.*

(d) *DCT focus measure with $T = 5$.*

(e) *Entropy 1 focus measure.*

(f) *Entropy 2 focus measure.*

Figure 4.11: *Focus measures for the image with more informative structured scene. Standard deviations of the states are also drawn.*

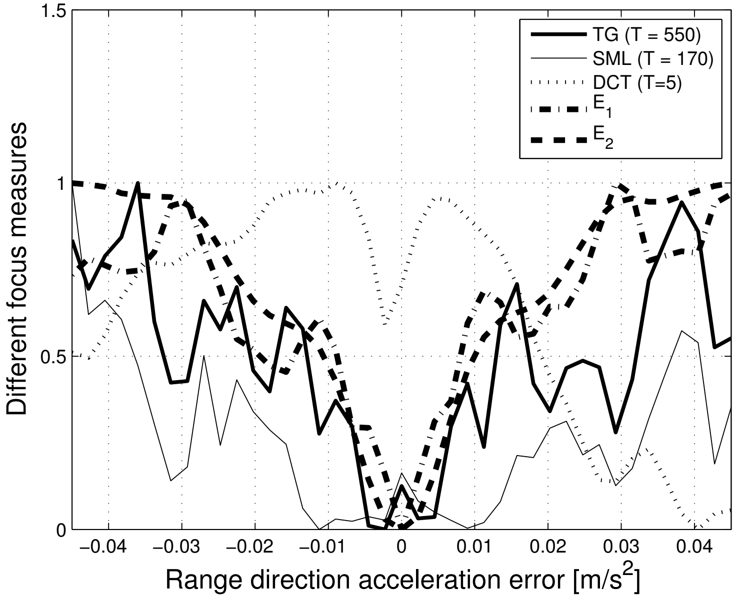

(a) *Focus measures with no velocity error.*

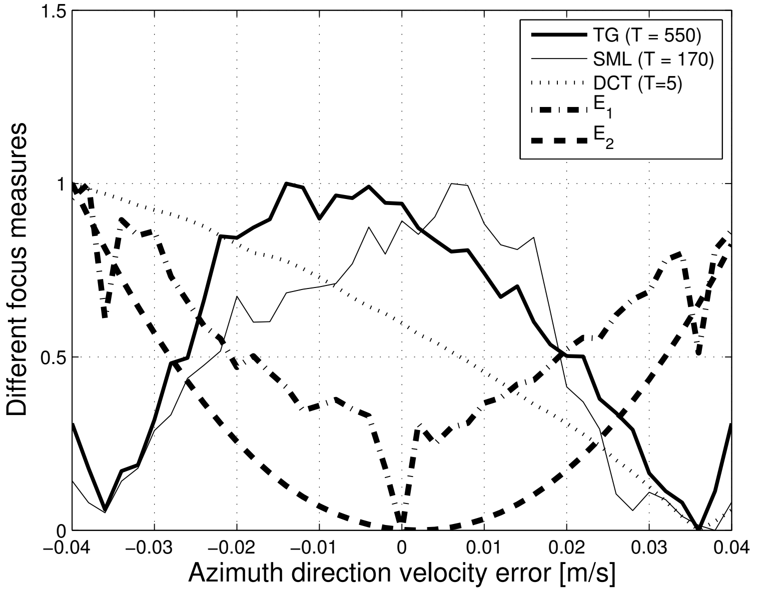

(b) *Focus measures with no acceleration error.*

Figure 4.12: *Focus measures for the structured scene with only error in* a_0^Y *and* v_0^X*.*

use as a focus measure in the minimisation criterion.

The focus measures above are evaluated on images that have no noise, *i.e.* the images are perfect. In reality, that is not the case, and images contain some noise caused by the noise in the radar measurements. Therefore, the same two scenes are used again, but white Gaussian noise with variance $\sigma^2 = 1.5$ is added to the radar echos. The images obtained with this setup are depicted in Figure 4.14a and Figure 4.15a. The focus measures for these two images are shown in Figure 4.14 and Figure 4.15. It can be seen in these plots that entropy 2 measure still behaves good, it is smooth and convex in the vicinity of the true values of the navigation states. The only thing that happens with entropy 2 is that the value of the function is different, but the principal form is the same as for the noise free case.

Another thing that can be noticed from these plots is that the entropy 1 measure does not have a pronounced global minimum in the case of structured scene, as it has for the noise free case. It looks similar to the case with unstructured scene. This is not surprising since the unstructured scene will behave like the image noise for the focus measure. It also looks like TG measure behaves better for the noisy case, at least around the true values of the navigation states. The explanation might be that TG measure has a threshold that can filter out the noise.

The conclusion from the evaluation above is that entropy 2 measure works quite fine for both cases, with and without noise in the radar measurements, and it is the smoothest measure of all tested ones. Entropy 1 could be used as well, at least for the scenes with structure, while TG seems to work for the case with the noise in images. The drawback of the TG measure is the threshold that must be tuned to the different imaged scenes.

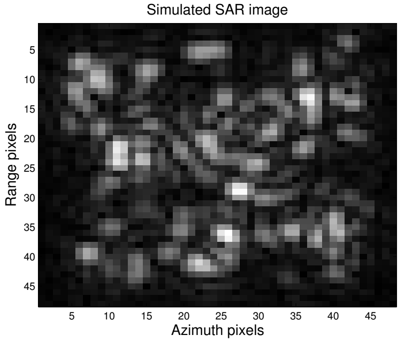

(a) SAR image of the unstructured scene.

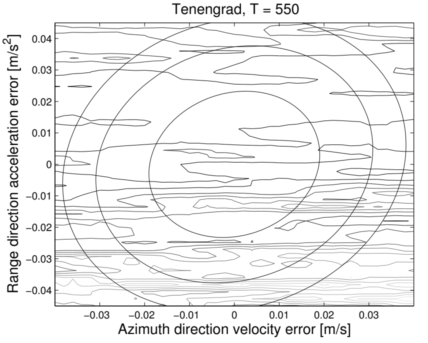

(b) TG focus measure with $T = 550$.

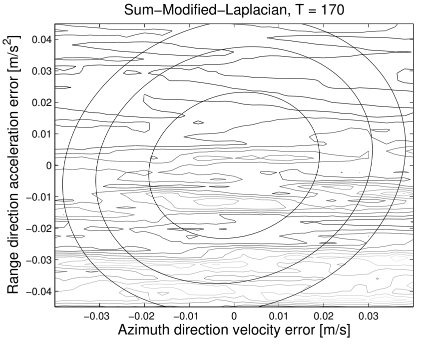

(c) SML focus measure with $T = 170$.

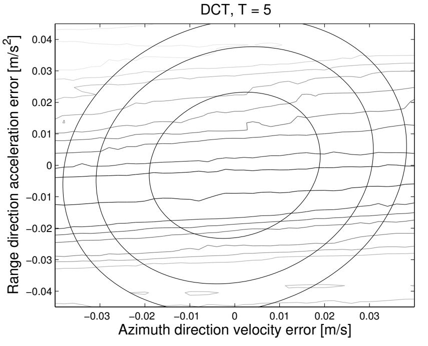

(d) DCT focus measure with $T = 5$.

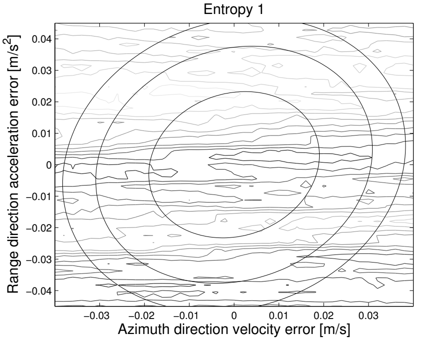

(e) Entropy 1 focus measure.

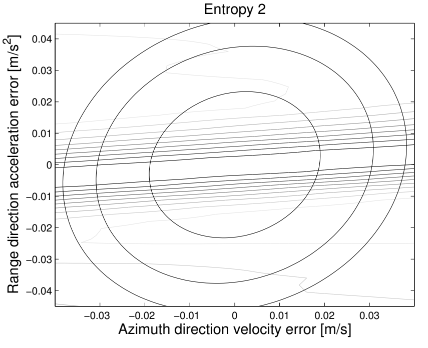

(f) Entropy 2 focus measure.

Figure 4.13: *Focus measures for the image with more informative unstructured scene.*

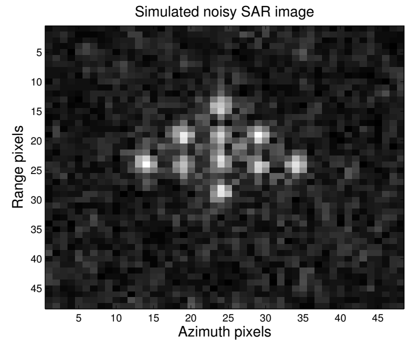

***(a)** Noisy SAR image of the structured scene.*

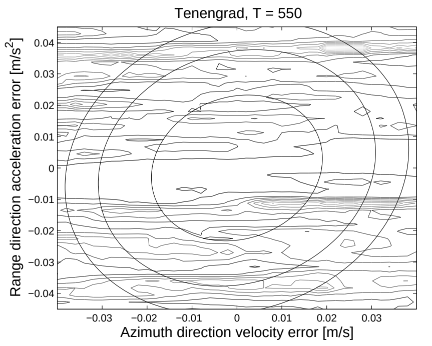

***(b)** TG focus measure with $T = 550$.*

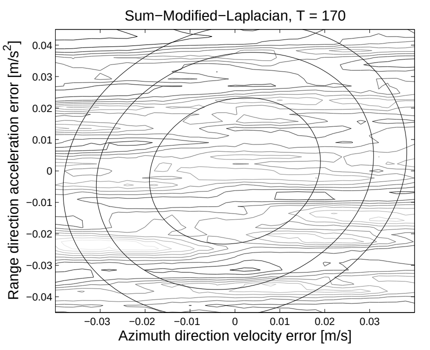

***(c)** SML focus measure with $T = 170$.*

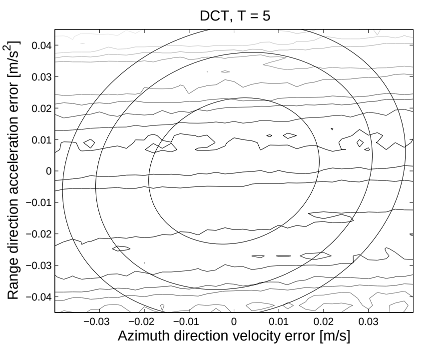

***(d)** DCT focus measure with $T = 5$.*

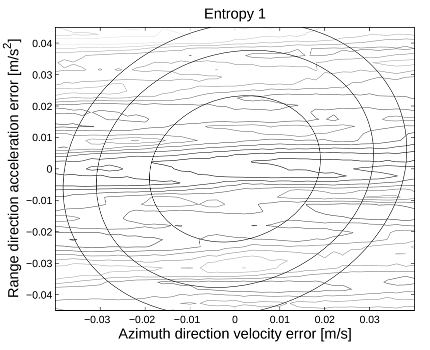

***(e)** Entropy 1 focus measure.*

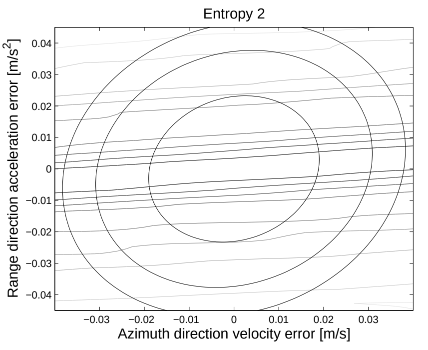

***(f)** Entropy 2 focus measure.*

***Figure 4.14:** Focus measures for the noisy image with more informative structured scene. White Gaussian noise with variance $\sigma^2 = 1.5$ is added on the radar echoes.*

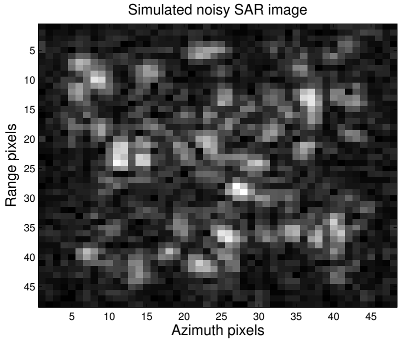

(a) *Noisy SAR image of the unstructured scene.*

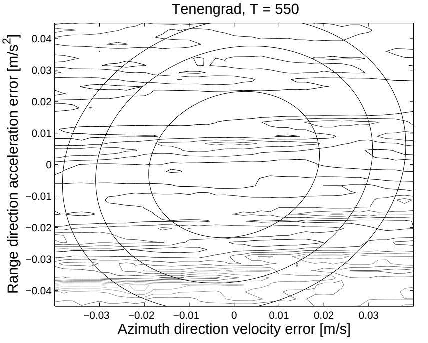

(b) *TG focus measure with $T = 550$.*

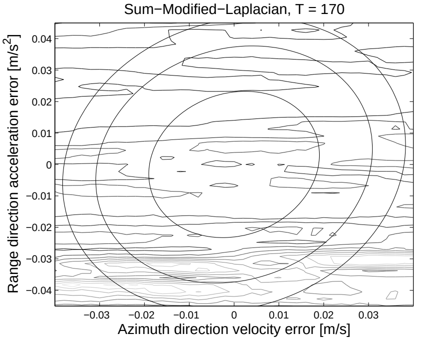

(c) *SML focus measure with $T = 170$.*

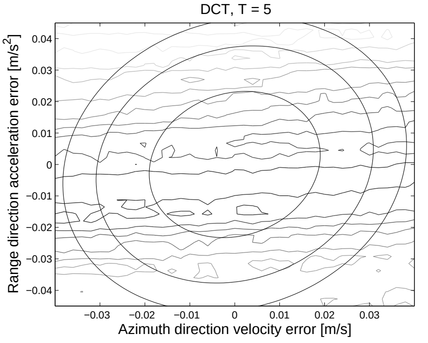

(d) *DCT focus measure with $T = 5$.*

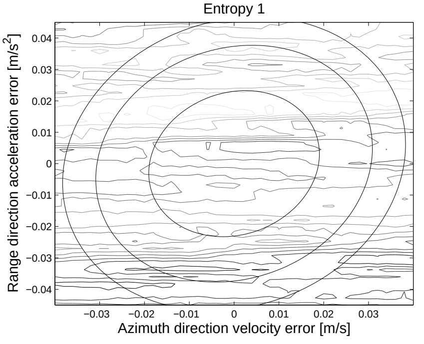

(e) *Entropy 1 focus measure.*

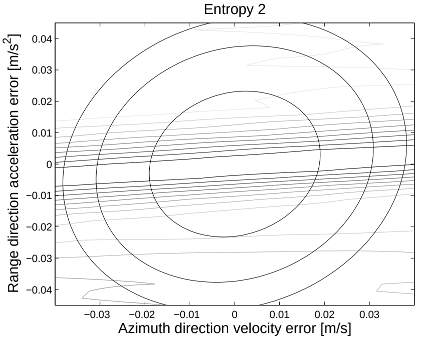

(f) *Entropy 2 focus measure.*

Figure 4.15: *Focus measures for the noisy image with more informative unstructured scene. White Gaussian noise with variance $\sigma^2 = 1.5$ is added on the radar echoes.*

5

Methods Based on the Complete SAR Images

As demonstrated in Section 4.3.3, all measures, except maybe DCT, can be used as a measure of the image focus, and used in (3.12a). If common minimisation methods are used, as for example gradient based methods, numerical gradients must be calculated for most of the focus measures. Since most of the functions are non-convex, gradient based methods may be inefficient and the global search method must be used there in order to find the global minimum. One exception from these obstacles is the entropy 2 measure. For that measure, the gradient can be calculated, at least semi-analytically and it is convex in the vicinity of the correct values, except for the ridge. A local method can be used here, for example some quasi-Newton method, in order to get near the global minimum and then some other measure with sharper global minimum can be used [Sjanic and Gustafsson, 2010]. However, since in general the focus measure function is also a function of the scene that is imaged, it is not certain that the global minimum will be pronounced, as is the case with image in Figure 4.13a.

In this section both quasi-Newton search and global grid based search methods will be demonstrated on some different examples of scenarios and the performance will be evaluated.

5.1 Gradient Based Search

Gradient search methods will be exemplified here with a couple of examples with different trajectories and errors in them. As mentioned above, the entropy 2 measure can be used as a first step to get near the global minimum, since it is convex but very flat in the proximity of the global minimum, and then some other measure can be used to find the global minimum, for example entropy 1 due to its sharp minimum for the correct values or Tenengrad if noisy images are considered. In the previous chapter only two states and their initial values are considered, v_0^X and a_0^Y, in order to be able to depict the focus measures. In general the minimisation should be applied for these states for all or at least some of the time instants along trajectory. Such an example will be studied later in this chapter.

A gradient search can, for the general problem $\min_x f(x)$, be formulated as

$$x^{k+1} = x^k + \mu_k H(x^k)^{-1} \nabla f(x^k) \tag{5.1a}$$

$$\nabla f(x) = \frac{\partial}{\partial x} f(x) \tag{5.1b}$$

where μ_k is step size with $\mu_0 = 1$, $f(x)$ is the loss function as in (3.12a) and $H(x)$ is some (positive definite) matrix. The initial estimate, x^0, can be taken as the usual estimate from the navigation system. In the simplest case H can be chosen as the identity matrix and the procedure becomes a pure gradient search. The disadvantage of such procedure is the slow convergence, especially if the function to be minimised is ridge-like. If H is chosen as the Hessian of f, the procedure becomes a Newton search. The Newton search has a fast convergence, it is constructed for one-step convergence for quadratic functions, and is to prefer if the Hessian is available. In many cases the Hessian is either not available or very difficult to obtain, as in the case considered here, and some approximate methods must be applied. One option is to calculate it as

$$H(x) = \nabla f(x) \cdot (\nabla f(x))^T + \lambda I \tag{5.2}$$

where λ is chosen as a small number, usually $\sim 10^{-6}$, to avoid singularity. This procedure resembles of Levenberg-Marquardt procedure for least squares. Another approach is a quasi-Newton search, and BFGS in particular, where the Hessian is approximated by utilising gradients of the function during the search, see Nocedal and Wright [2006]. The general gradient search procedure is summarised in Algorithm 1.

In all these procedures it is essential to obtain the gradient of the loss function. Because of the special structure of the focus measure function and the SAR processing algorithm, the complete analytical gradient is hard to obtain. For example, for the Entropy 1 measure it is hard to differentiate a histogram of the image. In this case numerical methods must be used. However, for the Entropy 2 measure it is almost possible to obtain analytical gradient and this will be described in the next subsection.

5.1.1 Calculating the Gradient

Here the calculations to obtain an analytical gradient of the entropy 2 function will be presented. The key to doing this is simply the chain rule for gradient calculation, *i.e.* if we, for example, have a function $f(x(t))$ and want to obtain $\nabla_t f$, the chain rule states that

$$\nabla_t f = \frac{\partial f}{\partial x} \frac{\partial x}{\partial t} \tag{5.3}$$

Algorithm 1 Gradient search procedure

Input: Initial iterate of the optimisation parameters x^0, raw radar data, tolerance thresholds ε_1, ε_2, ε_3
Output: Solution $\hat{x}$, focused SAR image

$k := 0$
repeat
  Calculate gradient of the cost function, $\nabla f(x^k)$
  Calculate (approximate) Hessian, $H(x^k)$
  $\mu_k := 1$
  repeat
    $x^{k+1} := x^k + \mu_k H(x^k)^{-1} \nabla f(x^k)$
    $\mu_k := \mu_k/2$
  until $f(x^{k+1}) < f(x^k)$
  $k := k+1$
until $\|x^k - x^{k-1}\|^2 < \varepsilon_1$ **or** $\nabla f(x^{k-1}) < \varepsilon_2$ **or** $\|f(x^k) - f(x^{k-1})\|^2 < \varepsilon_3$

In order to apply the chain rule, first the decomposition chain of the entropy 2 focus measure will be done and then, all partial derivatives will be presented.

The first function to be differentiated is Entropy 2 focus measure

$$F = -\sum_{i=1}^{M}\sum_{j=1}^{M} p_{ij} \ln p_{ij} = -\sum_{i=1}^{M^2} p_i \ln p_i \tag{5.4}$$

where last equality is simply reformulation of the double sum by vectorising the image. Next, each p_i is obtained by

$$p_i = \frac{|\tilde{I}_i|^2}{\sum_j |\tilde{I}_j|^2} \tag{5.5}$$

meaning that p_i is a function of the absolute value of the complex-valued SAR image. In the next step, we need to obtain derivative $\partial|\tilde{I}|/\partial R$. In the creation of the image, a back-projection sum is evaluated and all partial images are summed. Each partial image is a function of one column in the RAR image and the range from the platform to each pixel in the SAR image, see Section 2.2. Unfortunately it is not easy, if not impossible, to obtain analytical expression for this derivative, $\partial|\tilde{I}|/\partial R$. However, this value can simply be obtained during image creation by means of numerical derivation. The cost for that procedure is memory demand and execution time which both are doubled. But this increase in cost is constant no matter how many parameters optimisation is performed over. If compared to calculating numerical gradients, the cost for that is increasing linearly with the number of parameters.

Last function that needs to be calculated is the range as a function of the states, $R(x_t)$. To calculate the analytical expression of this function some SAR geometry

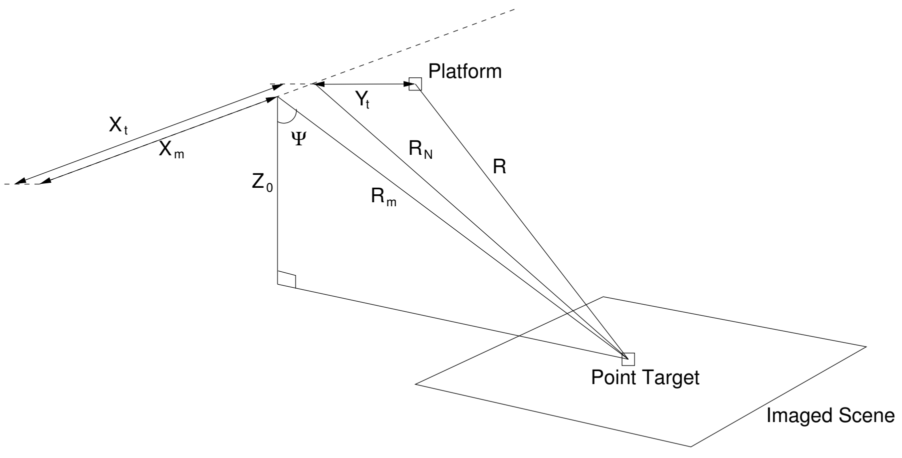

Figure 5.1: *SAR geometry. The figure is not to scale.*

preliminaries are needed. In order to express range as a function of the states, the geometry setup as in Figure 5.1 can be considered. From the figure it can be seen that the range R_t can, with help from cosine theorem, be expressed as

$$R_t = \sqrt{R_N^2 + Y_t^2 - 2\cos\left(\frac{\pi}{2} - \Psi\right) R_N Y_t} \tag{5.6a}$$

$$R_N = \sqrt{R_m^2 + (X_m - X_t)^2} \tag{5.6b}$$

i.e. as a function of the trajectory. Here the exact expression for the range along the trajectory is used, unlike in most of the SAR literature, where approximate and linearised expressions are used, see for example Xing et al. [2009]. This is due to the fact that in low frequency SAR application, as the one considered here, the ratio between range and trajectory length is not negligible due to the lobe width. If approximate expressions are used, too large errors will be introduced in the beginning and the end of the trajectory.

Next, the dynamical model (3.24a) can be used to express the position states used in the range expression above as a function of any other state by using that

$$x_t = F^{t-k} x_k, \quad t > k \tag{5.7}$$

Note that the noise term is neglected since it is equivalent to optimise over noise and over acceleration states, so the latter one is used here to simplify the expressions. This gives that positions can be expressed as

$$X_t = X_0 + T_s(t-k)v_k^X + \frac{T_s^2(t-k)^2}{2} a_k^X \tag{5.8a}$$

$$Y_t = Y_0 + T_s(t-k)v_k^Y + \frac{T_s^2(t-k)^2}{2} a_k^Y \tag{5.8b}$$

If these expressions are used in the (5.6a), we can easily obtain partial derivatives of the range with respect to the velocities and accelerations in arbitrary time points. Now we have everything needed to calculate the gradient of the focus measure with respect to the trajectory states. The decomposition of the gradient is

$$\frac{\partial F}{\partial x} = \frac{\partial F}{\partial p} \frac{\partial p}{\partial |\tilde{I}|} \frac{\partial |\tilde{I}|}{\partial R} \frac{\partial R}{\partial x} \tag{5.9}$$

and the partial derivatives are, in turn (with $\cos(\pi/2 - \Psi) = \sin(\Psi)$)

$$\frac{\partial F}{\partial p_i} = -\ln p_i - 1 \tag{5.10a}$$

$$\frac{\partial p_i}{\partial |\tilde{I}_j|} = \begin{cases} \frac{2|\tilde{I}_j| \sum |\tilde{I}|^2 - 2|\tilde{I}_j|^2 |\tilde{I}_i|}{\left(\sum |\tilde{I}|^2\right)^2}, & i = j \\ -\frac{2|\tilde{I}_j|^2 |\tilde{I}_i|}{\left(\sum |\tilde{I}|^2\right)^2}, & i \neq j \end{cases} \tag{5.10b}$$

$$\frac{\partial R_t}{\partial v_k^X} = -\frac{(X_m - X_t)T_s(t-k) - \frac{\sin(\Psi)(X_m - X_t)Y_t T_s(t-k)}{R_N}}{R_t} \tag{5.10c}$$

$$\frac{\partial R_t}{\partial v_k^Y} = \frac{Y_t T_s(t-k) - \sin(\Psi) R_N T_s(t-k)}{R_t} \tag{5.10d}$$

$$\frac{\partial R_t}{\partial a_k^X} = -\frac{(X_m - X_t)T_s^2(t-k)^2 - \frac{\sin(\Psi)(X_m - X_t)Y_t T_s^2(t-k)^2}{R_N}}{2R_t} \tag{5.10e}$$

$$\frac{\partial R_t}{\partial a_k^Y} = \frac{Y_t T_s^2(t-k)^2 - \sin(\Psi) R_N T_s^2(t-k)^2}{2R_t} \tag{5.10f}$$

and $\partial|\tilde{I}|/\partial R$ is numerically calculated during image formation. Now, at least for entropy 2 focus measure, we can calculate the gradient (semi-) analytically and use it in the minimisation procedure. The second term in (3.12a) is easy to differentiate, since it is a quadratic form and $h(x)$ is a linear function in this case.

5.1.2 Numerical Examples

In order to demonstrate the behaviour of the gradient search for this setup, the SAR image from Figure 4.11a is used. In order to illustrate the behaviour, only two optimisation variables are considered here, $x^0 = [v_0^X,\ a_0^Y]^T$ and the algorithm is initiated with different starting points x^0 based on the stationary covariance of the states in the system. Those values are $[100.005,\ 0.005]^T$, $[99.99,\ 0.01]^T$, $[99.995,\ 0.02]^T$, $[100.02,\ -0.01]^T$ and $[100.005,\ -0.035]^T$. In Figure 5.2a, the gradient search based entropy 2 measure is illustrated and we can see that solutions converge to the flat ridge-like area close to the correct acceleration, but not necessarily to the correct velocity. In Figure 5.2b, the gradient search where the entropy 1 measure is used is depicted. In this case the algorithm is initiated with the solution from the entropy 2 search. It can be seen that this minimisation strategy works pretty well, although one solution is stuck in a local minimum. In that case the velocity error is the largest one of all errors. Note also that only the focus measure is used to find estimate of the states *i.e.* γ_s is set to zero while γ_F is set to one in Equation 3.12a.

It is interesting to see how the image created with the solution that is stuck in the local minimum of the entropy 1 measure looks like compared to the unfocused image that is started with. As illustrated in Figure 5.3, it can be seen that the image created with values from the minimisation procedure is very close to the focused image and much better than the unfocused images that are started with. The probable explanation for this comes from the fact that small azimuth direction velocity errors do not influence the final image much due to the quantisation effects. However the estimate of the navigation states is not correct.

In the second example a more realistic setup is done. The optimisation problem to be solved is

$$\min_{v_0^X, a_0^Y, w^Y_{\lfloor N/4 \rfloor}, w^Y_{\lfloor N/2 \rfloor},\ w^Y_{\lfloor 3N/4 \rfloor}} \quad 0.99 E_{1,2}(x_{0:N}) + 0.01 \left(\sum_{t=1}^{N} \|a_t^{mY} - a_t^Y\|^2_{R_t} + \|w_t^Y\|^2_{Q_t^Y} \right) \tag{5.11a}$$

subject to

$$x_{t+1} = F x_t + G w_t \tag{5.11b}$$

$$\begin{bmatrix} X_0 \\ Y_0 \\ v_0^Y \\ a_0^X \end{bmatrix} = \begin{bmatrix} 0 \\ 0 \\ 0 \\ 0 \end{bmatrix} \tag{5.11c}$$

$$w_t^X = 0,\ t \in \left\{0 : N\right\} \tag{5.11d}$$

$$w_t^Y = 0,\ t \notin \left\{\lfloor N/4 \rfloor,\ \lfloor N/2 \rfloor,\ \lfloor 3N/4 \rfloor\right\} \tag{5.11e}$$

$$Q_t^Y = \begin{cases} \infty, & t \in \left\{\lfloor N/4 \rfloor,\ \lfloor N/2 \rfloor,\ \lfloor 3N/4 \rfloor\right\} \\ 0, & \text{otherwise} \end{cases} \tag{5.11f}$$

$$P_0 = \infty \cdot I_2 \tag{5.11g}$$

where model (3.24) is used and a^m is the measured acceleration with additive white Gaussian noise with $R_t = 0.0022\ \mathrm{m}^2/\mathrm{s}^4$. $E_{1,2}(x_{0:N})$ is either entropy 2 or entropy 1, exactly as in the previous example. It is assumed that a disturbance on Y-direction acceleration will act on the platform in an impulse like manner only a few times during the SAR image generation and that the amplitude of the disturbance is set free. This is the meaning of equation (5.11f). It is also assumed that the acceleration in X-direction will vary slowly due to the platforms inherited inertia in this direction, so it can be assumed to be zero. Both scenes from Figure 4.11a and Figure 4.13a are used and 30 Monte Carlo simulations are performed in order to evaluate the performance of the estimation procedure.

Resulting RMSE of the parameters and the mean value of the error image power is presented in the Table 5.1 and Table 5.2 for both structured and unstructured scene. Here the actual acceleration is presented instead of the process noise value,

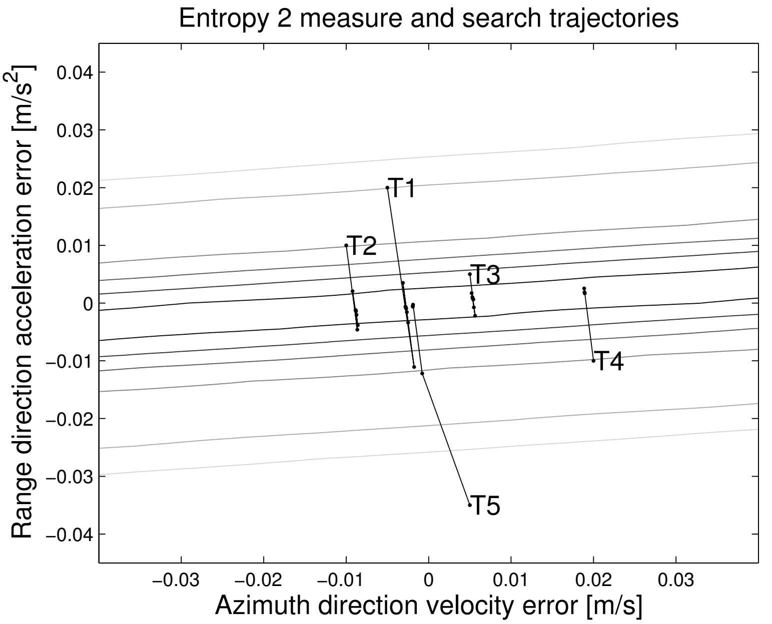

***(a)** Search trajectory for five different values of x^0 using entropy 2 focus measure.*

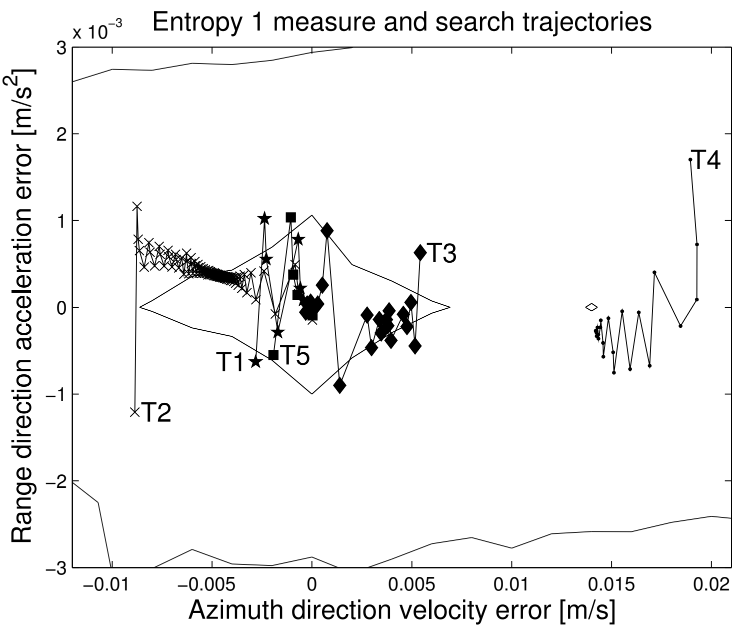

***(b)** Search trajectory for entropy 1 focus measure with x^0 given by the entropy 2 gradient search.*

***Figure 5.2:** Search trajectory for five different values of x^0 using two different entropy measures.*

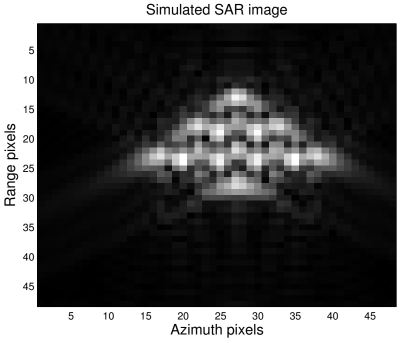

(a) *Image created with error in velocity of 0.02 m/s and in acceleration of* $-0.01\ m/s^2$.

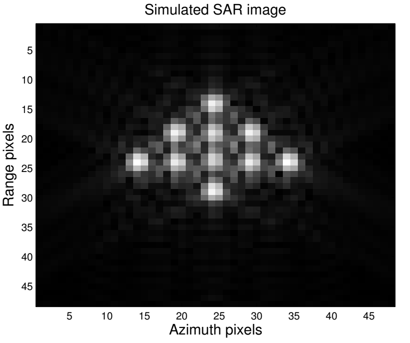

(b) *Image created with error in velocity of 0.014 m/s and in acceleration of* $-0.0003\ m/s^2$.

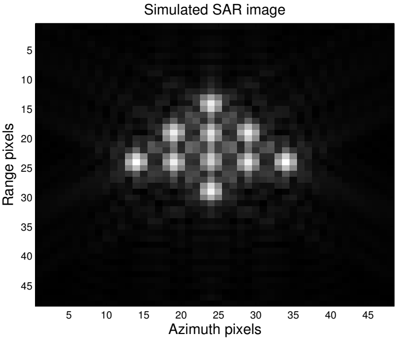

(c) *Focused image as a reference.*

Figure 5.3: *Resulting images from the minimisation procedure with starting point* $[100.02,\ -0.01]^T$.

Parameter	RMSE (opt. with E_2)	RMSE (opt. with E_1)
$\hat{v}_0^X$	$7.05 \cdot 10^{-3}$ m/s	$7.04 \cdot 10^{-3}$ m/s
$\hat{a}_0^Y$	$9.94 \cdot 10^{-4}$ m/s^2	$9.15 \cdot 10^{-4}$ m/s^2
$\hat{a}_{\lfloor N/4 \rfloor}^Y$	$6.51 \cdot 10^{-4}$ m/s^2	$6.34 \cdot 10^{-4}$ m/s^2
$\hat{a}_{\lfloor N/2 \rfloor}^Y$	$6.89 \cdot 10^{-4}$ m/s^2	$6.84 \cdot 10^{-4}$ m/s^2
$\hat{a}_{\lfloor 3N/4 \rfloor}^Y$	$6.02 \cdot 10^{-4}$ m/s^2	$6.03 \cdot 10^{-4}$ m/s^2
Mean value of the error image power	149.6	126.9

Table 5.1: *RMSE for the estimated parameters and the mean value for the error image power for the structured scene.*

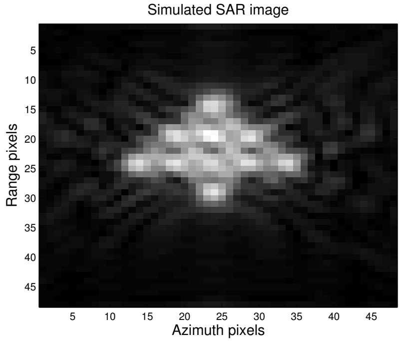

*(**a**) SAR image of the structured scene created with noisy position data.*

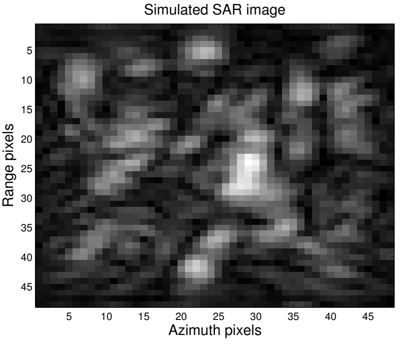

*(**b**) SAR image of the unstructured scene created with noisy position data.*

Figure 5.4: *SAR images created with noisy position data.*

Parameter	RMSE (opt. with E_2)	RMSE (opt. with E_1)
$\hat{v}_0^X$	$11.2 \cdot 10^{-3}$ m/s	$11.2 \cdot 10^{-3}$ m/s
$\hat{a}_0^Y$	$11.61 \cdot 10^{-4}$ m/s^2	$10.98 \cdot 10^{-4}$ m/s^2
$\hat{a}_{\lfloor N/4 \rfloor}^Y$	$6.63 \cdot 10^{-4}$ m/s^2	$6.52 \cdot 10^{-4}$ m/s^2
$\hat{a}_{\lfloor N/2 \rfloor}^Y$	$9.31 \cdot 10^{-4}$ m/s^2	$8.86 \cdot 10^{-4}$ m/s^2
$\hat{a}_{\lfloor 3N/4 \rfloor}^Y$	$7.77 \cdot 10^{-4}$ m/s^2	$7.58 \cdot 10^{-4}$ m/s^2
Mean value of the error image power	1348	1242

Table 5.2: *RMSE for the estimated parameters and the mean value for the error image power for the unstructured scene.*

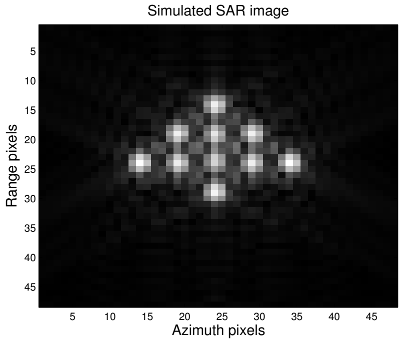

(a) *Image of the structured scene after minimisation with Entropy 2 as focus measure.*

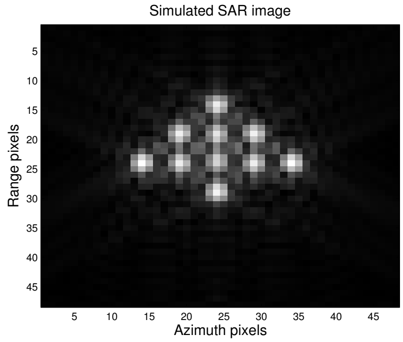

(b) *Image of the structured scene after minimisation with Entropy 1 as focus measure.*

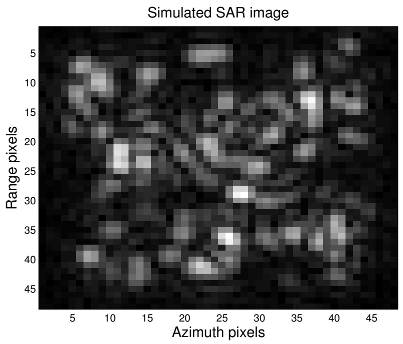

(c) *Image of the unstructured scene after minimisation with Entropy 2 as focus measure.*

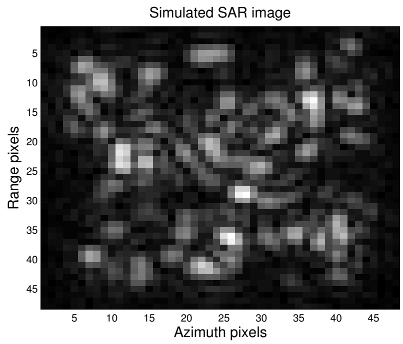

(d) *Image of the unstructured scene after minimisation with Entropy 1 as focus measure.*

Figure 5.5: *Resulting images from the gradient search minimisation.*

since it is more interesting. It can be noticed that the improvement of the RMSE after further minimisation with entropy 1 is not very big, it is in the magnitude of 10^{-5}. It suggests that the extra step of minimisation with entropy 1 can be skipped if faster procedure is sought.

In Figure 5.4 a noisy position (one of the 30 noise realisations) is used for the image generation. We see that both images are unfocused and the image of the unstructured scene is pretty bad, all the dominant targets are blurred. In Figure 5.5 the images after minimisation with entropy 2 and 1 are depicted (for the same noise realisation as above). Here it can be seen that improvement in the image with extra minimisation with entropy 1 is impossible to see with the naked eye, *i.e.* the improvement of the navigation states does not visibly improve the images. This could be expected from the results from MC simulations.

The resulting estimates of the parameters and error image power after entropy 1 minimisation for the two scenes and this particular realisation of the noise are presented in the Table 5.3.

Parameter	Structured scene	Unstructured scene
$\hat{v}_0^X$	$9.236 \cdot 10^{-3}$ m/s	$10.13 \cdot 10^{-3}$ m/s
$\hat{a}_0^Y$	$-3.057 \cdot 10^{-4}$ m/s^2	$-1.707 \cdot 10^{-4}$ m/s^2
$\hat{a}_{\lfloor N/4 \rfloor}^Y$	$-0.553 \cdot 10^{-4}$ m/s^2	$-1.733 \cdot 10^{-4}$ m/s^2
$\hat{a}_{\lfloor N/2 \rfloor}^Y$	$11.15 \cdot 10^{-4}$ m/s^2	$10.25 \cdot 10^{-4}$ m/s^2
$\hat{a}_{\lfloor 3N/4 \rfloor}^Y$	$1.384 \cdot 10^{-4}$ m/s^2	$1.234 \cdot 10^{-4}$ m/s^2
Error image power	51.37	53.12

Table 5.3: *Error in the estimated parameters for the two scenes after entropy 1 minimisation procedure.*

5.2 Global Grid Search

As demonstrated in Section 5.1, the gradient based search method is able to estimate the navigation states that produce fairly good SAR images. This method is still prone to the local minima problem due to the non-convexity of the focus measures, especially if initial values of the optimisation parameters are far away from the solution. A solution to that problem is a global search method. The most straightforward approach is to use a grid search and find the minimum of the loss function, (3.12a) in the grid. This approach can be described according to Algorithm 2. The function $\mathbf{dim}(x)$ returns the amount of elements in x. The

Algorithm 2 Grid search procedure

Input: Initial value of the optimisation parameters x^0, raw radar data, grid size for each parameter S_i, amount of grid points for each parameter N_i
Output: Solution $\hat{x}$, focused SAR image

Create grid $G(x_i, j_i)$ of the parameter values centred on x^0 with N_i grid points and with grid resolution $\Delta_i = S_i/N_i$,
$i = 1, \ldots, \mathbf{dim}(x)$, $j_i = x_i^0 - S_i/2, x_i^0 - S_i + \Delta_i, \ldots, x_i^0 + S_i/2$

for all i **in** 1 **to** $\mathbf{dim}(x)$ **do**
  for all j_i **in** $x_i^0 - S_i/2$ **to** $x_i^0 + S_i/2$ **step** Δ_i **do**
    $V(G(x_i, j_i))$:= value of the loss function (3.12a) for parameter x_i evaluated in grid point j_i
  end for
end for
$\hat{x} := \arg\min_x V$

performance of such method is dependent of the grid size and its resolution. The better performance is achieved with the larger grid (suitable size could be *e.g.* 2σ standard deviation of the parameters) and that has a fine grid resolution. These choices directly influence the amount of executions of the SAR image creation algorithm, which is

$$\prod_{i=1}^{\mathbf{dim}(x)} N_i, \tag{5.12}$$

$$\begin{aligned} N_i &= \text{amount of grid points for parameter } i, \\ i &= 1, \ldots, \mathbf{dim}(x). \end{aligned}$$

This means that the higher performance requires more execution time and slower algorithm, *i.e.* there is a fundamental balance between performance and speed. This kind of algorithm can be implemented in an iterative manner where the grid size and resolution is changed between iterations, since it is assumed that each iteration makes the estimate better. In this case, a coarser and larger grid can be used in the first iteration, and finer and smaller grid in the successive iterations. The total amount of executions of the SAR algorithm is, in this case

$$\sum_{j=1}^{M} \prod_{i=1}^{\mathbf{dim}(x)} N_{ij}, \tag{5.13}$$

$$\begin{aligned} N_{ij} &= \text{amount of grid points for parameter } i \text{ in iteration } j, \\ M &= \text{amount of iterations}, \\ j &= 1, \ldots, M, \\ i &= 1, \ldots, \mathbf{dim}(x). \end{aligned}$$

The iterative approach can be beneficial if the amount of optimisation parameters is large and the accuracy demand is high, *i.e.* the grid resolution should be fine.

5.2.1 Numerical Examples

The performance of the global grid search will be evaluated on the test SAR images as in Section 5.1.2. The same optimisation cases, with both two and five optimisation parameters, are evaluated for the structured scene only. the focus measure that is used is entropy 1 due to its pronounced minimum value for the correct parameters for the structured scene. If noisy SAR images are used, TG could have been used as well, as noticed in Chapter 4. Because the grid search is a time consuming procedure and its result is only used as a comparison to the gradient search method, no Monte Carlo simulations are done and only the structured scene is used.

The error in the estimated parameters and error image power using the grid search procedure is presented in Table 5.4 and the resulting SAR images are depicted in Figure 5.6. It can be seen that the estimate of the parameters in both cases is very close to the true parameters. The only source of the inaccuracy in

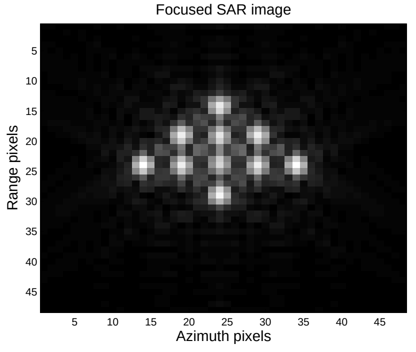

(a) Focused SAR image generated with estimated trajectory with two optimisation parameters.

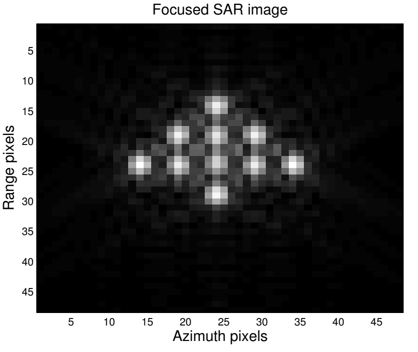

(b) Focused SAR image generated with estimated trajectory with five optimisation parameters.

Figure 5.6: *SAR image generated with estimated trajectories with two and five optimisation parameters respectively.*

Parameter	Two parameter case	Five parameter case
$\hat{v}_0^X$	$5 \cdot 10^{-3}$ m/s	-$3 \cdot 10^{-3}$ m/s
$\hat{a}_0^Y$	$2 \cdot 10^{-4}$ m/s^2	-$5 \cdot 10^{-4}$ m/s^2
$\hat{a}_{\lfloor N/4 \rfloor}^Y$	-	-$5 \cdot 10^{-4}$ m/s^2
$\hat{a}_{\lfloor N/2 \rfloor}^Y$	-	-$5 \cdot 10^{-4}$ m/s^2
$\hat{a}_{\lfloor 3N/4 \rfloor}^Y$	-	-$5 \cdot 10^{-4}$ m/s^2
Error image power	2.60	70.25

Table 5.4: *Error in the estimated parameters for the structured scene with the grid search minimisation procedure.*

this case is the combination of the initial parameter vector x^0 and the grid resolution, which causes the grid points not to coincide with the true parameter values.

6

Methods Based on Raw Radar Data

In this chapter methods based on raw radar data, or RAR, are used to acquire information about the platform's motion and in that way obtain better trajectory in the filtering framework.

6.1 Introduction to Phase Gradient or Range Gradient Methods

In the previous sections the common factor for the auto-focusing procedure is that SAR images, either real or complex, are used to obtain a focus measure as a function of the platform trajectory. Since essentially the same information is contained in the raw SAR measurements, these can be used for the same goal, *i.e.* auto-focus and extracting the platform's trajectory. Since raw SAR data contains phase delay information (which is discarded during image formation), it is that information that is mainly used for auto-focusing. These methods are called Phase Gradient (PG) or Phase Difference (PD) methods, see for example Oliver and Quegan [2004], Xing et al. [2009], Wahl et al. [1994], Yegulalp [1999] or Fienup [1989] for details.

The basis for this approach is the fact that the phase delay of the radar echo data is proportional to the range which will vary hyperbolically as a function of time, see (5.6) and Figure 5.1,

$$\varphi_t = -\frac{4\pi}{\lambda} R_t \tag{6.1}$$

where λ is the wavelength of the radar carrier. It is seen that phase delay and range are proportionally related to each other. That means that phase and range can be used equivalently, it is only the factor $-4\pi/\lambda$ that differs. Here, exactly as in previous sections the platform's altitude is assumed constant but the model is easily adapted to the case when altitude is varying. We can now calculate the time derivative of the phase delay and obtain

$$\dot{\varphi}_t = -\frac{4\pi}{\lambda}\dot{R}_t \tag{6.2}$$

The range derivative, $\dot{R}_t$, can be calculated by taking the time derivative of the range from (5.6) (repeated here for convenience)

$$R_t = \sqrt{R_N^2 + Y_t^2 - 2\sin(\Psi)\, R_N\, Y_t} \tag{6.3a}$$

$$R_N = \sqrt{R_m^2 + (X_m - X_t)^2} \tag{6.3b}$$

By using the chain rule we obtain

$$\dot{R}_t = \frac{-(X_m - X_t)v_t^X + Y_t v_t^Y - R_N \sin(\Psi) v_t^Y + \frac{Y_t \sin(\Psi)(X_m - X_t)v_t^X}{R_N}}{\sqrt{R_N^2 + Y_t^2 - 2R_N Y_t \sin(\Psi)}} \tag{6.4}$$

As mentioned in Chapter 2, in the SAR applications where radar frequency is high or antenna size is large, the lobe is narrow and an approximate expression for the range and its gradient can be used without much loss of accuracy. The source of the approximation in this case is the fact that the synthetic aperture length, $2X_m$, and deviation Y_t are much shorter than the range to the middle of the scene, R_m. The range can then be approximated with the Taylor expansion as

$$R_t \approx R_m + \frac{(X_m - X_t)^2}{2R_m} \tag{6.5}$$

and the range gradient calculated with this approximate expression and under the assumptions that velocity v_t^X is constant (reasonable assumption for short aperture times) is a linear (affine) function of time

$$\dot{R}_t \approx -\frac{(X_m - X_t)v^X}{R_m} = -\frac{(X_m - v^X t)v^X}{R_m} = -\frac{X_m v^X}{R_m} + \frac{(v^X)^2}{R_m}t \tag{6.6}$$

The PG methods try to estimate the slope of this linear function from the raw data in order to compensate for the phase delay error caused by the platform's unknown motion. This compensation is then applied during azimuth compression in order to focus the image. For the time domain image formation approach, this is equivalent to estimating the unknown motion. The assumption made above about narrow radar lobe is not applicable to the SAR systems which operates with low frequency. This will imply that range gradient cannot be approximated with the linear function except in the narrow band around zero phase delay. Due to this, the method of fitting a linear function in order to compensate for the phase delay error described above will not work satisfactory for the low frequency SAR. That is why, just as in the previous sections, the exact expression for the range is used here.

If we look at the equation (6.4) we see that the right hand side consists of states of the dynamical model, *i.e.* positions, velocities and some (known) constants. The left hand side of the equation is the entity that can be estimated from the SAR data (either raw or partially processed). This implies that we have a measurement equation from the standard sensor fusion and filtering framework in the form

$$y_t = h(x_t; \theta) + e_t \tag{6.7a}$$

$$x_t = [X_t \; Y_t \; v_t^X \; v_t^Y]^T \tag{6.7b}$$

$$\theta = [R_m \; X_m \; \Psi]^T \tag{6.7c}$$

and some standard filtering methods, such as the EKF or the particle filter, can be applied.

6.2 Estimating the Range Gradient

In order to create measurements from (6.7), we need an estimate of the phase delay. Phase delay estimation kernel, proposed in Fienup [1989], is (superindex m stands for measured)

$$\dot{\varphi}_t^m = \frac{1}{T} \arg \left\{ \sum_R I_{\mathrm{RAR}}(R, t) I^*_{\mathrm{RAR}}(R, t-T) \right\} \tag{6.8}$$

where $I_{\mathrm{RAR}}(R, t)$ is the complex RAR image from (2.1), *i.e.* raw radar data, I^* denotes the complex conjugate, R is the range dimension and t is the azimuth (or time) dimension and T is the time between pulses which is the inverse of the pulse repetition frequency. This estimate can be calculated in a sequential manner, pulse by pulse and be interpreted as a measurement y_t for each time instance and used in the filtering framework. The problem with both of these methods is that they are developed for the high frequency SAR systems where phase gradient can be approximated with a linear function. Since this is not the case in the low frequency SAR system some other method must be applied. If seen in the context of back-projection and subimage processing described in Chapter 2, if each radar echo is used to generate a subimage, the complete SAR image is then simply the sum of all subimages. Each subimage is created with some assumption about range from the platform to the scene, either correct or perturbed, and the raw data contain information about the correct range. This in turn means that each (complex valued) pixel in the back-projected subimage will contain the information about the range between the platform and the scene. However, due to the phase wrapping effect in the complex number arithmetic, the absolute value of the range cannot be obtained. However, it is possible to estimate the range derivative from the consecutive subimages in a manner similar to (6.8) in the following way

$$\dot{\varphi}_t^m = \frac{1}{TM^2} \sum_{i=1}^{M} \sum_{j=1}^{M} \arg \left\{ \tilde{I}_{ij}(t) \tilde{I}^*_{ij}(t-T) \right\} \tag{6.9}$$

where $\tilde{I}_{ij}(t)$ is the complex $M \times M$ subimage generated from radar echo t, see Section 2.2 and Figure 2.3, and T is the time between radar pulses. This is basically an estimate of the average range to the centre of the imaged scene. The subimage is created with an assumption of straight and constant velocity trajectory with nominal state values. Note that it is only raw data used for the image generation that is summed here, not the whole range dimension as in (6.8). This is important, if the image to be created is not the same size as the raw data. Range gradient estimated with (6.9) is illustrated in Figure 6.1 (plotted with dotted line) together with analytically calculated range gradients based on (6.4) (plotted with solid and dashed lines). The one plotted with solid line is based on the correct trajectory, *i.e.* data are collected with the same trajectory used for the analytical expression. For the range gradient plotted with dashed line another trajectory, different from the one used for collecting data, is used. As it can be seen from this plot the estimate of the range gradient (6.9) can be interpreted as a measurement y_t and (6.4) can be interpreted as $h(x_t)$ giving the standard measurement equation. With this relation a standard EKF is applied and the performance is evaluated.

6.3 EKF and Evaluation of the Performance

Given the dynamical and the measurement models of the system as in (3.2a) and (3.2b), the EKF is defined by the following recursive steps, [Kailath et al., 2000, Gustafsson, 2010],

$$\hat{x}_{t+1|t} = f(\hat{x}_{t|t}, 0) \tag{6.10a}$$
$$P_{t+1|t} = F_t P_{t|t} F_t^T + B_t Q_t B_t^T \tag{6.10b}$$
$$F_t = \frac{\partial}{\partial x} f(x, w)\Big|_{x=\hat{x}_{t|t},\ w=0} \tag{6.10c}$$
$$B_t = \frac{\partial}{\partial w} f(x, w)\Big|_{x=\hat{x}_{t|t},\ w=0} \tag{6.10d}$$
$$\hat{x}_{t|t} = \hat{x}_{t|t-1} + K_t(y_t - h(\hat{x}_{t|t-1})) \tag{6.10e}$$
$$P_{t|t} = P_{t|t-1} - K_t H_t P_{t|t-1} \tag{6.10f}$$
$$H_t = \frac{\partial}{\partial x} h(x)\Big|_{x=\hat{x}_{t|t-1}} \tag{6.10g}$$
$$K_t = P_{t|t-1} H_t^T (H_t P_{t|t-1} H_t^T + R_t)^{-1} \tag{6.10h}$$

Here $\hat{x}_{t|t}$ is the estimate of the states in the time t given all the measurements up to the time t and $\hat{x}_{t|t-1}$ is the estimate of the states at time t given all the measurements up to the time $t-1$. $P_{t|t}$ and $P_{t|t-1}$ are their respective covariances. The rest of the notation follows from Section 3.1.

The dynamical model of the system used in this case is the same as in the Section 3.3, *i.e.* (3.24a). The measurements that are used are the range gradient $\dot{R}_t^m$ obtained from (6.9) and scaled with factor $-4\pi/\lambda$, and the accelerations. The

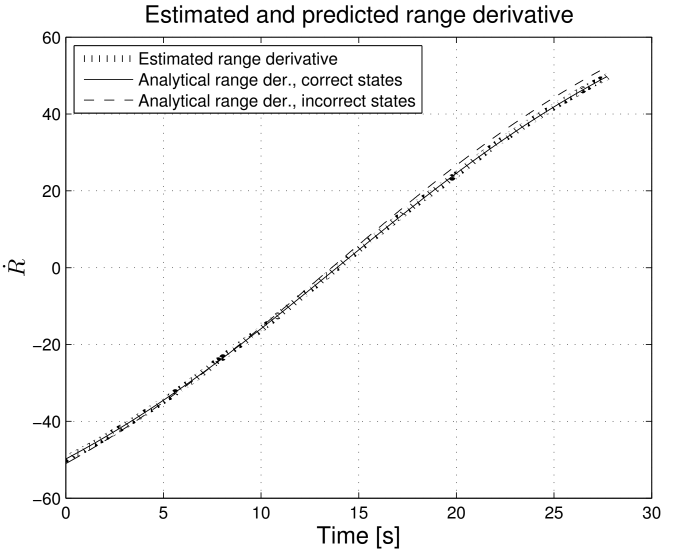

(a) Range derivative, the whole trajectory.

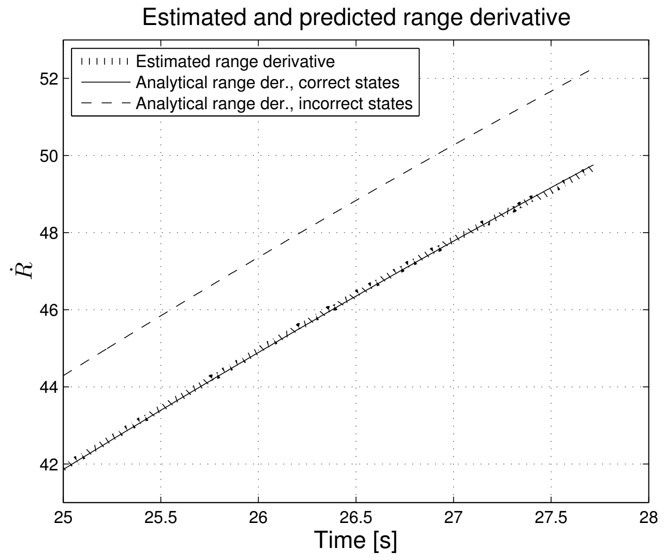

(b) Range derivative, only the last few seconds of the trajectory.

Figure 6.1: *Range derivative estimated from data (dotted line) and calculated by the analytical expression (solid and dashed lines). Solid line curve is generated with correct trajectory, while dashed is not.*

measurement equation is then

$$\underbrace{\begin{bmatrix} \tilde{a}_t^X \\ \tilde{a}_t^Y \\ \dot{R}_t^m \end{bmatrix}}_{y_t} = \underbrace{\begin{bmatrix} a_t^X \\ a_t^Y \\ \frac{-(X_m-X_t)v_t^X+Y_t v_t^Y-R_N \sin(\Psi)v_t^Y+\frac{Y_t \sin(\Psi)(X_m-X_t)v_t^X}{R_N}}{\sqrt{R_N^2+Y_t^2-2R_N Y_t \sin(\Psi)}} \end{bmatrix}}_{h(x_t)} + \underbrace{\begin{bmatrix} e_t^{a^X} \\ e_t^{a^Y} \\ e_t^{\dot{R}} \end{bmatrix}}_{e_t}, \tag{6.11}$$

where $\tilde{a}_t$ is the measured acceleration, and e_t is white Gaussian noise with covariance matrix $W = \text{diag}\{W_a,\ W_a,\ W_{\dot{R}}\}$ (here covariance matrix of the measurement noise is called W instead of R to avoid collision with range which is called R). In order to use EKF, the Jacobian of the measurement equation with respect to the states, $\partial h/\partial x$ is needed. For the measurement equation above, the Jacobian is (omitting time index for readability)

$$\frac{\partial h}{\partial x} = \begin{bmatrix} \frac{\partial h_1}{\partial X} & \frac{\partial h_1}{\partial Y} & \frac{\partial h_1}{\partial v^X} & \frac{\partial h_1}{\partial v^Y} & \frac{\partial h_1}{\partial a^X} & \frac{\partial h_1}{\partial a^Y} \\ \frac{\partial h_2}{\partial X} & \frac{\partial h_2}{\partial Y} & \frac{\partial h_2}{\partial v^X} & \frac{\partial h_2}{\partial v^Y} & \frac{\partial h_2}{\partial a^X} & \frac{\partial h_2}{\partial a^Y} \\ \frac{\partial h_3}{\partial X} & \frac{\partial h_3}{\partial Y} & \frac{\partial h_3}{\partial v^X} & \frac{\partial h_3}{\partial v^Y} & \frac{\partial h_3}{\partial a^X} & \frac{\partial h_3}{\partial a^Y} \end{bmatrix} \tag{6.12}$$

and the nonzero elements are (with $\sin(\Psi) = s_\Psi$)

$$\frac{\partial h_1}{\partial a^X} = 1 \tag{6.13a}$$

$$\frac{\partial h_2}{\partial a^Y} = 1 \tag{6.13b}$$

$$\frac{\partial h_3}{\partial X} = \frac{v^X + \frac{(X_m-X)v^Y s_\Psi}{R_N} - \frac{Y v^X s_\Psi}{R_N} + \frac{(X_m-X)^2 Y v^X s_\Psi}{R_N^3}}{R} - \frac{\left((X_m - X)v^X - Y v^Y + v^Y R_N s_\Psi - \frac{(X_m-X)v^X Y s_\Psi}{R_N}\right)(X_m - X)\left(1 - \frac{Y s_\Psi}{R_N}\right)}{R^3} \tag{6.13c}$$

$$\frac{\partial h_3}{\partial Y} = \frac{v^Y + \frac{(X_m-X)v^X s_\Psi}{R_N}}{R} + \frac{\left((X_m - X)v^X - Y v^Y + v^Y R_N s_\Psi - \frac{(X_m-X)Y v^X s_\Psi}{R_N}\right)(Y - R_N s_\Psi)}{R^3} \tag{6.13d}$$

$$\frac{\partial h_3}{\partial v^X} = -\frac{X_m - X - \frac{(X_m-X)Y s_\Psi}{R_N}}{R} \tag{6.13e}$$

$$\frac{\partial h_3}{\partial v^Y} = \frac{Y - R_N s_\Psi}{R} \tag{6.13f}$$

Using this setup an EKF has been applied to two cases, one where range gradient measurement has not been used and one where it has. In order to simulate somewhat more realistic acceleration measurements, a bias of 0.005 m/s^2 is added to the X-direction and -0.005 m/s^2 to the Y-direction in addition to the noise. The performance is then compared in terms of RMSE of the trajectory and difference between correct and EKF focused SAR images.

The RMSE for the position and velocity based on the 30 Monte Carlo simulations as a function of time for cases with and without range gradient measurement is depicted in Figure 6.2a and Figure 6.2b for the structured scene and in Figure 6.3a and Figure 6.3b for the unstructured scene. The mean value of the power of the error image is 384.1 and 3596, respectively. These values can be compared to the values in Table 5.1 and Table 5.2. The resulting images created with one of the 30 EKF estimated trajectories are depicted in Figure 6.4. It can be seen in these images that addition of the range gradient measurement improves the image focus and the estimate of the navigation states, especially compared to the pure inertial estimates.

6.4 Comparison between Filter and Optimisation Method's Results

It is interesting to compare the results from the two suggested methods, optimisation and filter based. Since both methods have their advantages and disadvantages, it is the application and its need that decides which method to use and when. If shear performance is compared, the optimisation method performs better than the filter method. This is not surprising since the optimisation method is smoothing and smoothing always has better performance than filtering. This is illustrated in Figure 6.5 and Figure 6.6 where the RMSE values of the $X-$ and $Y-$position are compared for the two methods and the structured and the unstructured scene respectively. It is also seen that both methods perform slightly better for the structured scene, which is also expected. The focus measures which are used perform better on the structured scenes according to Chapter 4 and so does the range (or phase) gradient method [Wahl et al., 1994, Yegulalp, 1999].

On the other hand, the filter method is sequential and works on the subimages from each radar echo, giving the possibility of a real time implementation. The optimisation method is batch oriented and as such it is more suitable for off line applications or slow updates of the navigation parameters (complete SAR image must be created in order to estimate the navigation parameters). An efficient implementation of the optimisation algorithms is needed for the slow updates and this might require some heuristics.

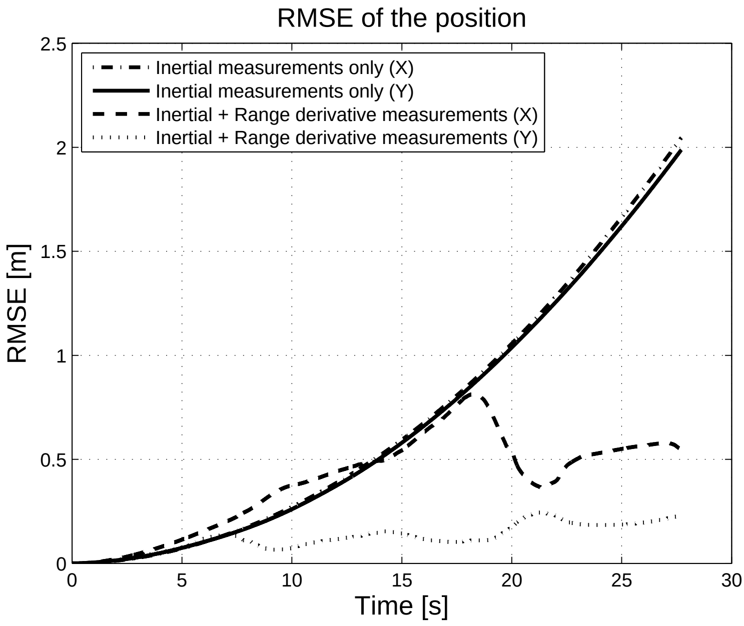

(a) RMSE for the EKF estimated position for the structured scene.

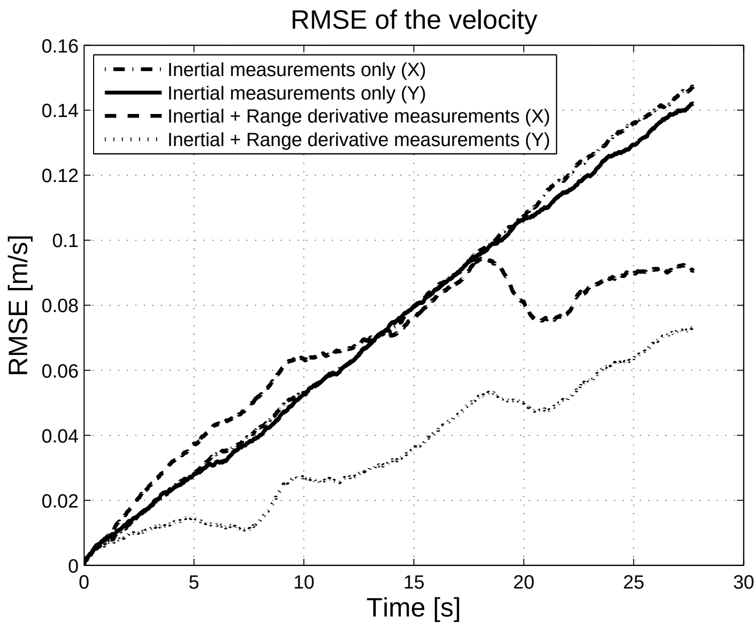

(b) RMSE for the estimated velocity for the structured scene.

Figure 6.2: *RMSE for the estimated position and velocity for the structured scene. X is the azimuth (or along track) dimension and Y is the range (or cross track) dimension.*

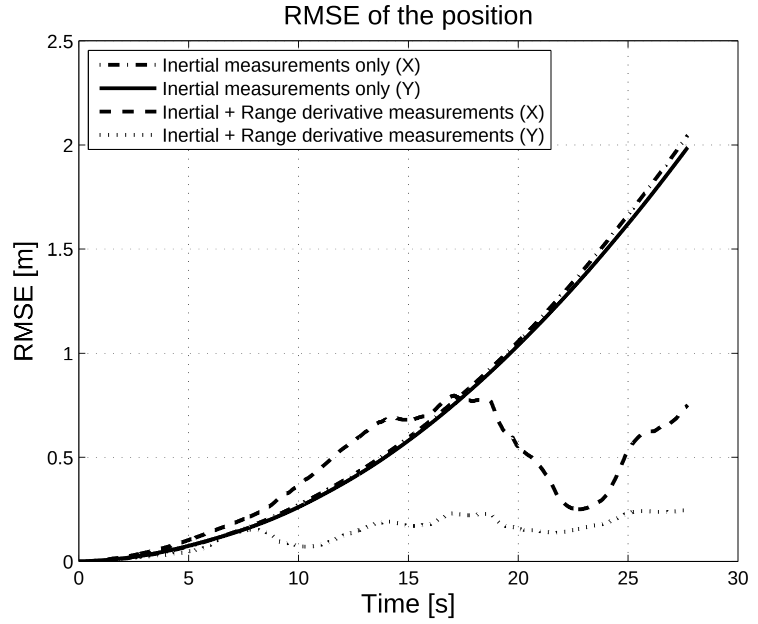

(a) *RMSE for the EKF estimated position for the unstructured scene.*

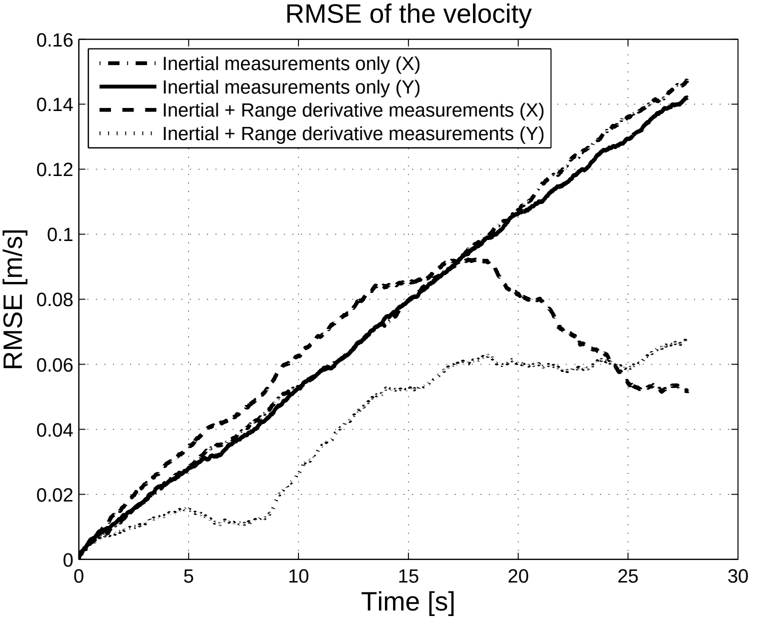

(b) *RMSE for the estimated velocity for the unstructured scene.*

Figure 6.3: *RMSE for the estimated position and velocity for the unstructured scene. X is the azimuth (or along track) dimension and Y is the range (or cross track) dimension.*

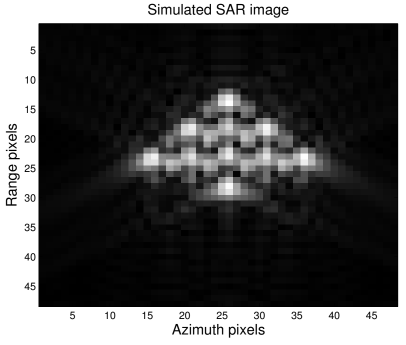

*(**a**) Image of the structured scene created with trajectory from the pure inertial estimate.*

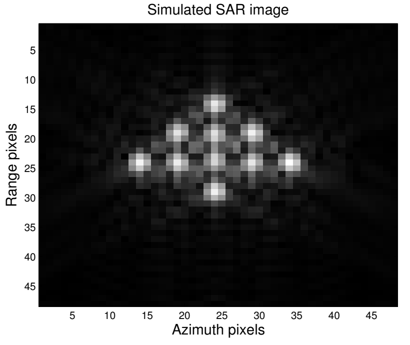

*(**b**) Image of the structured scene created with trajectory from the estimate with range gradient as measurement.*

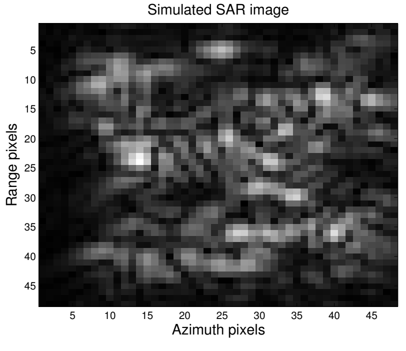

*(**c**) Image of the unstructured scene created with trajectory from the pure inertial estimate.*

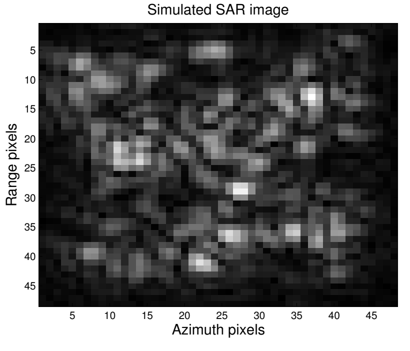

*(**d**) Image of the unstructured scene created with trajectory from the estimate with range gradient as measurement.*

Figure 6.4: *Images of the structured and unstructured scene created with estimated trajectories with and without range gradient measurement.*

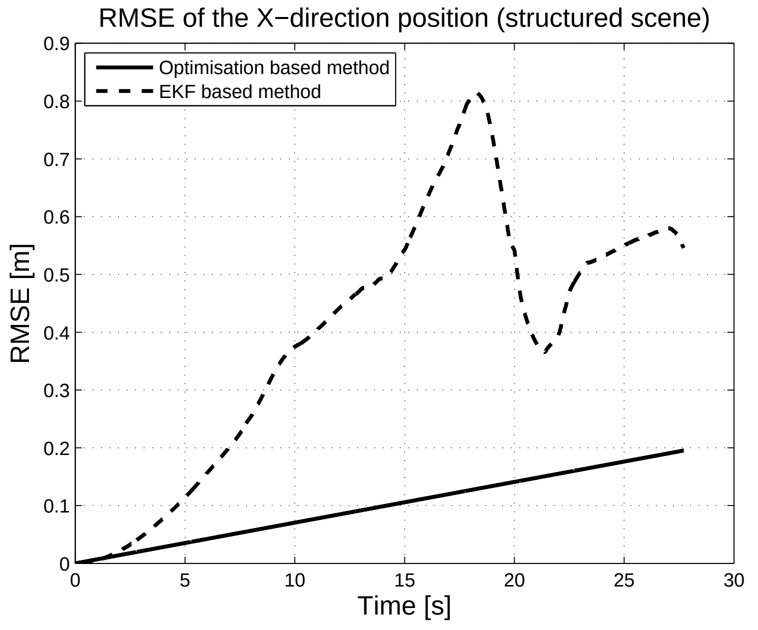

***(a)** RMSE of the X−direction position from optimisation and filter based methods for the structured scene.*

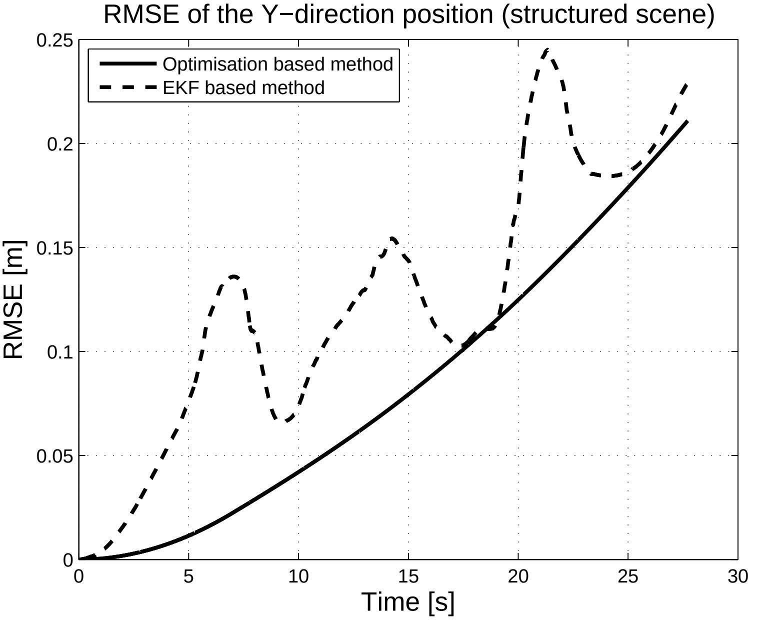

***(b)** RMSE of the Y−direction position from optimisation and filter based methods for the structured scene.*

***Figure 6.5:** RMSE for the estimated position from the optimisation and filter based methods, structured scene.*

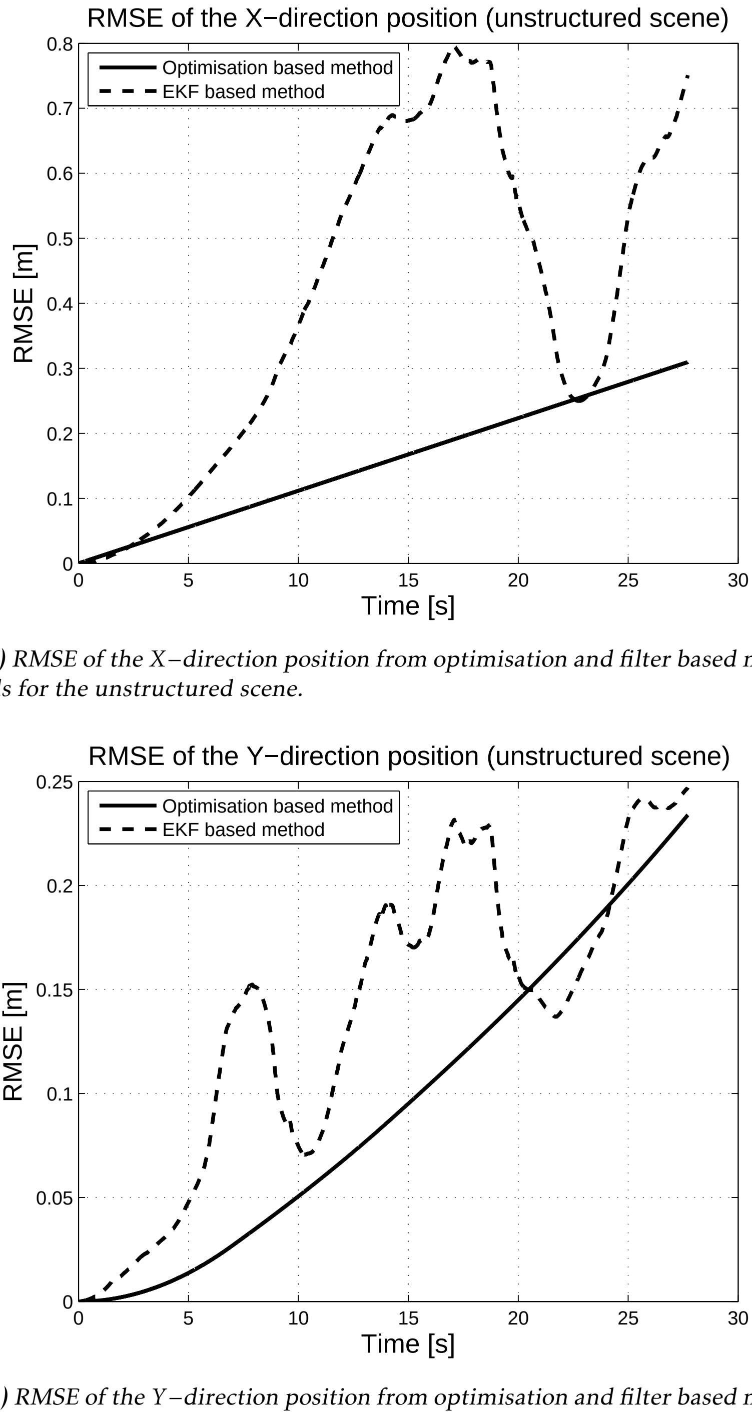

***(a)** RMSE of the X−direction position from optimisation and filter based methods for the unstructured scene.*

***(b)** RMSE of the Y−direction position from optimisation and filter based methods for the unstructured scene.*

***Figure 6.6:** RMSE for the estimated position from the optimisation and filter based methods, unstructured scene.*

7 Concluding Remarks

7.1 Conclusions

In this work a problem of simultaneous auto-focusing of SAR images and obtaining a good estimate of the navigation states by using the sensor fusion framework is presented. The solution is given for both complete SAR images and raw radar data leading to batch and filtering methods, respectively. The first one is more suitable for off-line applications, although it is not limited to these, while the second one can be applied to an on-line case. The methods have been evaluated on simulated test images, that should be representative for the imaged scenes.

The results from both batch and filter based methods show a good potential of obtaining good auto-focused images and fairly good navigation states estimate, without high precision navigation aids, like GNSS. The two-stage batch method based on two different focus measures works good. In the first stage the smooth and convex measure, but with no pronounced minimum for the correct parameters (like the entropy 2 focus measure) is used, and some other measure (like entropy 1 or TG) with sharper minimum for correct parameter values is used in the second stage. The benefit of the second stage, at least in the evaluated cases, is not high and the second stage could be skipped if the accuracy is sufficient after the first stage.

If the results from both methods are compared to the accuracy obtained without SAR images used as a sensor, but with all navigation states measured, the performance is better in the batch case, which is expected. For that case, the performance is fully comparable with the case where all states are measured. For the filter case, the performance is somewhat worse, especially for the unstructured scene, but still better than the accuracy of the measurements from Table 3.1. However, due to the nature of the SAR images, there are ambiguities that still lead to the limitations in quality of the navigation states estimate.

7.2 Future Work

Since only simulated images are used in this thesis, the next logical step is to use real data from the CARABAS radar and apply the described methods to these. In that case a complete 3-DOF or even 6-DOF dynamical model is needed. However, the methods that are suggested here are general and flexible and extension of the dynamics is not a problem.

Another thing that could be further investigated is the focus measures used for SAR images. Here, focus measures traditionally used in optical image processing are tested. Although they seem to work satisfactory for SAR images, they are tailored for optical images that have quite different nature. Therefore it would be interesting to try to find a focus measure for the SAR images where SAR images creation process and their nature are taken into account. The aim is to find some more robust, possibly convex measure.

The raw data method applied here is related to the phase gradient (PG) method used extensively for SAR auto-focusing. The method seems to work well, but it would be interesting to apply some other parametric methods in the raw data domain. For example, as demonstrated in Chapter 2, a point target will be imaged as a hyperbola in a RAR image. If a scene contains such point targets it should be possible to search for the hyperbolas in the raw data and estimate the platform's motion from these. This method would be coupled to the SLAM method even tighter where usual features in the images are replaced with hyperbolas in the raw radar data and the ideas and approach from Sjanic et al. [2011] could then be applied.

Another idea related to SLAM and parametric methods that can be further examined, is the concept of "Cooperative SAR". Here, N platforms with radars are flying around and collecting radar echoes from the scene. The scene is modelled as a set of D dominant point scatterers at positions s_d, and at each time instant each platform registers ranges to the L strongest echos. The following measurement model is then obtained

$$y_t^i = \|p_t^i - s_{d_l}\| + e_t^i \tag{7.1}$$

$$\begin{aligned}
y_t^i &: \text{ platform } i\text{'s detections from the radar echos at time } t,\ \mathbf{dim}(y_t^i) \leq L,\\
p_t^i &: \text{ position of the platform } i \text{ at time } t,\\
s_{d_l} &: \text{ position of the scatterer } d,\ d_l \text{ is association of echo } l \text{ to scatterer } d,\\
e_t^i &: \text{ measurement noise for platform } i \text{ at time } t,\\
i &= 1, \ldots, N,\\
d &= 1, \ldots, D,\\
l &= 1, \ldots, L.
\end{aligned}$$

This approach differs from the basic SAR approach, which is nonparametric and similar to the TkBD, since some kind of association between measurements and scatterers is needed and strong assumption about the scatterers in the scene is made.

Bibliography

L. E. Andersson. On the Determination of a Function from Spherical Averages. *SIAM Journal on Mathematical Analysis*, 19(1):214–232, 1988. doi: 10.1137/0519016. URL `http://link.aip.org/link/?SJM/19/214/1`. Cited on page 9.

T. Bailey and H. Durrant-Whyte. Simultaneous localization and mapping (SLAM): Part II. *IEEE Robotics & Automation Magazine*, 13(3):108–117, Septemeber 2006. Cited on page 5.

T. Bayes. An Essay towards solving a Problem in the Doctrine of Chances. *The Philosophical Transactions of the Royal Society of London*, 53:370–418, 1763. Cited on page 16.

C. Cafforio, C. Prati, and F. Rocca. SAR data focusing using seismic migration techniques. *IEEE Transactions on Aerospace and Electronic Systems*, 27(2): 194 –207, March 1991. ISSN 0018-9251. doi: 10.1109/7.78293. Cited on page 9.

L. J. Cutrona, W. E. Vivian, E. N. Leith, and G. O. Hall. A high-resolution radar combat-surveillance system. *IRE Transactions on Military Electronics*, MIL-5(2):127–131, April 1961. ISSN 0096-2511. doi: 10.1109/IRET-MIL.1961.5008330. Cited on page 9.

H. Durrant-Whyte and T. Bailey. Simultaneous Localization and Mapping: Part I. *IEEE Robotics & Automation Magazine*, 13(12):99–110, June 2006. Cited on page 5.

J. Farrell and M. Barth. *The global positioning system and inertial navigation*. McGraw-Hill Professional, 1999. Cited on page 20.

J. A. Fawcett. Inversion of N-Dimensional Spherical Averages. *SIAM Journal on Applied Mathematics*, 45(2):336–341, 1985. ISSN 00361399. URL `http://www.jstor.org/stable/2101820`. Cited on page 9.

R. Ferzli and L. J. Karam. No-reference objective wavelet based noise immune image sharpness metric. In *Proceedings of International Conference on Image*

Processing, ICIP 2005, volume 1, pages I–405–8, Septemeber 2005. Cited on page 29.

J. R. Fienup. Phase Error Correction by Shear Averaging. In *Signal Recovery and Synthesis*, pages 134–137. Optical Society of America, June 1989. Cited on pages 61 and 63.

N. J. Gordon, D. J. Salmond, and A. F. M. Smith. Novel approach to nonlinear/non-Gaussian Bayesian state estimation. *IEE Proceedings of Radar and Signal Processing*, 140(2):107 –113, April 1993. ISSN 0956-375X. Cited on page 18.

F. Gustafsson. *Statistical Sensor Fusion*. Studentliteratur, Lund, 2010. Cited on pages 17, 24, and 64.

H. Hellsten and L. E. Andersson. An inverse method for the processing of synthetic aperture radar data. *Inverse Problems*, 3(1):111, 1987. URL `http://stacks.iop.org/0266-5611/3/i=1/a=013`. Cited on page 9.

W. Huang and Z. Jing. Evaluation of focus measures in multi-focus image fusion. *Pattern Recognition Letters*, 28(4):493 – 500, 2007. ISSN 0167-8655. doi: DOI:10.1016/j.patrec.2006.09.005. URL `http://www.sciencedirect.com/science/article/B6V15-4MC719D-1/2/00a5dc2f7f03dd28727131ac88ff59f2`. Cited on page 27.

T. Kailath, A. H. Sayed, and B. Hassibi. *Linear Estimation*. Prentice-Hall, Upper Saddle River, New Jersey, 2000. Cited on pages 18 and 64.

R. E. Kalman. A New Approach to Linear Filtering and Prediction Problems. *Transactions of the ASME–Journal of Basic Engineering*, 82(Series D):35–45, 1960. Cited on page 17.

M. Kristan, J. Pers, Perse M., and S. Kovacic. A Bayes-spectral-entropy-based measure of camera focus using a discrete cosine transform. *Pattern Recognition Letters*, 27(13):1431 – 1439, 2006. ISSN 0167-8655. doi: DOI:10.1016/j.patrec.2006.01.016. Cited on page 28.

J. B. Kuipers. *Quaternions and Rotation Sequences*. Princeton University Press, 1999. Cited on page 21.

R. Larsson, Z. Sjanic, M. Enqvist, and L. Ljung. Direct Prediction-error Identification of Unstable Nonlinear Systems Applied to Flight Test Data. In *Proceedings of the 15th IFAC Symposium on System Identification*, Saint-Malo, France, July 2009. Not cited.

A. S. Milman. SAR Imaging by Omega-K Migration. *International Journal of Remote Sensing*, 14(10):1965–1979, 1993. Cited on page 9.

R. L. Jr. Morrison and D. C. Jr. Munson. An experimental study of a new entropy-based SAR autofocus technique. In *Proceedings of International Conference on Image Processing, ICIP 2002*, volume 2, pages II–441–4, September 2002. doi: 10.1109/ICIP.2002.1039982. Cited on pages 12 and 29.

F. Natterer. *The Mathematics of Computerised Tomography*. New York: Wiley, 1986. Cited on pages 5 and 9.

J. Nocedal and S. J. Wright. *Numerical Optimization*. Springer, New York, 2006. Cited on page 48.

C. Oliver and S. Quegan. *Understanding Synthetic Aperture Radar Images*. The SciTech Radar and Defense Series. SciTech, 2004. ISBN ISBN 1-891121-31-6. Cited on pages 12 and 61.

F. Rocca. Synthetic Aperture Radar: a New Application for Wave Equation Techniques. *Stanford Exploration Project SEP-56*, pages 167–189, 1987. URL `http://sepwww.stanford.edu/oldreports/sep56/56_13.pdf`. Cited on page 9.

D. J. Salmond and H. Birch. A paricle filter for track-before-detect. In *Proceedings of the American Control Conference*, pages 3755–3760, Arlington, VA, USA, June 2001. Cited on page 3.

M. D. Shuster. A survey of attitude representations. *The Journal of Astronautical Sciences*, 41(4):439–517, October 1993. Cited on page 21.

Z. Sjanic and F. Gustafsson. Simultaneous Navigation and SAR Auto-focusing. In *Proceedings of 13th International Conference on Information Fusion*, Edinburgh, UK, July 2010. Cited on page 47.

Z. Sjanic, M. A. Skoglund, T. B. Schön, and F. Gustafsson. A Nonlinear Least-Squares Approach to the SLAM Problem. In *Proceedings of 18th IFAC World Congress (submitted to)*, Milano, Italy, August/Septemeber 2011. Cited on page 74.

L. M. H. Ulander, H. Hellsten, and G. Stenstrom. Synthetic-aperture radar processing using fast factorized back-projection. *Aerospace and Electronic Systems, IEEE Transactions on*, 39(3):760–776, July 2003. ISSN 0018-9251. doi: 10.1109/TAES.2003.1238734. Cited on page 11.

D. E. Wahl, P. H. Eichel, D. C. Ghiglia, and C. V. Jr. Jakowatz. Phase gradient autofocus - a robust tool for high resolution SAR phase correction. *IEEE Transactions on Aerospace and Electronic Systems*, 30(3):827–835, July 1994. ISSN 0018-9251. doi: 10.1109/7.303752. Cited on pages 12, 61, and 67.

L. Xi, L. Guosui, and J. Ni. Autofocusing of ISAR images based on entropy minimization. *IEEE Transactions on Aerospace and Electronic Systems*, 35(4):1240–1252, October 1999. ISSN 0018-9251. doi: 10.1109/7.805442. Cited on pages 12 and 29.

M. Xing, R. Jiang, X.and Wu, F. Zhou, and Z. Bao. Motion Compensation for UAV SAR Based on Raw Radar Data. *IEEE Transactions on Geoscience and Remote Sensing*, 47(8):2870–2883, August 2009. ISSN 0196-2892. doi: 10.1109/TGRS.2009.2015657. Cited on pages 12, 50, and 61.

A. F. Yegulalp. Minimum entropy SAR autofocus. In *7th Adaptive Sensor Array Processing Workshop*, March 1999. Cited on pages 29, 61, and 67.

Licentiate Theses
Division of Automatic Control
Linköping University

P. Andersson: Adaptive Forgetting through Multiple Models and Adaptive Control of Car Dynamics. Thesis No. 15, 1983.

B. Wahlberg: On Model Simplification in System Identification. Thesis No. 47, 1985.

A. Isaksson: Identification of Time Varying Systems and Applications of System Identification to Signal Processing. Thesis No. 75, 1986.

G. Malmberg: A Study of Adaptive Control Missiles. Thesis No. 76, 1986.

S. Gunnarsson: On the Mean Square Error of Transfer Function Estimates with Applications to Control. Thesis No. 90, 1986.

M. Viberg: On the Adaptive Array Problem. Thesis No. 117, 1987.

K. Ståhl: On the Frequency Domain Analysis of Nonlinear Systems. Thesis No. 137, 1988.

A. Skeppstedt: Construction of Composite Models from Large Data-Sets. Thesis No. 149, 1988.

P. A. J. Nagy: MaMiS: A Programming Environment for Numeric/Symbolic Data Processing. Thesis No. 153, 1988.

K. Forsman: Applications of Constructive Algebra to Control Problems. Thesis No. 231, 1990.

I. Klein: Planning for a Class of Sequential Control Problems. Thesis No. 234, 1990.

F. Gustafsson: Optimal Segmentation of Linear Regression Parameters. Thesis No. 246, 1990.

H. Hjalmarsson: On Estimation of Model Quality in System Identification. Thesis No. 251, 1990.

S. Andersson: Sensor Array Processing; Application to Mobile Communication Systems and Dimension Reduction. Thesis No. 255, 1990.

K. Wang Chen: Observability and Invertibility of Nonlinear Systems: A Differential Algebraic Approach. Thesis No. 282, 1991.

J. Sjöberg: Regularization Issues in Neural Network Models of Dynamical Systems. Thesis No. 366, 1993.

P. Pucar: Segmentation of Laser Range Radar Images Using Hidden Markov Field Models. Thesis No. 403, 1993.

H. Fortell: Volterra and Algebraic Approaches to the Zero Dynamics. Thesis No. 438, 1994.

T. McKelvey: On State-Space Models in System Identification. Thesis No. 447, 1994.

T. Andersson: Concepts and Algorithms for Non-Linear System Identifiability. Thesis No. 448, 1994.

P. Lindskog: Algorithms and Tools for System Identification Using Prior Knowledge. Thesis No. 456, 1994.

J. Plantin: Algebraic Methods for Verification and Control of Discrete Event Dynamic Systems. Thesis No. 501, 1995.

J. Gunnarsson: On Modeling of Discrete Event Dynamic Systems, Using Symbolic Algebraic Methods. Thesis No. 502, 1995.

A. Ericsson: Fast Power Control to Counteract Rayleigh Fading in Cellular Radio Systems. Thesis No. 527, 1995.

M. Jirstrand: Algebraic Methods for Modeling and Design in Control. Thesis No. 540, 1996.

K. Edström: Simulation of Mode Switching Systems Using Switched Bond Graphs. Thesis No. 586, 1996.

J. Palmqvist: On Integrity Monitoring of Integrated Navigation Systems. Thesis No. 600, 1997.

A. Stenman: Just-in-Time Models with Applications to Dynamical Systems. Thesis No. 601, 1997.

M. Andersson: Experimental Design and Updating of Finite Element Models. Thesis No. 611, 1997.

U. Forssell: Properties and Usage of Closed-Loop Identification Methods. Thesis No. 641, 1997.

M. Larsson: On Modeling and Diagnosis of Discrete Event Dynamic systems. Thesis No. 648, 1997.

N. Bergman: Bayesian Inference in Terrain Navigation. Thesis No. 649, 1997.

V. Einarsson: On Verification of Switched Systems Using Abstractions. Thesis No. 705, 1998.

J. Blom, F. Gunnarsson: Power Control in Cellular Radio Systems. Thesis No. 706, 1998.

P. Spångéus: Hybrid Control using LP and LMI methods – Some Applications. Thesis No. 724, 1998.

M. Norrlöf: On Analysis and Implementation of Iterative Learning Control. Thesis No. 727, 1998.

A. Hagenblad: Aspects of the Identification of Wiener Models. Thesis No. 793, 1999.

F. Tjärnström: Quality Estimation of Approximate Models. Thesis No. 810, 2000.

C. Carlsson: Vehicle Size and Orientation Estimation Using Geometric Fitting. Thesis No. 840, 2000.

J. Löfberg: Linear Model Predictive Control: Stability and Robustness. Thesis No. 866, 2001.

O. Härkegård: Flight Control Design Using Backstepping. Thesis No. 875, 2001.

J. Elbornsson: Equalization of Distortion in A/D Converters. Thesis No. 883, 2001.

J. Roll: Robust Verification and Identification of Piecewise Affine Systems. Thesis No. 899, 2001.

I. Lind: Regressor Selection in System Identification using ANOVA. Thesis No. 921, 2001.

R. Karlsson: Simulation Based Methods for Target Tracking. Thesis No. 930, 2002.

P.-J. Nordlund: Sequential Monte Carlo Filters and Integrated Navigation. Thesis No. 945, 2002.

M. Östring: Identification, Diagnosis, and Control of a Flexible Robot Arm. Thesis No. 948, 2002.

C. Olsson: Active Engine Vibration Isolation using Feedback Control. Thesis No. 968, 2002.

J. Jansson: Tracking and Decision Making for Automotive Collision Avoidance. Thesis No. 965, 2002.

N. Persson: Event Based Sampling with Application to Spectral Estimation. Thesis No. 981, 2002.

D. Lindgren: Subspace Selection Techniques for Classification Problems. Thesis No. 995, 2002.

E. Geijer Lundin: Uplink Load in CDMA Cellular Systems. Thesis No. 1045, 2003.

M. Enqvist: Some Results on Linear Models of Nonlinear Systems. Thesis No. 1046, 2003.

T. Schön: On Computational Methods for Nonlinear Estimation. Thesis No. 1047, 2003.

F. Gunnarsson: On Modeling and Control of Network Queue Dynamics. Thesis No. 1048, 2003.

S. Björklund: A Survey and Comparison of Time-Delay Estimation Methods in Linear Systems. Thesis No. 1061, 2003.

M. Gerdin: Parameter Estimation in Linear Descriptor Systems. Thesis No. 1085, 2004.

A. Eidehall: An Automotive Lane Guidance System. Thesis No. 1122, 2004.

E. Wernholt: On Multivariable and Nonlinear Identification of Industrial Robots. Thesis No. 1131, 2004.

J. Gillberg: Methods for Frequency Domain Estimation of Continuous-Time Models. Thesis No. 1133, 2004.

G. Hendeby: Fundamental Estimation and Detection Limits in Linear Non-Gaussian Systems. Thesis No. 1199, 2005.

D. Axehill: Applications of Integer Quadratic Programming in Control and Communication. Thesis No. 1218, 2005.

J. Sjöberg: Some Results On Optimal Control for Nonlinear Descriptor Systems. Thesis No. 1227, 2006.

D. Törnqvist: Statistical Fault Detection with Applications to IMU Disturbances. Thesis No. 1258, 2006.

H. Tidefelt: Structural algorithms and perturbations in differential-algebraic equations. Thesis No. 1318, 2007.

S. Moberg: On Modeling and Control of Flexible Manipulators. Thesis No. 1336, 2007.

J. Wallén: On Kinematic Modelling and Iterative Learning Control of Industrial Robots. Thesis No. 1343, 2008.

J. Harju Johansson: A Structure Utilizing Inexact Primal-Dual Interior-Point Method for Analysis of Linear Differential Inclusions. Thesis No. 1367, 2008.

J. D. Hol: Pose Estimation and Calibration Algorithms for Vision and Inertial Sensors. Thesis No. 1370, 2008.

H. Ohlsson: Regression on Manifolds with Implications for System Identification. Thesis No. 1382, 2008.

D. Ankelhed: On low order controller synthesis using rational constraints. Thesis No. 1398, 2009.

P. Skoglar: Planning Methods for Aerial Exploration and Ground Target Tracking. Thesis No. 1420, 2009.

C. Lundquist: Automotive Sensor Fusion for Situation Awareness. Thesis No. 1422, 2009.

C. Lyzell: Initialization Methods for System Identification. Thesis No. 1426, 2009.

R. Falkeborn: Structure exploitation in semidefinite programming for control. Thesis No. 1430, 2010.

D. Petersson: Nonlinear Optimization Approaches to $\mathcal{H}_2$-Norm Based LPV Modelling and Control. Thesis No. 1453, 2010.